

Technische Universität München
Institut für Energietechnik

Lehrstuhl für Thermodynamik

An Experimental Study on Vertical Subcooled Flow Boiling Under the Influence of Turbulence and Secondary Flows

Gregor Kurt Bloch

Vollständiger Abdruck der von der Fakultät für Maschinenwesen der
Technischen Universität München zur Erlangung des akademischen
Grades eines

DOKTOR – INGENIEURS

genehmigten Dissertation.

Vorsitzender:

Univ.-Prof. Dr. mont. habil. Dr. rer. nat. h. c. Ewald Werner

Prüfer der Dissertation:

1. Univ.-Prof. Dr.-Ing. Thomas Sattelmayer
2. Univ.-Prof. Dr. Horst-Michael Prasser,
Eidgenössische Technische Hochschule Zürich, Schweiz

Die Dissertation wurde am 04.05.2016 bei der Technischen Universität München
eingereicht und durch die Fakultät für Maschinenwesen am 16.09.2016 angenommen.

As the boiling phenomenon is so involved and complicated, the analysis of boiling heat transfer is an almost impossible problem.

- Shiro Nukiyama

Vorwort

Die vorliegende Arbeit entstand am Lehrstuhl für Thermodynamik der Technischen Universität München während meiner Zeit als wissenschaftlicher Mitarbeiter. Die Arbeit wurde vom Bundesministerium für Bildung und Forschung (BMBF) als Teil des Verbundprojekts “Modellierung, Simulation und Experimente zu Siedevorgängen in Druckwasserreaktoren “im Rahmen des BMBF-Förderkonzeptes “Energie 2020+ “unter dem Förderkennzeichen 02NUK010E gefördert.

Mein herzlicher Dank gilt meinem Doktorvater, Herrn Prof. Dr.-Ing. Thomas Sattelmayer, für die Betreuung der Arbeit, das entgegengebrachte Vertrauen, die Unterstützung der wissenschaftlichen Tätigkeit und den mir gewährten Freiraum bei der Gestaltung der Arbeit.

Herrn Prof. Horst-Michael Prasser danke ich für die Übernahme des Ko-referates und Herrn Prof. Werner für die Übernahme des Vorsitzes der mündlichen Prüfung.

Des Weiteren gilt mein Dank den Kollegen im Verbundprojekt und in Garching am Lehrstuhl. Es war eine unvergessliche Zeit.

Ebenso gilt der Dank den zahlreichen Studenten die im Rahmen des Projekts tatkräftig zum Gelingen beigetragen haben. In den dreieinhalb Jahren Laufzeit waren über 30 Studenten aus aller Welt am Projekt beteiligt, so dass ein Aufzählen von Namen hier den Rahmen sprengen würde. So viel sei gesagt: ohne euch wäre es nicht gegangen.

Nicht zuletzt gilt mein Dank allen meinen Freunden und meiner Familie für ihre Unterstützung.

München, im April 2016

Gregor Bloch

Wesentliche Teile dieser Dissertation wurden vom Autor bereits standardmäßig vorab als Konferenz- und Zeitschriftenbeiträge veröffentlicht [5–17, 21]. Alle Vorveröffentlichungen sind entsprechend der gültigen Promotionsordnung ordnungsgemäß gemeldet. Sie sind deshalb nicht zwangsläufig im Detail einzeln referenziert. Vielmehr wurde bei der Referenzierung eigener Vorveröffentlichungen Wert auf Verständlichkeit und inhaltlichen Bezug gelegt.

Significant parts of this Ph.D. thesis were published by the author beforehand in conference proceedings and journal papers [5–17, 21]. All of these prior printed publications are registered according to the valid doctoral regulations. However, not all of them are quoted explicitly everywhere as they are part of this present work being official documents. Whether these personal prior printed publications were referenced depended on maintaining comprehensibility and providing all necessary context.

Kurzfassung

Eine experimentelle Studie zum unterkühlten Strömungssieden entlang der gesamten Siedekurve unter Verwendung unterschiedlicher Messtechniken wird vorgestellt. Die Messtechniken beinhalten Hochgeschwindigkeitsfotographie, Particle-Image Velocimetry, Digitale Holografische Interferometrie sowie optische Mikrosonden. Ergebnisse zum voll ausgebildeten Blasen-sieden, zum Filmsieden sowie zum Übergang im Bereich der kritischen Wärmestromdichte werden präsentiert. Durch Strömungseinbauten werden zusätzliche Turbulenzen und Sekundärströmungen eingebracht, die signifikanten Einfluss auf das Siedeverhalten zeigen. Die Ergebnisse erlauben eine detailliertere Beschreibung der Phänomene sowohl beim Blasen- als auch beim Filmsieden, beispielsweise der Dampfphasengeschwindigkeiten, der Temperaturverteilungen in der Flüssigphase, Dampfverteilung und erreichbare Wärmestromdichten. Abschließend werden die vorgestellten Ergebnisse mit vorhandenen mechanistischen Modellen zur kritischen Wärmestromdichte verglichen, hierbei werden verschiedene Schwächen der vorhandenen Modelle aufgezeigt. Hierauf aufbauend wird ein Konzept für ein neues phänomenologisches Modell präsentiert.

Abstract

An experimental study on subcooled flow boiling along the entire boiling curve using various measuring techniques is presented. The measuring techniques include high-speed photography, particle image velocimetry, digital holographic interferometry and optical microprobes. Results are presented on fully developed nucleate boiling, film boiling and on the critical heat flux transition process. Inserts creating turbulence and secondary flows are applied to change the characteristics of the flow, showing significant influence on the boiling process. The results shed new light on phenomena in nucleate as well as in film boiling, such as vapor velocities, heat dispersion in the liquid phase, vapor distribution and achievable heat fluxes. Finally, results on the critical heat flux transient are compared to available mechanistic models, highlighting some of the shortcomings of the current methods. Based on this, a conceptualization for a new phenomenological model is presented.

Contents

List of figures	xiv
List of tables	xiv
Nomenclature	xv
1 Introduction	1
2 Boiling phenomena	3
2.1 Modes of boiling	3
2.2 Boiling curve and critical heat flux	3
2.2.1 Types of critical heat flux	5
2.2.2 Parametric trends in the critical heat flux	5
2.3 Critical heat flux models	7
2.3.1 Empirical models and look-up tables	7
2.3.2 Mechanistic models	8
2.4 Description of post-CHF boiling - fully developed film boiling	18
2.5 Influence of turbulence and secondary flows on boiling processes	20
2.5.1 Turbulence intensity	21
2.5.2 Vorticity	21
3 Measuring techniques	22
3.1 Challenges and techniques in boiling experiments	22
3.2 Overview on available measuring techniques	23
3.2.1 Non-invasive techniques	23
3.2.2 Invasive techniques	25
3.2.3 Measuring of parameters in the solid parts	27
3.2.4 Summary on available measuring techniques	28
3.3 Holographic interferometry	28
3.3.1 Analogue holographic interferometry	28
3.3.2 Digital holographic interferometry	30
4 Experimental setup and methods	32

4.1	Boiling test rig	32
4.1.1	Boiling chamber	34
4.1.2	Fluid	35
4.2	Flow inserts	35
4.2.1	Orifice insert	36
4.2.2	Twisted tape insert	37
4.3	Measuring techniques: setup and methods	38
4.3.1	Thermocouples	38
4.3.2	High-speed photography	39
4.3.3	Optical probes	42
4.3.4	Particle image velocimetry (PIV)	48
4.3.5	Digital holographic interferometry, holographic inter- ferometric velocimetry	51
4.4	Experimental procedure for boiling experiments	57
5	Nucleate boiling	58
5.1	Observed regimes	58
5.2	Distribution and velocity of vapor phase	59
5.2.1	High-speed photography	59
5.2.2	Probe measurements	61
5.3	Vapor agglomerations	62
5.3.1	Size	62
5.3.2	Liquid entrainment	63
5.3.3	Frequencies	64
5.3.4	Velocities	65
5.3.5	Behavior in the wakes of vapor agglomerations	66
5.3.6	Dynamic behavior of vapor agglomerations	68
5.4	Influence of inserts	70
5.4.1	Heat fluxes	70
5.4.2	Influence on vapor distribution	73
5.4.3	Periodic behavior of vapor layer	78
5.4.4	Velocities of vapor agglomerations with inserts	80
5.4.5	Heat distribution from holographic interferometry	80
5.4.6	Summary on the influence of inserts	80
6	Fully developed film boiling	83
6.1	Gas distribution	83

6.2	Velocity distribution in the liquid phase from PIV and HIIV	85
6.3	Heat distribution from digital holographic interferometry . . .	86
6.4	Summary on film boiling results	88
7	CHF transition	90
7.1	Gas-holdup	90
7.2	Frequencies of vapor agglomerations	92
7.3	Transition from holographic interferometry	92
7.4	Vapor layer behavior during DNB from probe measurements	94
7.5	Summary on the CHF transition	95
8	Critical review of the results, formulation of a new modeling approach	97
8.1	Bubble crowding model	97
8.2	Sublayer dryout model	100
8.3	Interfacial lift-off model	102
8.4	Conceptualization of a refined phenomenological model . . .	104
8.4.1	Drift-flux gradient and lift-force in the vapor phase .	105
8.4.2	Refined phenomenological approach	106
9	Summary and conclusions	109
	Supervised theses	110
	References	114

List of figures

2.1	Characteristical boiling curve	4
2.2	DNB trigger mechanisms for different mechanistic models . .	9
2.3	Phase distribution at CHF for the sublayer dryout model . .	13
2.4	Interfacial lift-off model: Cycle of events leading to the DNB	16
2.5	Schematic of vapor behavior in film boiling regime	19
4.1	Schematic of the boiling test rig	32
4.2	CAD model showing the main test rig	33
4.3	Sectional view of the boiling chamber and the copper heater	34
4.4	CAD rendering of flow inserts	36
4.5	Vortices created by the twisted tape insert	37
4.6	Velocity fields for twisted tape insert at different heights . .	38
4.7	Setup for high-speed photography	39
4.8	Numerical processing steps for high-speed photographs . . .	40
4.9	Optical Probes: effects of polishing angle	43
4.10	Schematic drawing of the beam setup for the optical probes	44
4.11	Microscope image of 3 tips of the optical probes	45
4.12	CAD rendering of the optical probe setup	46
4.13	Mounting of the optical probes in the channel	46
4.14	Signal treatment for the optical probes	47
4.15	PIV setup	50
4.16	Schematic setup of the digital holographic interferometer. . .	52
4.17	CAD model of the digital holographic interferometer	53
4.18	Interrogation area and sample results for DHI	54
4.19	Different reconstruction techniques in DHI	55
4.20	Influence of time intervals in I2I DHI	56
5.1	Fully developed nucleate boiling in the highly coalesced regime	59
5.2	Distribution of the vapor phase over the channel cross section for different subcoolings	60
5.3	Velocity profiles of the vapor phase for different subcoolings	60
5.4	Optical probes: maximum void fractions at different posi- tions and subcoolings	61

5.5	Photographs of the vapor structure over a larger area and in detailed recording of the middle section	63
5.6	Probe measurement showing the structure of one agglomeration with entrained liquid	64
5.7	Distribution of agglomeration frequencies	65
5.8	Velocity field in the wake of a vapor agglomeration	67
5.9	Temperature distribution in the vicinity of vapor agglomerations from DHI	69
5.10	Development of vapor agglomeration over time	69
5.11	Overview of flow regimes at CHF(-) with and without flow inserts	71
5.12	Heat fluxes along the entire boiling curve for the empty channel and orifice insert	72
5.13	Influence of inserts on CHF at different fluid subcoolings	72
5.14	Detailed view of flow regimes at CHF(-) with and without flow inserts	74
5.15	Distribution of the void fraction for different inserts (HSP)	75
5.16	Size distribution of isolated bubbles for different inserts (HSP)	75
5.17	Development of void fraction over the whole boiling curve (OP)	76
5.18	Maximum void fractions for different inserts (OP)	77
5.19	Distribution of agglomeration frequencies with the orifice insert	79
5.20	Interf. phase maps of heat distrib. with and without inserts	80
6.1	Development of film boiling	84
6.2	Photographs of film boiling at different subcoolings	84
6.3	Distribution of the void fraction in fully developed film boiling (OP)	85
6.4	Histograms of vertical and horizontal velocities in film boiling derived from HIIV	86
6.5	Interference phase maps of steady state film boiling at different subcoolings	87
6.6	Interference phase maps showing film boiling with different flow inserts	88
7.1	Photographic images of transition from nucleate boiling into transition boiling for different subcoolings	91
7.2	Interference phase maps for CHF transition	93

7.3	Development of the heat flux, void fractions and bubble sizes/contact times over time for the CHF transient at 5 K subcooling	95
8.1	Vapor layer distribution at CHF(-) for the reference case and with added turbulence by orifice	98
8.2	Measurement of void fractions from optical probes	99
8.3	Development of the heat flux, void fractions and bubble sizes/contact times over time for the CHF transient at 9 K subcooling	101
8.4	Slip velocity calculated by Chisholms correlation.	105
8.5	Proposed new mechanisms for CHF transition	107

List of tables

4.1	Physical parameters of dodekafluoro-2-methylpentan-3-one .	35
4.2	Camera specifications	40
5.1	Dimensions of vapor agglomerations close to CHF at different subcoolings	63
5.2	Average frequencies of vapor agglomerations	65
5.3	Velocities for peaks and tails of agglomerations	66
5.4	CHF increase to reference for different subcoolings	73
5.5	CHF increase to reference for different flow velocities	73
5.6	Change in maximum local void fraction compared to reference for different probe positions	77
5.7	Dimensions of vapor agglomerations for different inserts	79

Nomenclature

Latin Characters

A_1	Empirical coefficient	-
A	Area	m^2
a	Empirical constant	-
A_L	Light wave amplitude	-
a_1	Empirical constant	-
a_2	Empirical constant	-
a_3	Empirical constant	-
A_w	Wetting front area	m^2
A_b	Bubble size	m^2
b	Body force	$m^2 s^{-2}$
b	Ratio of liquid length to vapor wavelength	-
c	Wave speed	$m s^{-1}$
c	Speed of sound	$m s^{-1}$
c_r	Real component of wave speed	$m s^{-1}$
c_D	Drag coefficient	-
c_p	Specific heat capacity at constant pressure	$J kg^{-1} K^{-1}$
c_v	Specific heat capacity at constant volume	$J kg^{-1} K^{-1}$
d	Tube diameter	m
D_e	Equivalent diameter	m
d_r	Distance to reconstruction plane	m
d_b	Bubble size	m
D_e	Equivalent diameter	m
D_p	Average bubble diameter	m
G	Axial mass flux	$kg m^{-2} s^{-1}$
g	Gravity	$m s^{-2}$
G'	Lateral mass flux due to turbulence	$kg m^{-2} s^{-1}$
g_n	Body force per unit mass normal to surface	$m s^{-2}$
g_e	Gravitational acceleration on earth	$m s^{-2}$
G	Mass flux	$kg m^{-2} s^{-1}$
G_m	Relative mass flux	$kg m^{-2} s^{-1}$

h_f	Saturated liquid enthalpy	J kg^{-1}
h_l	Liquid enthalpy	J kg^{-1}
h_{fg}	Enthalpy of evaporation	J kg^{-1}
h_{ld}	Enthalpy at point of bubble detachment	J kg^{-1}
H_g	Vapor layer thickness	m
H_l	Liquid layer thickness	m
h_{LG}	Latent heat of evaporation	J kg^{-1}
h_{SC}	Subcooled heat transfer coefficient	$\text{W m}^{-2} \text{K}^{-1}$
i	Imaginary unit	-
i_b	Turbulence intensity at the bubbly layer edge	-
j	Complex number $\exp(\dots j)$	-
k	Empirical constant	-
k_w	Wave number	-
a_L	Two phase multiplier	-
L	Tube length	metre
L_m	Vapor blanket length	m
\dot{m}	Mass flow	kg s^{-1}
\dot{m}''	Mass flux	$\text{kg m}^{-2} \text{s}^{-1}$
M	Empirical coefficient	-
$m_{\xi,\eta}$	Pixelposition	-
n	Empirical coefficient	-
n_b	Number of bubbles	-
N_η	Number of pixel in η -direction	-
N_ξ	Number of pixel in ξ -direction	-
p	Pressure	Pa
p	Pressure	Pa
\dot{q}_{CHF}	Critical heat flux	kW m^{-2}
\dot{q}	Heat flux	kW m^{-2}
t	Time	s
t_a	Threshold time value for agglomeration detection	s
t_c	Contact time at optical probe tip	s
T	Temperature	K
Tu	Turbulence intensity	-
T_L	Temperature of liquid entering sublayer	K
T_{sat}	Saturated liquid temperature	K
T_{sub}	Fluid subcooling	K
T_w	Wall temperature	K

U	Mean axial velocity	m s^{-1}
U	Analogue voltage signal	V
u	Horizontal velocity component	m s^{-1}
u'	Horizontal velocity fluctuations	m s^{-1}
U_b	Vapor blanket velocity	m s^{-1}
U_{bL}	Mean liquid velocity close to vapor plumes	m s^{-1}
\bar{U}_l	Mean velocity of the liquid phase	m s^{-1}
\bar{U}_g	Mean velocity of the vapor phase	m s^{-1}
u_L	Horizontal liquid velocity	m s^{-1}
U_m	Mean liquid velocity	m s^{-1}
U_t	Threshold voltage	V
v	Vertical velocity component	m s^{-1}
v'	Vertical velocity fluctuations	m s^{-1}
v_s	Superficial vertical velocity	m s^{-1}
v_{11}	Radial velocity created by vapor generation	m s^{-1}
v_L	Vertical liquid velocity	m s^{-1}
v_s	Liquid superficial velocity	m s^{-1}
v_v	Local vapor velocity	m s^{-1}
v_v	Vertical vapor velocity	m s^{-1}
x	Coordinate	m
x_1	Average qualities in the core region	-
x_2	Average qualities in the bubbly layer	-
x_w	Distance to channel wall	m
y	Coordinate, distance from grid position	m
y_0	Grid position	m
j	Complex number	-
z	Streamwise coordinate	m

Greek Characters

δ	Mean vapor layer thickness	m
δ_m	Sublayer thickness	m
ΔN_η	Real pixel width in η -direction	m
ΔN_ξ	Real pixel width in ξ -direction	m
$\Delta\rho$	Density difference	kg m^{-3}
Δt	Time step	s
ϵ	Void fraction	-

ϵ_a	Threshold void fract. for agglomeration detection	-
ϵ_p	Porosity of perforated plates	-
η	Coordinate	m
η	Interfacial displacement	m
η_0	Initial amplitude of interfacial displacement	m
λ	Vapor wavelength	m
λ_L	Light wavelength	m
λ_{cr}	Critical wavelength	m
μ	Dynamic viscosity	$\text{kg m}^{-1} \text{s}^{-1}$
ν	Kinematic viscosity	$\text{m}^2 \text{s}^{-1}$
ξ	Coordinate	m
ρ	Density	kg m^{-3}
ρ_g	Vapor density	kg m^{-3}
ρ_g''	Modified vapor density	kg m^{-3}
ρ_l	Liquid density	kg m^{-3}
ρ_l''	Modified liquid density	kg m^{-3}
σ	Surface tension	N m^{-1}
$\sigma_{v'}$	Standard deviation of radial fluctuating velocity	m s^{-1}
τ_w	Shear stress	Pa
ϕ	Phase	-
φ	Frequency of occurrence	-
ψ	Turbulence correction	-
ω	Vorticity	s^{-1}

Abbreviations

CAD	Computer Aided Design
CFD	Computational Fluid Dynamics
CHF	Critical Heat Flux
DHI	Digital Holographic Interferometry
DNB	Departure from nucleate boiling
FFT	Fast Fourier Transformation
HIIV	Holographic Interferometric Image Velocimetry
HSP	High-Speed Photography
ONB	Onset of nucleate boiling
PIF	Phase indicator function
PIV	Particle Image Velocimetry

WMS Wire mesh sensor

Dimensionless Numbers

π Pi
 Π_{1-5} Dimensionless number
Re Reynolds number

Subscripts

empty Case with empty channel
g Vapor, vapor phase
l Liquid, liquid phase
max Maximum value
min Minimum value
swirl Case with flow insert

1 Introduction

Boiling processes are widely used in many technical applications due to the high heat transfer rates that can be achieved. Examples include nuclear and conventional power plants, cooling of high performance electronics, evaporation cooled chemical reactors and various other process engineering applications. However, the processes are complex, happening on wide time and length scales with two phases being present and simultaneous transfer of heat and mass. Special technical importance lies in the so called departure from nucleate boiling (DNB) and the accompanying critical heat flux (CHF) that pose a limit to the heat transfer and mark the transition from nucleate into film boiling. As the transition is accompanied with an excursion of the heater temperature that can lead to damage or destruction of the heat transferring equipment, it is desired to operate the equipment at a safe distance to the CHF. Extensive research concerning the CHF phenomenon has been conducted over the last 50 years, however the main effects causing the transition still remain to be fully understood. Apart from a vast number of empirical correlations and look-up tables, a number of so called mechanistic models have been proposed which focus on the physical phenomena leading to the DNB. However, the models vary quite strongly in the underlying assumptions, with some even assuming physically rather questionable mechanisms. One reason for this lack of understanding can be found in the small number of experimentally derived parameters used for the creation of many such models, which in turn is caused by the complexity of the process and the difficulty in accessing it with readily available measuring techniques. One of the aims of this study was therefore to develop and implement new measuring techniques to capture data on up to date unclear mechanisms and to thus contribute in the deepening of the understanding of boiling processes up to CHF and especially of the DNB process itself. The techniques applied for this aim are high-speed photography, digital holographic interferometry, optical microprobes and particle image velocimetry. In addition to the CHF phenomenon in general, only little information exists to date on effects of turbulence and secondary flows on the boiling processes. Therefore, another part of this study deals with the effects of additional

isotropic turbulence and longitudinal vortices on the boiling process along the whole boiling curve.

This thesis is structured as follows: following this introduction, Chap. 2 gives an overview on the phenomena in boiling processes, and discusses available models on the critical heat flux. Furthermore, an overview is given on available measuring techniques, while techniques being applied in the experiments are discussed in further detail. After this, Chap. 3 gives an overview on available measuring techniques and the challenges encountered in analyzing multiphase-flows experimentally. Chap. 4 presents the setup of the used experimental apparatus as well as the measuring techniques, and further describes the methods used for the conduction of the experiments and the derivation of results. The experimental results are described in three separate chapters to offer a more distinguished view on the phenomena in different regimes of boiling. First, Chap. 5 discusses the phenomena observed in fully developed nucleate boiling up to the CHF. After this, Chap. 6 gives an overview on the phenomena encountered in fully developed film boiling. Having thus defined the two boundary regimes for the departure from nucleate boiling, Chap. 7 focuses on the phenomena encountered during the actual CHF transition process. In Chap. 8, the experimental results discussed in the previous chapters are used to give a critical review of existing mechanistic models, and finally provide a concept for a refined phenomenological approach on the CHF phenomenon. Lastly, Chap. 9 provides a summary of the earlier chapters.

2 Boiling phenomena

Boiling is a highly important mechanism of heat transfer and is widely used in a vast number of industrial applications. The high efficiency of the boiling process in comparison to non-evaporative heat transfer lies in the large amount of heat required for evaporation, which makes it possible to reach heat transfer rates orders of magnitude higher than in single-phase systems. However, the two phase system poses a number of challenges in correctly describing the ongoing phenomena. The following chapter shall give an overview of effects taking place in boiling systems, different regimes of boiling as well as models for the description of relevant phenomena. Basic literature on the subject includes the books by Collier and Thome [39], Carey [24], Tong and Tang [127], and Kandlikar [79].

2.1 Modes of boiling

Generally, two main modes of boiling heat transfer are to be distinguished: pool boiling defines a type of boiling without any forced convection, while flow boiling is defined as a boiling process under forced convection. Flow boiling is used far more frequently in industrial applications, as both the heat transfer rates and the controllability of the process are higher. Furthermore, it has to be distinguished between saturated boiling where the fluid is at boiling temperature, and subcooled boiling, where the average temperature of the liquid phase is below boiling temperature. For the results discussed here, only subcooled flow boiling was studied.

2.2 Boiling curve and critical heat flux

For both pool and flow boiling, the characteristic boiling curve first introduced by Nukiyama [107] can be observed as shown in Fig. 2.1. Here, the heat flux \dot{q} is plotted versus the wall superheat ΔT_W , which is defined as the difference between the wall temperature and the boiling point of the fluid.

At low wall superheat up to point A, single-phase convective heat transfer is present. After passing point A, the onset of nucleate boiling (ONB) takes place, leading to a strong increase in heat flux. The evaporation rate increases further, reaching fully developed nucleate boiling at point B and up until the point C, where a sudden excursion in wall temperature and a decrease in heat flux can be observed. As this temperature excursion can likely damage the boiling equipment, point C is often denoted as the boiling crisis, burnout, departure from nucleate boiling (DNB) or the critical heat flux (CHF). Passing point C, the boiling regime transitions from nucleate into film boiling, where a thin film of vapor insulates the heater surface from the bulk flow. The actual mechanisms leading to the CHF have been the subject of a large number of studies over the last decades, and still remain to be fully understood. In the following paragraphs, a detailed discussion shall be given on different CHF types and modeling approaches.

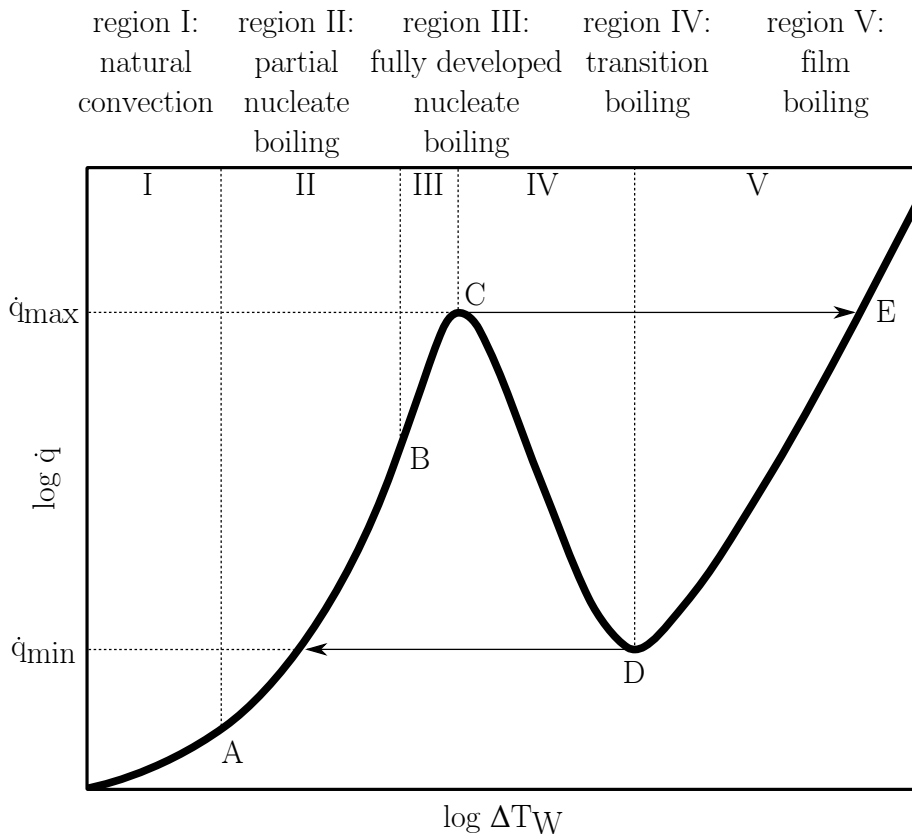


Figure 2.1: Characteristic boiling curve as observed in both pool and flow boiling, showing the heat flux over the wall superheat (adapted and reprinted from [79]).

2.2.1 Types of critical heat flux

Depending on the vapor concentration of the flow with boiling, two different types of critical heat flux have been identified. Firstly, the rather mild CHF denoted as *dryout* occurring at very high vapor qualities, and secondly the severe CHF denoted as *departure from nucleate boiling* (DNB) occurring at low vapor qualities. In systems with high subcoolings and flow rates such as pressurized water reactors, the DNB is the type of CHF typically encountered. Therefore, the focus of this study was also mainly on the departure from nucleate boiling.

2.2.2 Parametric trends in the critical heat flux

The critical heat flux has been shown to depend on a large variety of parameters. For a number of the most common (and most easily varied) parameters such as fluid subcooling, flow rates, system pressure and heater geometries, parametric trends have been identified.

2.2.2.1 Mass flux

The mass flux G directly defines the amount of fresh liquid being transported to the heated areas. Concerning the heat flux, a linear influence of mass flux on the critical heat flux has been shown in a large number of studies, e.g. [28, 79, 99].

2.2.2.2 Fluid subcooling

Fluid subcooling, controlling mainly the components of quench and single phase convection for the overall heat flux as well as the rate of condensation, has also been shown to have a mostly linear influence on the critical heat flux [28, 36, 78, 79].

2.2.2.3 Pressure

System pressure, while affecting the boiling point and therefore the onset of nucleate boiling for a given system, has been shown to have little to no influence on the critical heat flux [28, 36, 78].

2.2.2.4 Heater thickness

The thickness and thus the thermal capacity of the heater has been stated to have a possible influence on CHF. While Celata et al. [33] reported a slight decrease in CHF for an increase in wall thickness from 0.25 mm to 1.75 mm for round tubes with equal inner diameter, Guglielmini and Nannei [60] presented a significant decrease of CHF for thickness below 0.5 mm. Golobic [56] also correlated these effects as an asymptotic critical heat flux being observed for thin heaters. Based on these results, Zhang et al. [141] also pointed out a necessary minimum heater thickness of 0.4 mm. Konishi et al. [88] have also pointed out that very thin heaters tend to give an underestimation of CHF values, because a heat balance with the lower regions of the heater is not possible. This may lead to a dryout below a single bubble being falsely detected as CHF. Here, a minimum wall thickness of 0.4 mm was proposed as well.

2.2.2.5 Channel diameter

A decrease of CHF with increasing channel diameter has been reported by a large number of authors, e.g. [31, 78, 83, 127]. A threshold value for heated length to diameter of 0.3 was reported, above which further increase in diameter has no further influence on CHF.

2.2.2.6 Further parameters

Further parameters such as surface roughness [33], amounts of dissolved gases [79] and non-uniform heating [79] are also sometimes reported as having an influence on CHF. Further discussion of these parameters is omitted here for brevity, mainly because reported influence on CHF appears to be

small, and the parameters do not appear to bear a significant effect on the CHF trigger mechanism.

2.3 Critical heat flux models

Due to the technical importance of the critical heat flux, intensive research has been conducted on the phenomenon. This was further intensified along with the development and installation of the first of nuclear reactors starting in the 1950s and 1960s owing to the high amounts of heat that needs to be transferred from a reactor core. This has led to a large number of different CHF models existing today. The models differ strongly in type, ranging from basic empirical correlations and look-up tables up to more or less physically correct mechanistic models and CFD codes. Comprehensive reviews on the subject have been given for example by Gersey and Mudawar [55], Celata and Mariani [35], Hall and Mudawar [64], Kandlikar [78] and Konishi et al. [88]. The following section shall give a short overview on the most important types of models and their respective capabilities.

2.3.1 Empirical models and look-up tables

Among the first correlations for CHF were empirical correlations derived from experiments in various geometries and fluids. Hall and Mudawar [62–64] presented a large CHF database and compared the data to over 100 available CHF correlations. An obvious disadvantage of these models lies in the limited applicability to the systems from which they were derived, as an extrapolation to conditions other than the ones used in the original experiments is usually not possible. Thus, even with the vast amount of correlations currently available, correct prediction of CHF still poses a challenge. This can also be explained by considering the high number of influencing variables on boiling processes. As discussed by Mudawar [104] and Katto [81], correlations for flow boiling in tubes typically take the form given in Eq. (2.1). In contrast to single phase heat transfer correlations, CHF correlations are far more complex, consisting of a dimensionless group Π_n which itself is a function of numerous independent dimensionless groups each being valid over a limited range [104]. Furthermore, the high cost and complexity of two phase experiments makes data for validation very

scarce, and coverage of the parameters is limited. Also parameters are often grouped together due to limitation to one test fluid, test-rig geometry and orientation, gravity and so on.

$$\begin{aligned} \frac{\dot{q}_{CHF}}{G h_{fg}} &= f\left(\frac{\rho_l}{\rho_g}, \frac{G^2 L}{\sigma \rho_l}, \frac{c_{p,l} T_{sub}}{h_{fg}}, \frac{L}{d}, \frac{G}{\rho_l \sqrt{g_e d}}, \dots\right) = \\ &= f(\Pi_1, \Pi_2, \Pi_3, \Pi_4, \Pi_5, \dots) \end{aligned} \quad \left\{ \begin{array}{l} \Pi_{1,min} < \Pi_1 < \Pi_{1,max} \\ \Pi_{2,min} < \Pi_2 < \Pi_{2,max} \\ \Pi_{3,min} < \Pi_3 < \Pi_{3,max} \\ \Pi_{4,min} < \Pi_4 < \Pi_{4,max} \\ \Pi_{5,min} < \Pi_5 < \Pi_{5,max} \\ \dots \end{array} \right. \quad (2.1)$$

To provide a better data base, several groups have presented reviews of available CHF data from vast numbers of sources. Hall and Mudawar [63, 64] as well as Groeneveld et al. [57, 59] presented databases or look-up tables for CHF with more than 30,000 data points each, serving a wide range of parameters. These databases allow for a good comparison of available data and verification of empirical correlations, but still offer no insight into the actual mechanisms leading to the CHF.

2.3.2 Mechanistic models

To improve calculation of the critical heat flux over the empirical models, so called phenomenological or mechanistic models were developed based on actual physical mechanisms leading up to the CHF. These types of models offer a potentially higher validity, provided the correct identification of the mechanisms. These models have so far mainly seen use in academia, while for industrial applications the use of empirical correlations is still favored [132]. However, a correct phenomenological description of the actual trigger mechanisms for CHF may not only improve the accuracy of calculations but also help to find measures to prevent or postpone the departure from nucleate boiling. Especially regarding the implementation of correct boiling models into CFD codes, mechanistic models offer a clear advantage over empirical approaches. A number of different mechanisms have been presented, most of which were developed based on experimental studies, largely by use

of photographic methods [20]. In the following paragraph, the four most recently used types shall be presented and discussed, these are namely the *boundary layer separation model*, the *bubble crowding model*, the *sublayer dryout model* and the *interfacial lift-off model*. Fig. 2.2 shows a simplified illustration of the general assumptions on the vapor behavior for these four models [88]. It illustrates the phenomena at an operating point shortly prior to the transition, denoted as CHF(-) and at an operating point shortly after the transition, denoted as CHF(+). The following section shall describe the four discussed models shortly and give a brief introduction of the basic parameters and principles of calculation to illustrate the fundamentals of each of the models.

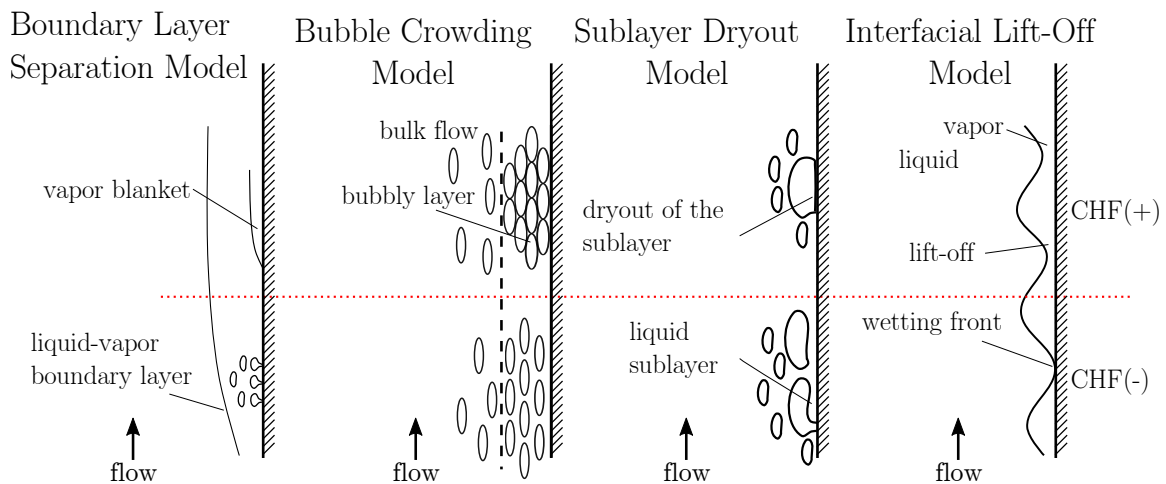


Figure 2.2: Schematic representation of the DNB trigger mechanisms for different mechanistic models, showing fully developed nucleate boiling at CHF(-) (lower part) and right after the occurrence of the DNB (upper part, denoted as CHF(+)). Adapted and reprinted from [88].

2.3.2.1 Boundary layer separation model

The *boundary layer separation model*, also denoted as separated flow model, is one of the oldest phenomenological models on CHF, see e.g. Tong [126]. The model assumes vapor as being injected into the liquid similar to gas flow through a porous plate, forming a vapor layer which separates the bulk liquid flow from the wall (see Fig. 2.2). The boiling crisis is postulated to occur following the formation of a vapor blanket above the porous plate, which leads to stagnation of the liquid flow to the heater. The liquid sublayer then evaporates, leading to an increase in the heater surface temperature above

the Leidenfrost temperature, thus inducing DNB. The correlations derived from these model assumptions still incorporate a large number of empirical constants, furthermore the basic mechanism was observed to have a weak physical basis [91]. For these reasons, the model has seen little application over the last two decades.

2.3.2.2 Near wall bubble crowding model

The *near wall bubble crowding model* assumes the loss of quenching and subsequent CHF to be caused by a rising concentration of vapor bubbles near the heater surface, which prohibits turbulence in the bulk flow from penetrating the vapor layer and transport fresh liquid to the heater surface. It is assumed that this happens at a critical vapor fraction in the vapor layer, which is derived from a geometrical balance of given bubbles that begin to coalesce after reaching the critical vapor fraction. Within the bubbly layer, homogeneous flow of vapor bubbles and liquid is assumed. The mechanism was first proposed by Weisman and Pei [133], based on previous work by Hebel et al. [67, 68]. The original model assumed homogeneous flow of vapor bubbles and liquid within the bubbly layer. Ying and Weisman [137] expanded the model to lower mass velocities, replacing the homogeneous flow model with a slip model taking into consideration the buoyancy effects of larger bubbles. Lim and Weisman [94] also applied the model to flow in channels with partial heating, while Yang and Weisman [136] further expanded the model for calculation of pre-CHF heat fluxes throughout the detached bubble region. The model was based mainly on a small number of visualization studies. In order to discuss the relevant quantities for the use of each of the mechanistic models, a very short overview shall be given citing the main equations. For the bubble crowding model, turbulent interchange at the edge of the so called bubbly layer close to the heater surface is assumed to be the limiting process in boiling heat transfer. The bubbly layer edge is assumed as the position where the Prandtl mixing length is equal to the bubble diameter multiplied by the empirical constant k (given as 2.5) [133]. The turbulence intensity i_b at the bubbly layer edge is calculated as a function of the Reynolds number, the ratio of bubble diameter D_p to

the pipe diameter d and the liquid and vapor densities ρ_l and ρ_g , with the empirical constants k and a according to Eq. (2.2) [133].

$$i_b = 0.426 k^{0.6} Re^{-0.1} \left(\frac{D_p}{d} \right)^{0.6} \left[1 + a \left(\frac{\rho_l - \rho_g}{\rho_g} \right) \right] \quad (2.2)$$

To correct for turbulence not reaching the wall due to radial vapor production, the quantity ψ was defined as a function of the radial velocity created by vapor generation v_{11} and the standard deviation of the radial fluctuating velocity $\sigma_{v'}$ as given in Eq. (2.3).

$$\psi = \frac{1}{\sqrt{2\pi}} \exp \left[-0.5 \left(\frac{v_{11}}{\sigma_{v'}} \right)^2 \right] - 0.5 \left(\frac{v_{11}}{\sigma_{v'}} \right) \operatorname{erf} \left(\frac{v_{11}}{\sqrt{2}\sigma_{v'}} \right) \quad (2.3)$$

Using Eq. (2.2) and Eq. (2.3), the lateral mass flux from the core to the bubbly layer due to turbulent interchange G' was defined for a total axial mass flux G as given in Eq. (2.4).

$$G' = \psi i_b G \quad (2.4)$$

Finally, the critical heat flux \dot{q}_{CHF} was given as a linear function of G' as shown in Eq. (2.5).

$$\dot{q}_{CHF} = G' h_{fg}(x_2 - x_1) \left(\frac{h_f - h_{ld}}{h_l - h_{ld}} \right) \quad (2.5)$$

With the enthalpies of evaporation h_{fg} , of liquid h_l , saturated liquid h_f and at point of bubble detachment h_{ld} . x_1 and x_2 are the average qualities in the core region and bubbly layer, respectively. For swirl flows, Weisman et al. [134] correlated i_b with correction for swirl flow shear stress τ_w , bubble size d_b and equivalent diameter D_e as given in Eq. (2.6), giving a direct scaling of critical heat flux with increasing turbulent intensity.

$$\frac{i_{b,\text{swirl}}}{i_{b,\text{empty}}} = \left(\frac{\tau_{w,\text{swirl}}}{\tau_{w,\text{empty}}} \right)^{0.5} \cdot \left(\frac{d_{b,\text{swirl}}}{d_{b,\text{empty}}} \right)^{0.6} \cdot \left(\frac{D_{e,\text{empty}}}{D_{e,\text{swirl}}} \right)^{0.6} \quad (2.6)$$

It has been commented by a number of researchers [28, 35, 91, 139] that a major weakness of this model lies in the assumption of CHF to occur at a certain critical vapor fraction. Weisman and Pei [133] provided a value of 82 % for this critical fraction, which was however observed to vary widely for differing mass fluxes and subcoolings by Styrikovich et al. [123].

2.3.2.3 Sublayer dryout model

The *sublayer dryout model*, first introduced by Lee and Mudawar [91] based on an older model with similar mechanism by Haramura and Katto [65], has received increased attention over the last twenty years [28, 29, 82, 83]. According to this model, CHF occurs when a liquid sublayer present under the vapor bubbles during nucleate boiling cannot be replenished from the bulk flow any more and evaporates, creating a dry spot on the heater surface. The model was originally developed for pressures of more than 5 MPa, but was also expanded for lower pressure systems by Katto [84]. Celata et al. [28] provided a rationalization of the model, which enabled the exclusion of most empirical constants. It was further expanded by Celata et al. [36] for cases with non-uniform heating and swirl flow. The swirl was accounted for by modifying the friction factor. To overcome some inconsistencies of the original sublayer dryout model, Celata et al. [31] developed the *superheated layer vapor replenishment model*, which assumes a liquid layer at saturation temperature (superheated layer) close to the heater surface that dries out at CHF and is replenished by a vapor blanket. The model was mainly developed for high mass fluxes and liquid subcoolings. Since a main assumption is an isolated layer of liquid close to the heater surface as the only possible position for vapor bubbles, the authors of the model state a loss of validity when local thermodynamic conditions at CHF approach the saturated state of the liquid bulk [31]. The model basics have mainly been developed from visualization studies on small scale experiments, such as the falling film evaporation study by Mudawwar et al. [105]. Experimental validation for the model on larger scale boiling experiments is scarce, mainly because the postulated thin sublayer is challenging to access with available measuring techniques. It also has to be noted that experimental studies using very thin heaters, such as the study by Hino and Ueda [70] (given by Lee and Mudawar [91] as one of the sources for the model) using a 0.5 mm thick heated tube, tend to overestimate the effects of larger bubbles. It has been commented, e.g. by [88] that the thin surface and therefore small heat capacity of such systems leads to an underestimation of the values for the CHF. This is due to the fact that the temperature cannot be balanced by heat capacity of the heater, making every larger bubble departing the heater cause an unrealistic dryout effect. Also, as with the other mechanistic models, all versions of the sublayer dryout model still contain a number

of empirically derived parameters. Fig. 2.3 shows the assumptions for vapor distribution and the schematic representation for the onset of sublayer dryout as given by Lee and Mudawar [91]. Again, a short overview shall be

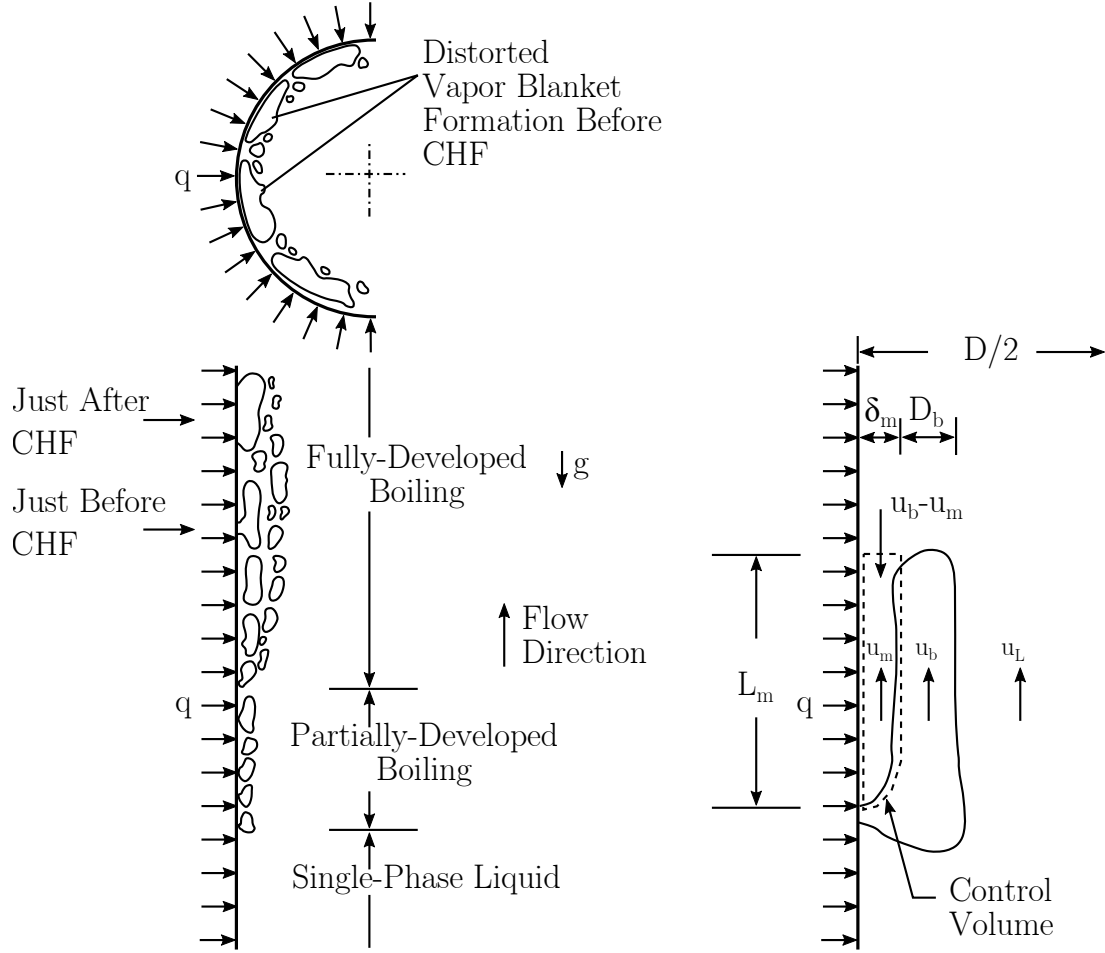


Figure 2.3: Phase distribution just before and just after CHF according to the sublayer dryout model. Adapted and reprinted from [91].

given on the basic modeling approach. For the sublayer dryout model, the critical heat flux \dot{q}_{CHF} is given as a function of the relative mass flux G_m , the sublayer thickness δ_m and the length of the vapor blanket L_m , as well as the thermohydraulic parameters such as the saturated liquid temperature T_{sat} , the temperature of the liquid entering the sublayer T_L , the specific heat of the liquid $c_{p,l}$ and an empirical constant a_1 (as given by Lee and Mudawar [91]), see Eq. (2.7).

$$\dot{q}_{CHF} = \frac{G_m \delta_m [h_{LG} + a_1 c_{p,l} (T_{sat} - T_L)]}{L_m} \quad (2.7)$$

The vapor blanket velocity U_b is given as a function of the vapor blanket length L_m , gravity g , density difference $\Delta\rho$, liquid density ρ_l , drag coefficient c_D and a mean liquid velocity close to the vapor plumes U_{bL} , see Eq. (2.8).

$$U_b = \left(\frac{2L_m g \Delta\rho}{\rho_l c_D} \right)^{0.5} + U_{bL} \quad (2.8)$$

Vapor blankets are formed by coalescence of small bubbles, creating elongated vertical cylinders/bubbles, with the length of the sublayer and the vapor blanket L_m equal to the critical Helmholtz wavelength, see Eq. (2.9), with the bubble velocity U_b and the mean liquid velocity U_m .

$$L_m = \frac{2\pi\sigma(\rho_l + \rho_g)}{\rho_l\rho_g(U_b - U_m)^2} \quad (2.9)$$

Considering U_m is very small in sublayer, Eq. (2.9) can be rewritten as:

$$L_m = \frac{2\pi\sigma(\rho_l + \rho_g)}{\rho_l\rho_g U_b^2} \quad (2.10)$$

The sublayer thickness can be expressed as given in Eq. (2.11), where a_1 and a_2 indicate empirical constants [91].

$$\delta_m = \frac{0.421a_2 \text{Re}^{(a_3-0.1)} G \rho_g h_{LG}^2 d_b}{[\dot{q}_{\text{CHF}} - a_1 h_{SC} (T_{\text{Sat}} - T_L)]^2} \cdot \left(1 + \frac{\delta_m}{\delta_m + d_b} \right) \left(\frac{gL_m \Delta\rho}{\rho_l c_D} \right)^{0.5} \quad (2.11)$$

2.3.2.4 Interfacial Lift-Off model

Another recent model is the *interfacial lift-off model*. In sharp contrast to the sublayer dryout model, this model focuses on the global behavior of the vapor rather than local microscopic effects. Here, a periodic behavior of the vapor layer along the whole heated length is postulated, with waves of higher void fractions alternating with so called wetting fronts, where liquid can access the heater. At DNB, the wetting fronts are assumed to lift-off from the heater surface, leading to liquid blockage and subsequent CHF. The model was first proposed by Galloway and Mudawar in [50, 51] based on photographic studies in a rectangular channel of 1.6x6.4 mm² with a copper heater and FC87 as boiling fluid. Galloway and Mudawar [50] defined three different regimes to be observed from ONB up to CHF. In the *discreet bubble regime* up to 40% of CHF, isolated bubbles were observed, while in

the *coalescent bubble regime* at up to 60% of CHF coalescence and formation of larger bubbles were observed. This led to the final *wavy liquid-vapor layer*, where all bubbles were observed to coalesce into a continuous vapor layer periodically touching the heater surface. Vapor wavelengths were reported in the range of 3 to 6 mm with amplitudes of 0.7 to 1.8 mm. Zhang et al. [138, 140] later conducted experiments with a different orientation of the heater surface relative to gravity which revealed more flow regimes. For vertical upflow however, the three aforementioned regimes were confirmed. The areas where the vapor layer touches the heater surface and thereby allows for access of liquid are denoted as *wetting fronts*. These are assumed to be the main mechanism of heat transfer in the wavy vapor layer regime. At CHF, the wetting front at the leading edge of the heater was observed to be lifted off from the heater surface, caused by a vigorous effusion of vapor beneath the front [50]. This led to further increases in heater temperature, culminating in the departure from nucleate boiling. Fig. 2.4 shows the cycle of events leading to CHF as given by [50]. This model was further developed by Gersey and Mudawar [55], Sturgis and Mudawar [121, 122] and Zhang et al. [139, 142]. Kharangate et al. [85] expanded the model for use with vapor at the inlet. As for the other mechanistic models, a short description of the basic modeling approach shall be given in the following paragraphs. For this model, the periodic behavior of the vapor layer is described as a wavy interface, the basic behavior of which can be described by classical hydrodynamic instability. The Helmholtz instability caused by the difference in velocity between the two phases leads to a critical wavelength λ_{cr} as given in Eq. (2.12) for a vertically orientated channel [121]. For other orientations, the body force has to be taken into account as well [140]. In contrast to the classical Helmholtz instability applied in the sublayer dry-out model (see Eq. (2.9)), a modified density term is used for both liquid and vapor density, taking into account the thickness of the respective layers: $\rho''_{l/g} = \rho_{l/g} \cot(k_w H_{l/g})$ with liquid/vapor layer thickness $H_{l/g}$ and wave number k_w .

$$\lambda_{cr} = \frac{2 \pi \sigma (\rho''_l + \rho''_g)}{\rho''_l \rho''_g (\bar{U}_g - \bar{U}_l)^2} \quad (2.12)$$

As the trigger mechanism, separation of wetting fronts from the wall is postulated, confirmed by photographic study. The curvature of the liquid-vapor interface generates a pressure force that promotes contact of the interface with the heated wall, enabling liquid access. CHF occurs when the mo-

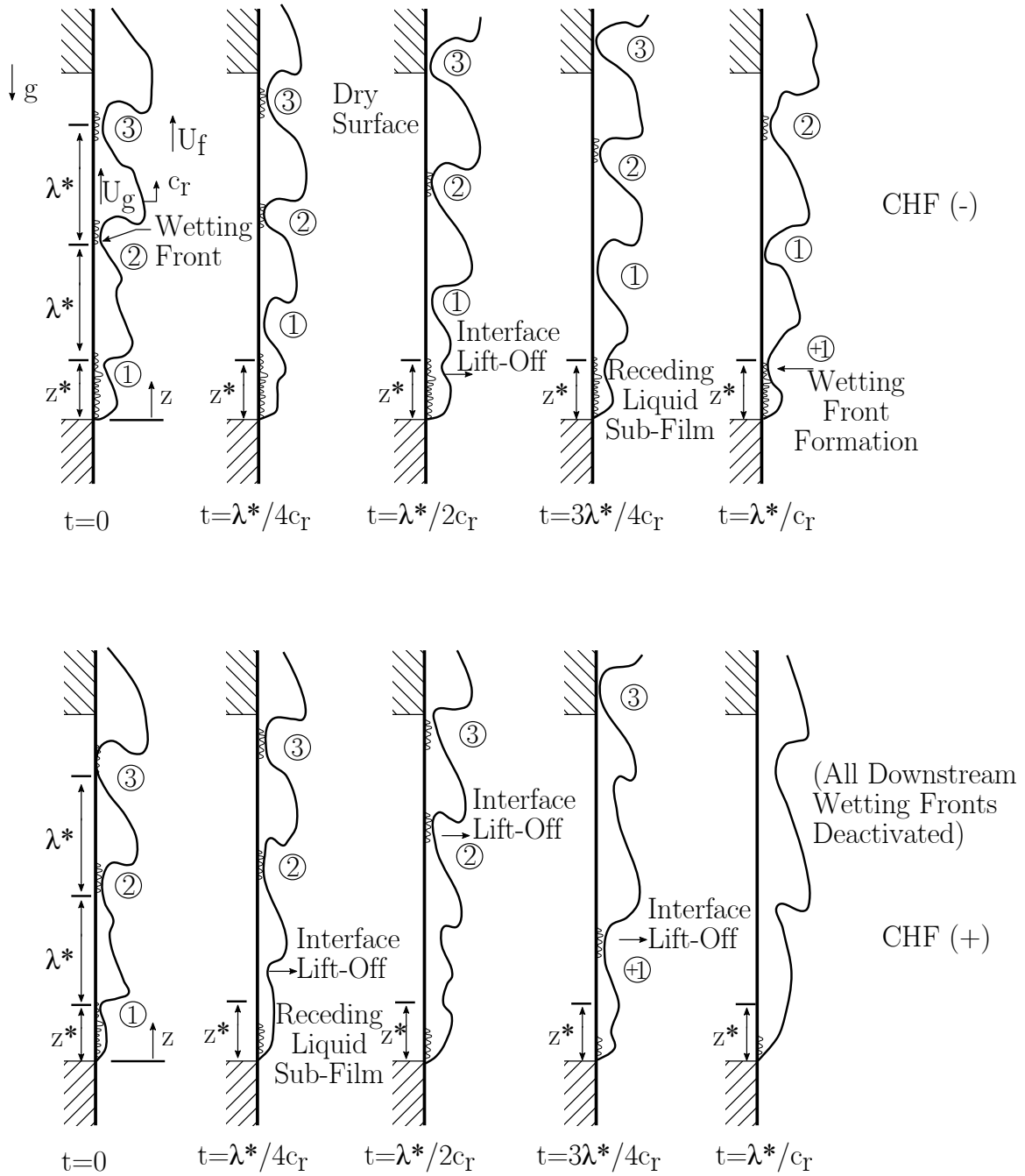


Figure 2.4: Illustration of complete cycle of events leading up to the DNB according to the interfacial lift-off model, observed at 99% CHF (CHF(-), above) and 101% CHF (CHF(+), below). Adapted and reprinted from [50].

mentum of generated vapor normal to the heated surface just exceeds the pressure force. For an assumed interfacial wave shape of $\eta(z, t) = \eta_0 e^{ik(z-ct)}$,

the pressure difference perpendicular to the wall is expressed as given in Eq. (2.13) [88].

$$p_l - p_g = - \left[\rho_l''(c - \bar{U}_l)^2 + \rho_g''(c - \bar{U}_g)^2 + (\rho_l - \rho_g) \frac{g_n}{k_w} \right] k_w \eta_0 e^{ik_w(z-ct)} \quad (2.13)$$

It is assumed that the wetting fronts occupy a fixed fraction b of the critical wavelength, therefore the average pressure force for the wetting fronts is calculated by averaging the pressure difference over $b \lambda_{cr}$ [88].

$$\overline{p_l - p_g} = \frac{4\pi\sigma\delta}{b\lambda^2} \sin(b\pi) \quad (2.14)$$

The parameter b is given as 0.2 by Sturgis and Mudawar [121, 122] based on photographic studies. In subcooled flow boiling, heat in the wetting front is consumed by vaporizing liquid, as given in Eq. (2.15), where A_w is the wetting front area.

$$\dot{q}_w A_w = (c_{p,l} \Delta T_{sub,in} + h_{fg}) \rho_g U_{g,n} A_w \quad (2.15)$$

The local heat flux required to push the interface away from the wall \dot{q}_w is determined by equating the vapor momentum $\rho_g U_{g,n}^2$ to the pressure force obtained from Eq. (2.14) [88].

$$\begin{aligned} \dot{q}_w &= \rho_g (c_{p,l} \Delta T_{sub,in} + h_{fg}) \sqrt{\frac{\overline{P_l - P_g}}{\rho_g}} \\ &= \rho_g (c_{p,l} \Delta T_{sub,in} + h_{fg}) \left[\frac{4\pi\sigma \sin(b\pi)}{b\rho_g} \right]^{1/2} \frac{\delta^{1/2}}{\lambda_{cr}} \Big|_{z^*} \end{aligned} \quad (2.16)$$

The critical heat flux \dot{q}_{CHF} is defined as the average heat flux over the entire heated area, which relates to the wetting front heat flux by the relation $q_m'' = b q_w''$. From this, Eq. (2.17) is derived.

$$\dot{q}_{CHF} = \rho_g (c_{p,l} \Delta T_{sub,in} + h_{fg}) \left[\frac{4\pi\sigma b \sin(b\pi)}{\rho_g} \right]^{1/2} \frac{\delta^{1/2}}{\lambda_{cr}} \Big|_{z^*} \quad (2.17)$$

Here, δ and λ_c are calculated at the coordinate z^* , determined from a separated flow model used for prediction of the velocities $U_l(z)$, $U_g(z)$ and the vapor layer thickness $\delta(z)$.

2.3.2.5 Mechanistic models: summary and conclusions

The fact there are at least four different mechanistic models currently being used indicates that there is still confusion as to what actually triggers the departure from nucleate boiling. The basic model assumptions differ quite significantly in parts. This can be explained by the limited amount of experimental data on which the models were based. Most models were mainly deduced from photographic studies. Unfortunately, this technique leaves out a significant number of variables and offers limited access to the crucial high void vapor layer close to the heater surface. Still, all models have shown good validity for the data on which they were developed. However, each model still comprises noteworthy empiricism, at least in some parts, despite the mechanistic base approach. Thus, it is still unclear which of the proposed mechanisms, if any, actually causes the DNB. Also, as Weisman [132] points out, several models may be correct due to imprecise definition of the actual CHF event itself: while e.g. the bubble crowding model focuses on the behavior of the global vapor layer shortly before CHF, the sublayer dryout models focus on local sublayer behavior at or even slightly after CHF. As a result, the actual trigger mechanism still needs to be identified more clearly. It is the author's opinion that this can only be achieved with an improved experimental approach, utilizing measuring techniques that can complement the photographic technique to gain access to parameters in the liquid bulk flow and especially inside the vapor layer close to the heater surface. For this, Chap. 3 shall give an overview of currently available measuring techniques applicable in boiling research, and point out the aims of the experimental program.

2.4 Description of post-CHF boiling - fully developed film boiling

As the nucleate boiling regime is the desired operation mode for most industrial applications due to the high transferable heat fluxes, many studies focus mainly on the prevention of the CHF and the mechanisms leading to it, dismissing the film boiling regime as an unwanted state. However, there is quite a number of applications where film boiling is not only the prevalent but also the desired regime. These applications are mainly found in

systems operated at low temperature and pressures, as typical in cryogenic applications. For example, the vaporization of liquid nitrogen is usually done by film boiling of the nitrogen on a heat exchanger with water as the heating medium. For such applications, it is of high interest to sufficiently describe the film boiling process. In contrast to nucleate boiling, the heat transfer mechanisms in film boiling are rather straightforward and can be described comparatively simply [39]. Fig. 2.5 shows a sketch of the two phase behavior and the different modes of heat transfer prevalent in film boiling. As the vapor film completely separates the heater surface from the liquid phase, heat is transferred via conduction from the wall to the vapor film (q_w), by conduction from the vapor film interface to the liquid phase (q_i) and by radiation (q_r). The flow can typically be treated as fully separated gas/liquid flow [79]. Rather few experimental results are available on

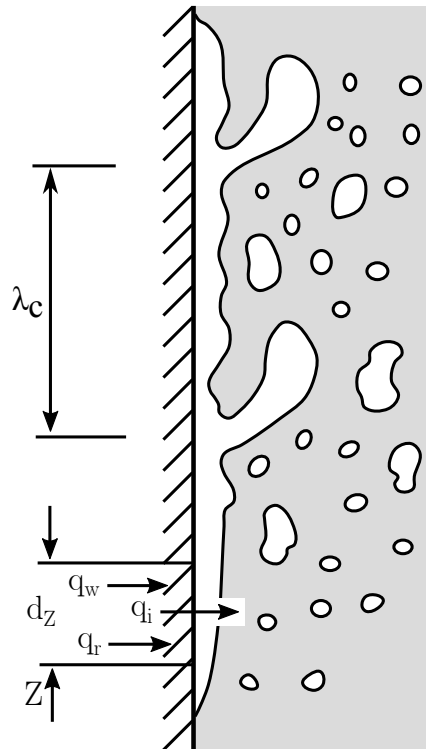


Figure 2.5: Schematic of vapor behavior in film boiling regime. Adapted and reprinted from [39].

the film boiling process, which is partly a result of the more difficult experimental approach due to the higher required temperatures and partly due to the smaller technical relevance in comparison to nucleate boiling and CHF. Some studies were conducted in pool film boiling [80, 129], most notably one conducted by Buchholz et al. [23], who used an optical microprobe with

a tip diameter of approx. $1.5\ \mu\text{m}$, to perform measurements along the entire boiling curve and into film boiling. It could be shown that for film boiling of Isopropanol and FC-3284 film thicknesses (void fraction $\epsilon > 0.3$) of approximately 0.25 to 0.5 mm could be observed. To the authors knowledge, while many correlations have been derived on heat transfer in film boiling [39, 58, 79], little to no actual experimental results have been published on the two-phase behavior and heat distributions in the liquid for film boiling under forced convection. Therefore, one aim of this study was to also shed some light on the two-phase behavior and heat distributions in fully developed film flow boiling.

2.5 Influence of turbulence and secondary flows on boiling processes

Turbulence describes the rapid variation of various properties within a fluid flow. Secondary flows are minor flows superimposed on a primary flow, such as a longitudinal vortex in a main flow. Considering the influence of mass flux and fluid subcooling on boiling processes discussed in Sec. 2.2.2, similar influences might be expected by increased turbulence and/or secondary flows in the system. Possible influences include increased transport of subcooled liquid towards the heated surface, increased removal of vapor from the heated surface, and enhanced mixing within the liquid phase. However, only few researchers have commented on the influence of turbulence and secondary flows on the mechanisms leading to CHF. A number of empirical correlations exist taking into account the effects of spacer grids in nuclear reactor bundles, such as the Westinghouse correlation [37]. Some reports have been given on the influence of twisted tapes in pipes [2, 30, 44, 45, 73, 74, 134] for which typically the increased velocity perpendicular to the main flow is discussed as main reason for higher heat fluxes. To the authors knowledge, no results have so far been published giving detailed information on the phenomena leading to the DNB and the influence the flow inserts can have on them. One central aim of the project was therefore to provide insight on the effects of added turbulence and longitudinal vortices on the boiling process. Turbulence and vortices were therefore artificially created by placing flow inserts of different geometries at the inlet of the test chamber.

To quantify the effects of the used inserts, characteristic parameters for the turbulent flow must be defined. For this study, the turbulence intensity Tu was used as parameter to define the effects strength and penetration depth for near isotropic turbulence and vorticity ω as a measure for the longitudinal vortices. These parameters shall be defined in the following paragraph.

2.5.1 Turbulence intensity

Turbulent flows can be characterized by the fluctuations of the fluid velocities u and v . The velocity fluctuations in horizontal and vertical direction, u', v' are defined as given in Eq. (2.18) [108].

$$u' = u - \bar{u}, \quad v' = v - \bar{v} \quad (2.18)$$

In this study, the turbulence intensity is used as the main parameter for analysing the turbulence present in the flow. The turbulence intensity is the root mean square of the velocity fluctuations in horizontal and vertical directions, u' and v' , normalized by the average velocity \bar{U}_l :

$$Tu = \frac{\sqrt{\frac{1}{2}(u'^2 + v'^2)}}{\bar{U}_l} \quad (2.19)$$

Turbulence created by grids decays very rapidly due to damping effects. According to literature, isotropic turbulence intensity decays exponentially with the distance $y - y_0$ downstream of the grid position y_0 [53]. Comte-Bellot and Corrsin [40] presented Eq. (2.20), with A_1 , M and n being coefficients for the particular grid geometry.

$$Tu = A_1 \cdot \left(\frac{y - y_0}{M} \right)^{-n} \quad (2.20)$$

For the plates used in this report, Roach [113] suggested a value of $-5/7$ for the exponential coefficient n .

2.5.2 Vorticity

To define the intensity of vortices, the vorticity ω is typically used as given for a plane flow in Eq. (2.21) [135].

$$\omega = \left(\frac{\partial v}{\partial x} - \frac{\partial u}{\partial y} \right) \quad (2.21)$$

3 Measuring techniques

3.1 Challenges and techniques in boiling experiments

Boiling processes pose a number of challenges for experimental investigations: the processes in boiling are usually very fast and happening on length scales from microscopic to several meters. High acquisition rates are needed, but also long observation times, high magnification for insight into microscopic phenomena as well as observations over larger areas up to the whole channel length. Many studies have been presented based on photographic recordings, e.g. [32, 49, 61, 142], which have greatly enhanced the understanding of the CHF. Still, as the photographic technique has a number of limitations, some questions regarding the DNB transition can not be answered with this method. Mainly, the following parameters are difficult to derive from photographic studies despite their importance for the boiling process: firstly, photographic methods are mainly limited to observations of the disperse (usually the vapor) phase, while the motion of the continuous phase remains inaccessible. Furthermore, even for the vapor, photographic methods fail to provide information about changes in the vapor flow at higher void fractions due to their integrative nature. Especially for larger channels with high numbers of bubbles, this poses a serious shortcoming. In addition to this, the temperature distribution in the fluid cannot be visualized. The following section shall give an overview of currently available measuring techniques and possible applications in boiling research. General reviews on measurements in multiphase flows have been given by Hewitt [69] and Boyer et al. [19]. Further books with emphasis on optical techniques include [93] and [102]. For boiling systems, a number of further constraints have to be considered:

- Usually at least one direction of view is blocked by the heater.
- At higher void fractions the flow becomes opaque, blocking access for optical techniques.

- Particles used for flow visualization may adhere to the hot heater surface, disturbing the heat transfer and liquid access.

For the two phase area, it can be distinguished in general between invasive techniques which are inserted into the flow directly, possibly affecting it, and non-invasive techniques which have no contact to the flow. The most important of these techniques shall be described in the next section. In addition to the measurement of parameters within the two phase region, the detailed measurement of heat flux and surface temperature within the heater also requires a sophisticated design of the heater and the measuring techniques. These shall also be discussed.

3.2 Overview on available measuring techniques

A large number of different measuring techniques have been used and proposed for boiling research, for which the following paragraph shall give a short overview. A general distinction can be made between *non-invasive techniques* that do not affect the flow itself and *invasive techniques* that are somehow in contact with the flow.

3.2.1 Non-invasive techniques

Non invasive techniques have been very commonly used in boiling research, and are still favored today because they do not affect the phenomena during the measurement. However, the techniques typically require more complex setup and/or have limited access to some areas. The most important non-invasive techniques shall be discussed in the following sections.

3.2.1.1 Photography

One of the most important non-invasive techniques is the photographic or videometric technique. The technique has evolved from standard single image photography to high-speed photographic methods at acquisition rates of several thousand images per second. Photographic techniques have been used e.g. by [32, 49, 50, 61, 86, 98, 122, 142], among many others. Properties that can be examined using photographic techniques include mainly

the vapor characteristics, i.e. bubble size and motion as well as vapor concentration and shapes. The reasons for the high popularity of the methods are the relatively simple setup and the easy interpretation of the results. While early studies used time consuming manual approaches to analyze the photographs, current work relies heavily on numerical processing of the images. However, despite the straightforward nature of the photographic images, the technique is also prone to misunderstandings, resulting from the numerical interpretation but also from inherent features of the technique: photographic techniques are depth integrating by nature, but also suffer from a limited field of depth. Furthermore, currently available cameras are still limited to image numbers of around 10.000. This limitation of images can result either in too short recording times with small intervals between the images, not allowing to observe the effects on longer timescales (transition processes, passing of periodic events in the vapor layer), or long recording times with too long intervals between the images, not allowing for observation of effects like bubble formation, breakup and coalescence. Therefore, while photographic techniques still remain one of the most important measuring principles in boiling research, the results have to be analyzed carefully. Also, it appears sensible to combine photography with another measuring technique to compensate for its shortcomings.

3.2.1.2 Particle image velocimetry

One of the most common techniques to measure parameters within the liquid phase is the particle image velocimetry (PIV). This technique uses particles that are inserted within the flow as tracers. The particles are illuminated with a light sheet, typically produced by a laser. The images are recorded using a standard camera, and velocity fields can be derived using cross-correlation algorithms [109, 112]. The use of particles makes this method only partly non invasive, as the particles can adhere to the heater surface, leading to the creation of artificial nucleation sites or an insulating layer. PIV can be used to analyze wide variations of geometries, see e.g. the use by Maurus in a $40 \times 40 \text{ mm}^2$ channel with multiple bubbles [99] or for observing the formation of bubbles at a single nucleation site as shown by Basic et al. [3].

3.2.1.3 Other techniques

A large number of other non-invasive techniques for measuring parameters in the two-phase flow have been proposed, most of which require either a specially designed heater or an otherwise highly sophisticated and costly setup. The following paragraph shall give a short overview on some of these techniques.

- Shadowgraphy and Schlieren provide a rather simple and robust setup for visualization of density gradients in transparent media. A detailed description of the optical setup can be found in Davies [43], while a comparison to interferometric techniques was given by Desse and Deron [47] and by the author in [11]. The technique was also used for the determination of velocity fields in turbulent flows by Hargather et al. [66], Jonassen et al. [76]. As discussed in [11, 47] the technique is less sensitive than interferometric methods but offers a far simpler setup and requires little to no post processing of data.
- Holography, digital holography and holographic interferometry are interferometric techniques that can be applied for the three dimensional evaluation of flows (holography) and the visualization of density gradients (holographic interferometry). These techniques are described in detail in section Sec. 3.3.

Further, but rather seldom used and not widely available techniques include thermochromatic liquid crystals [120], radiographic techniques such as γ -ray and x-ray densitometry and tomography [4, 119] and further techniques. All these techniques are highly sophisticated and may become of great interest for boiling research in the future. For reasons of brevity however, they shall not be discussed in further detail here.

3.2.2 Invasive techniques

As discussed above, while any operator would usually prefer using only non-invasive techniques, the inherent shortcomings make the use of some invasive measuring devices inevitable [19]. The main advantage of invasive

techniques lies in their ability to measure parameters locally, thus often giving more precise measurements with less need for interpretation. However, the invasive nature of these techniques and their influence on the observed process itself have to be taken into account.

3.2.2.1 Thermocouples

Thermocouples form the most basic measuring technique and provide the backbone for most heat transfer experiments. Typically at least one thermocouple is placed at in- and outlets of the channels.

3.2.2.2 Wire mesh sensors

Wire mesh sensors (WMS) have been introduced as a two-dimensional measuring technique for multiphase flows by Prasser et al. [110]. The technique uses a mesh of two layers of parallel wires, perpendicular to each other and with a height difference of around 1.5 mm that are inserted in the cross section of the observed flow. The sensor measures the conductivity or the capacitance [41, 42] between each wire crossing at recording frequencies of several kHz. The technique allows for a very sophisticated two-dimensional observation of the two phase flows, however the high amount of wires make it strongly invasive. The wires can also lead to a fragmentation of bubbles, as shown in [111]. A comparison to γ -ray densitometry was given in [119]. For use in boiling applications, the WMS is typically restricted to measurements of the vapor distribution in the non heated areas, i.e. in the in- and outlet of the heated sections as an implementation on the heated surface appears unfeasible.

3.2.2.3 Probe measurements

Electrical and optical probes can be used to detect different phases at the tip of the probe, using either conductivity, capacitance or refractive index as an indicator. Probe measurements can offer similar point wise information on vapor behavior in multiphase flows as the wire mesh sensors, but only offer one measuring position. However, the simpler setup and higher flexibility make the positioning of probe measurements very versatile. Conductive and

capacitance probes have been described in detail by Schleicher et al. [116], while a comparison to WMS is given by Manera et al. [96]. Optical probes are less widely used than the electrical ones, but offer a thinner geometry and thus less influence on the flow. Furthermore, as the refractive index is measured, optical probes are independent of conductivity changes and can be used for a wider array of fluids, e.g. water and organic systems. For these reasons, optical probes were developed for the use in the boiling experiments discussed here. A detailed description of the used probes is given in Sec. 4.3.3 and in [14].

3.2.3 Measuring of parameters in the solid parts

Even outside of the two phase flow, a number of parameters prove challenging to measure. These include the actual surface temperature of the heater as well as the heat flux being transported to the boiling liquid. A very basic and robust approach to measure the heater temperature was applied by Celata et al. [34], who used an electrically heated rod as heater, the temperature of which was measured using the elongation of the rod via a displacement sensor. However, such measurements only provide integrative information on the temperatures in the heater. Typically, several rows of thermocouples are implemented in the heater, from which heat fluxes can be calculated and surface temperatures can be extrapolated. For this, a certain thickness of the heater is required to allow for insertion of at least two thermocouples. However, the technique offers a highly robust and reliable measurement of both heater surface temperature and heat fluxes, and can also be placed at different heights along the heater. Further techniques include infrared imaging [54, 131], which offers a two-dimensional measurement of temperatures on the heater surface. However, this technique requires a very sophisticated heater construction, typically a thin foil that makes CHF difficult to reach. The technique is therefore more typically used to investigate nucleate boiling in the region of ONB. Another approach was taken by the group of Kim et al. [46, 87, 92, 106, 115] who applied an array of 96 specially designed, each $0.1 \times 0.1 \text{ mm}^2$ large microheaters under various gravity levels. The heaters could be separately supplied with electricity. However, CHF is also not accessible using this heating system.

Furthermore the highly sophisticated design of the heaters does not allow for the technique to be widely applied.

3.2.4 Summary on available measuring techniques

It can be concluded that there is (at least currently) no measuring technique available that can identify all necessary parameters in a boiling system. Therefore, any experimental investigation will have to make use of several techniques complementing each other to provide sufficient insight. For the current project, a combination of high-speed photography and optical probes for examination of the steam layer and PIV and holographic interferometry for the liquid phase were supposed to offer a reasonable combination. While high-speed photography and PIV have been largely discussed in literature (see Sec. 3.2.1) and well proven systems are commercially available, digital holographic interferometry and the optical probes required extensive further development. In the following sections, detailed information shall therefore be given on these techniques.

3.3 Holographic interferometry

Holographic techniques offer a number of advantages over other optical techniques, namely that from the recorded data, both phase and amplitude of the recorded lightwaves can be reconstructed. Furthermore, the technique offers a very high sensitivity on small changes in geometry, density etc. The physical and historical background of this technique shall be discussed in further detail in the following paragraphs.

3.3.1 Analogue holographic interferometry

Analogue Holographic Interferometry has been used as a technique for evaluation of density gradients in fluid flows by a large number of different researchers (see e.g. [93, 95, 102, 124]) over the last three decades. The technique is based on the interference of two coherent light beams, of which one is led through the studied volume where it is diffracted at density fields and objects. This beam is called the *object wave*. The other beam passes the

volume unaffected, and is referred to as the *reference wave*. The two beams create an interference pattern on a holographic plate, thus recording both amplitude and phase of the object wave. If the holographic plate is placed into a beam with the same wavelength as the recording one, the plate acts as a holographic grating, thus reconstructing the whole three dimensional object wave. To turn the setup from a standard holographic setup into a holographic interferometer, the developed holographic plate is replaced into the recording position. When the state of the regarded object changes, e.g. due to heating, the new object waves interfere with the ones recorded on the holographic plate, creating a new holographic interferogram that can be recorded behind the plate.

3.3.1.1 Real-time method

Of special interest with regard to time resolved measurements is the so called *real time method*, which has been used to provide high speed measurements of density distributions in applications such as boiling flows with high accuracy [95, 124]. For this method, a hologram of one state of the regarded system is recorded on a holographic plate, chemically developed and then placed in the optical path behind the object [102]. Like this, changes in the system create new object waves that interfere with the recorded waves on the plate, showing the changes in comparison to the recorded state. This is the actual holographic interferogram, which can then be recorded e.g. by high speed digital cameras. However, the real-time method still has some disadvantages: first, the use of at least one holographic plate requires chemical processing, which is time consuming and requires experience and equipment in analogue recording (darkroom etc.), which is no longer very common. The main disadvantage however results from the inability to create interferograms comparing to any other state than the one recorded on the reference hologram plate, which is usually the unheated or otherwise unchanged setup. Both of these disadvantages can be overcome by using a fully digital recording and processing system, as will be discussed in the following paragraphs.

3.3.2 Digital holographic interferometry

Digital holography for reconstruction of 3D-images has been used by a number of researchers [117], and also by some for digital holographic interferometry in flows [47, 48]. The digital hologram is recorded using a CCD or CMOS sensor, and is reconstructed numerically. Several methods for the numerical reconstruction of the object wave exist, as given e.g. in [90] and [130]. In the algorithm used for the results presented in this report, the reconstruction is done using the Fourier transform of the impulse response function H for one reconstructed plane given in Eq. (3.1), as described in [90] and [72].

$$H(m_\xi, m_\eta) = \exp \left\{ \frac{2\pi j d_r}{\lambda_L} \sqrt{1 - \frac{\lambda_L^2 \left(m_\xi + \frac{N_\xi^2 \Delta N_\xi^2}{2d_r \lambda_L} \right)^2}{N_\xi^2 \Delta N_\xi^2} - \frac{\lambda_L^2 \left(m_\eta + \frac{N_\eta^2 \Delta N_\eta^2}{2d_r \lambda_L} \right)^2}{N_\eta^2 \Delta N_\eta^2}} \right\} \quad (3.1)$$

m_ξ, m_η	pixelposition [-]	j	complex number $\exp(\dots)$
λ_L	light wave length [m]	N_ξ	number of pixel in ξ -direction [-]
ΔN_ξ	real pixel width in ξ -direction [m]	N_η	number of pixel in η -direction [-]
ΔN_η	real pixel width η -direction [m]	d_r	distance to reconstruction plane [m]

With the Fourier transform of the product of object and reference wave $G = FFT(a_{ccd} \cdot a_{ref})$, one plane a_{rec} of the analyzed volume can be reconstructed as a complex field with both phase and intensity information using the inverse Fourier transform of the product H and G : $a_{rec} = IFFT(G \cdot H)$. From a_{rec} , the phase ϕ and amplitude A_L for each pixel can be reconstructed using the complex number $z = A_L e^{i\phi} = Re(z) + Im(z)$ according to Eq. (3.2).

$$\phi = \arctan \left(\frac{Im(z)}{Re(z)} \right) \quad \text{and} \quad A_L = \sqrt{A_L e^{i\phi} \cdot A_L e^{-i\phi}} \quad (3.2)$$

The setup used for the experiments presented in this report is basically a classical holographic in-line setup with separated object and reference beams that records digital holograms. The actual holographic interferometry is then achieved by reconstructing the object waves for two different states of the setup, and letting these two waves interfere numerically by

subtracting the phases according to Eq. (3.3) [89, 118]. In contrast to the analogue method, the reference state can be chosen freely from all available holograms. Thus, the unheated case can be used as in the classical real-time method discussed above, as well as e.g. the state from the hologram taken one time step earlier.

$$\Delta\phi(\xi, \eta) = \begin{cases} \phi_1 - \phi_2 & \text{for } \phi_1 \geq \phi_2 \\ \phi_1 - \phi_2 + 2\pi & \text{for } \phi_1 < \phi_2 \end{cases} \quad (3.3)$$

From this, phase distribution and intensity for the digital holographic interferograms can be plotted. Thus, no chemical processing is required at all. For the interferometry, combinations of different reconstructed holograms can be chosen by the user. Like this, the main restrictions of the analogue technique are overcome.

4 Experimental setup and methods

The following chapter describes the setup of the test rig, the used materials and procedures as well as the applied measuring techniques.

4.1 Boiling test rig

The boiling test rig used for the experiments consists of a modular loop with a vertically orientated test chamber. A schematic flow diagram of the setup is given in Fig. 4.1, while Fig. 4.2 shows a CAD model of the whole test rig. The fluid is pumped through a preheater for adjusting of the

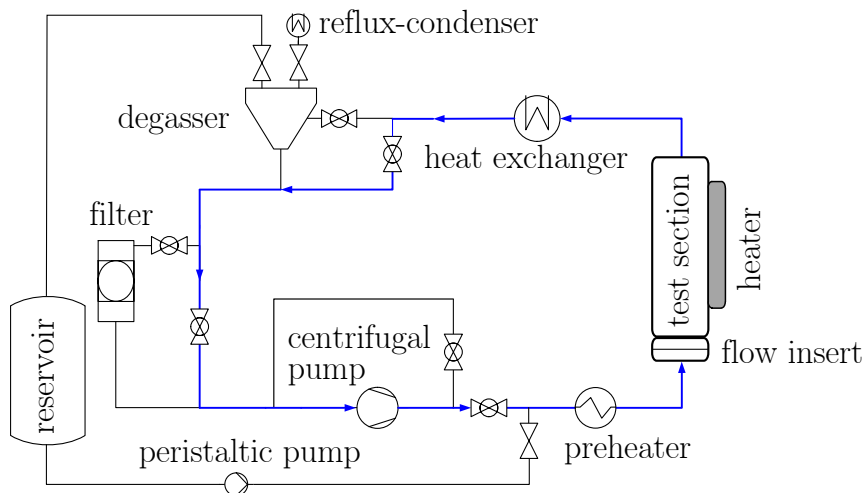


Figure 4.1: Schematic of the boiling test rig. The main fluid loop is marked in bold blue lines.

subcooling, then enters the main boiling chamber through a bend equipped with guide vanes to provide a homogeneous velocity profile at the inlet. Inserts for added turbulence and secondary flow structures can be placed at the inlet of the boiling chamber. After the boiling chamber, the fluid is cooled down with a double-pipe counter flow heat exchanger, and returned to the pump. A reflux condenser at the highest point keeps the setup open to the atmosphere, thus ensuring constant ambient pressure in the setup and separation of inert gases from the fluid. A filter and an additional

degassing unit and buffer tank are used to remove particles or inert gases from the fluid, and can also be run in bypass when necessary. The main part of the setup is mounted on a pneumatically insulated optical table to facilitate optical measurements, while the heavier and vibrating parts are mounted on the ground and are connected via flexible hoses. The pump is a multistage centrifugal pump type KSB Movichrom N-CN 15/6, which allows the running of experiments at superficial velocities of up to approx. 3 m/s. Using a bypass, the flow rate can also be set at very low levels. The maximum preheater power is 3 kW, allowing fast heating of the fluid. Both the double-pipe heat exchanger and the reflux condenser are cooled with process water, making it possible to keep the fluid temperature constant in steady state boiling at heat fluxes close to CHF for subcoolings up to 19 K. For higher fluid subcoolings, the fluid temperature can not be kept constant in steady state boiling over longer times, thus allowing only transient measurements.

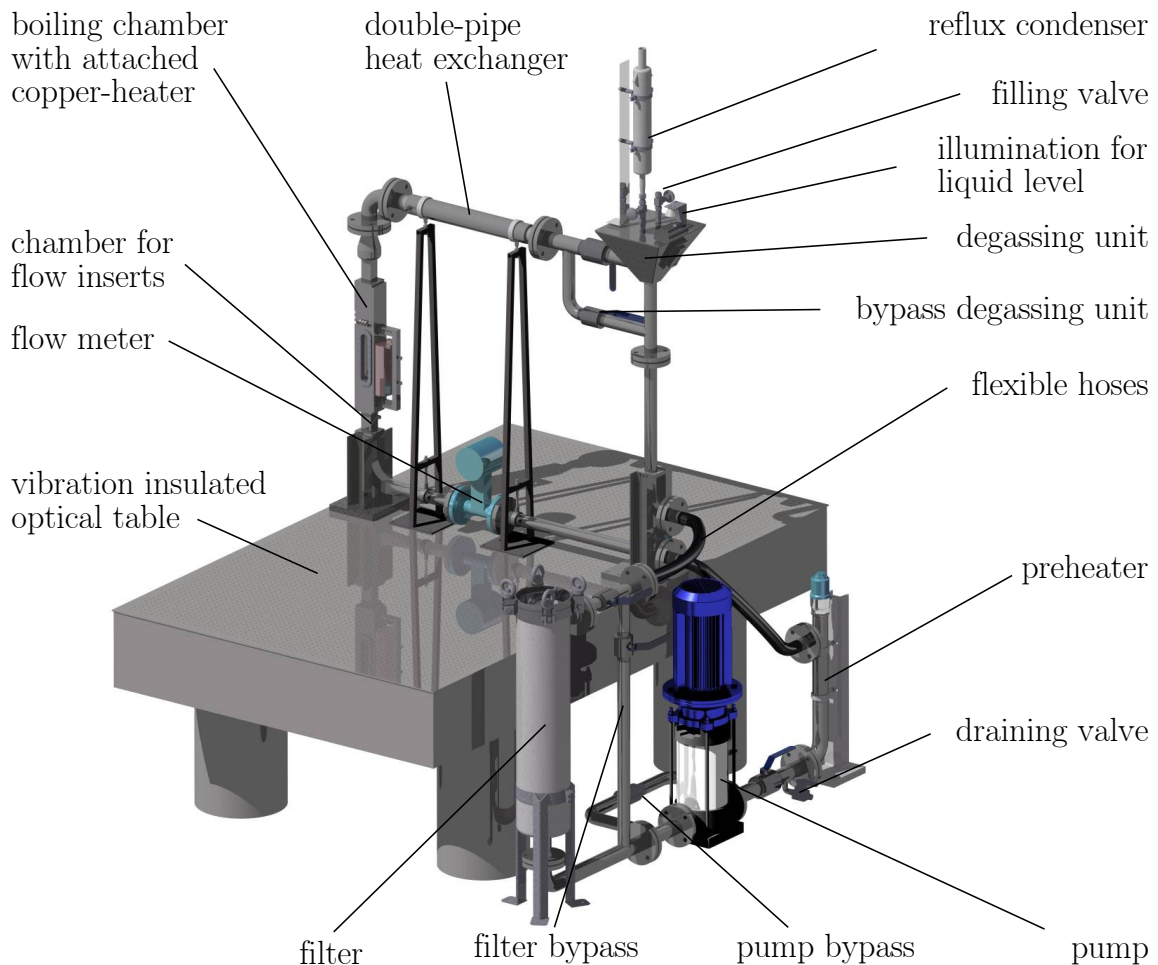


Figure 4.2: CAD model showing the main test rig.

4.1.1 Boiling chamber

The main boiling chamber is an improved version of the setup described by Maurus et al. [99–101] with a length of 500 mm and a square inner section of 40x40 mm². Heating is done via a 15x200 mm² copper bar flush mounted in one of the walls, beginning at 75 mm above the inlet. The copper heater is equipped with 12 cartridge heaters. Heating power is set via a continuously adjustable transformer, allowing total heating powers of up to approx. 3 kW. To measure surface temperature and heat flux, three rows with four thermocouples each are inserted at three different positions along the heater (for details, see Sec. 4.3.1). From the temperature gradients measured by the thermocouples, heat flux can be calculated using Fourier’s law, and surface temperature via a polynomial extrapolation. Fig. 4.3 shows a sectional view of the boiling chamber with the attached copper heater. To avoid errors due to possible changes of the heater surface from oxidation or fouling, reference measurements at given parameters were conducted after every third experiment. If necessary, the heater was then taken out of the channel and polished.

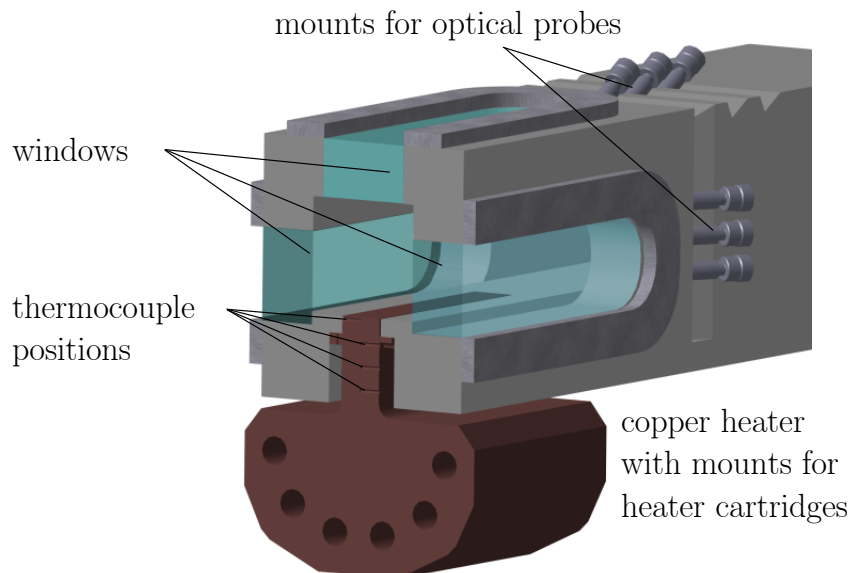


Figure 4.3: Sectional view of the boiling chamber and the attached copper heater.

4.1.2 Fluid

To be able to reach boiling regimes up to fully developed film boiling without damaging the heater, a working fluid with a low boiling temperature is required for the experiments. Aside from the low boiling point, the main requirements for the fluid are being a one component system, being liquid at standard conditions and being neither toxic nor flammable. Preliminary tests were conducted with a number of different fluids, of which dodekafluoromethylpentanone, available as 3M Novec649 showed the best performance. This fluid is chemically and physically similar to the well known 3M FC 72, with a boiling point of 49 °C at ambient pressure and enthalpy of vaporization of 88 kJ/kg. The main physical properties are given in Tab. 4.1 with a comparison to water.

Table 4.1: Physical parameters of dodekafluoro-2-methylpentan-3-one (3M Novec 649) and water at ca. 323 K.

Parameter	Novec 649	Water	Unit
density	1550	998	kg/m ³
dynamic viscosity	4.65	5.46	10 ⁻⁴ kg/m s
kinematic viscosity	0.3	0.5	10 ⁻⁶ m ² /s
specific heat	1103	4187	J/kg K
heat of vaporization	88	2300	kJ/kg
boiling point	49	100	°C

4.2 Flow inserts

As mentioned in Sec. 4.1.1, a bend with guide vanes is placed before the inlet to the boiling chamber to ensure a homogeneous flow profile. In preliminary experiments discussed by the author in [6], it could be shown that the flow field was indeed homogeneous at the inlet. PIV measurements from both horizontal directions at heights of 0, 200 and 400 mm above the inlet confirmed the positive effects of the applied guide vanes, showing a steady velocity distribution over the channel cross-section for all heights. Turbulence intensity was measured at a value of approx. 0.04 near the inlet, which confirmed values expected from literature for the given Reynolds numbers

[108]. PIV Measurements in vertical orientation also confirmed that no vortices were present in the empty channel configuration along the whole channel length [6]. Furthermore, the modular setup of the test rig allowed to place and exchange flow inserts at the inlet to the test chamber with low time requirement. Different types of inserts were designed with the aim of inducing either near isotropic turbulence or different kinds of longitudinal vortices in the channel. All inserts were analyzed using PIV in cold flows and boiling experiments. A wide array of different inserts was analyzed in preliminary experiments which are not discussed here for sake of brevity, but have been discussed by the author in several publications, see e.g. [6] for perforated plates of different types, and [12] for a comparison of twisted tape and delta wing inserts. Inserts using wire grids and multiple twisted vanes produced too little influence on the flow to have a measurable impact on the boiling processes, and were therefore omitted as well. As a result of the preliminary experiments, two types of inserts were chosen for the main part of the experimental program. These were one perforated plate with the aim of creating near isotropic turbulence at high turbulence intensities at the inlet to the boiling chamber, and a twisted tape insert aimed at creating a single, stable longitudinal vortex spanning the entire heated area. Fig. 4.4 shows CAD-renderings of the two inserts.

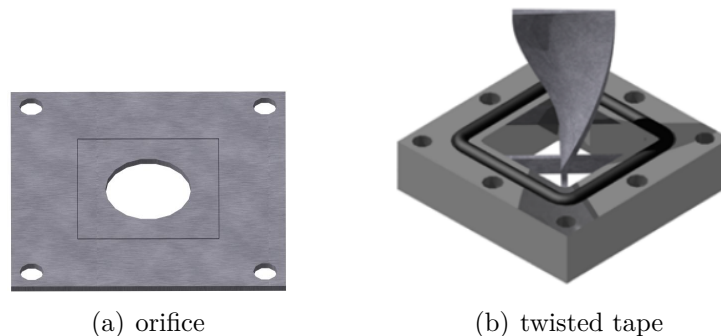


Figure 4.4: CAD rendering of the used flow inserts. The black rectangle marks the channel cross section for the orifice.

4.2.1 Orifice insert

The orifice insert consists of a stainless steel plates with a thickness of 2 mm, with a centric hole of 25 mm diameter, resulting in a porosity of 0.3. The

turbulence intensity measured by PIV in cold flow showed a maximum value of approx 0.7 at a height of 100 mm above the inlet [6, 12], which decayed exponentially in the downstream direction.

4.2.2 Twisted tape insert

A twisted tape insert with one large vane is used as the main vortex-inducing insert for the experiments. The insert consists of a stainless steel vane with a thickness of 1.5 mm, a width of 35 mm and a total length of 50 mm. The vane is twisted by an angle of 90° . Fig. 4.5 shows a visualization of the initial vortex created by the twisted tape insert from PIV measurements, and shows the vorticities measured by PIV at different heights above the inlet. The vortex created by the twisted tape decayed rather slowly along

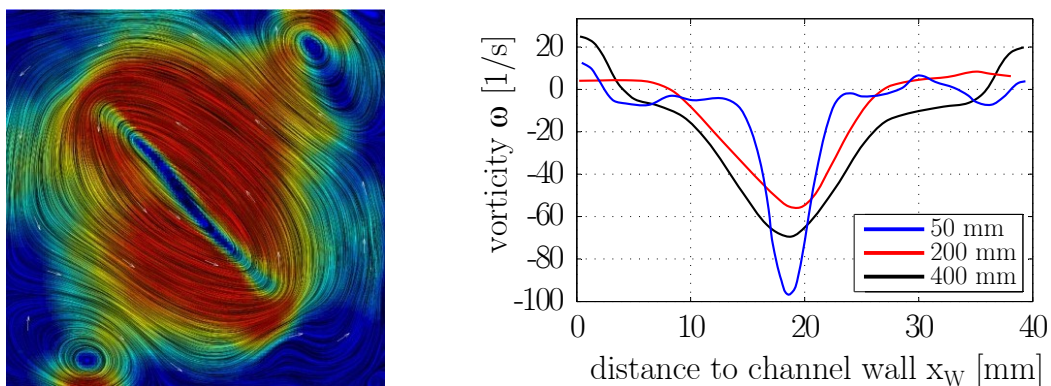


Figure 4.5: Vortices created by the twisted tape insert, left: Visualization of the vortex created by the twisted tape over the channel cross section. The stream lines were generated from PIV data using a line integral convolution algorithm. Right: Vorticities measured from PIV for the twisted tape at different heights above the inlet.

the channel: at the inlet, the maximum horizontal velocities were ca. 30% of the superficial velocity, but were still at the same values at a height of 200 mm. At a height of 400 mm, the vortices were still clearly distinguishable and still showed velocities of ca. 20% of the superficial velocity. Fig. 4.6 shows the resulting vector fields for the twisted tape at the different heights. This trend was also confirmed by the calculated vorticities for the twisted tape as shown in Fig. 4.5.

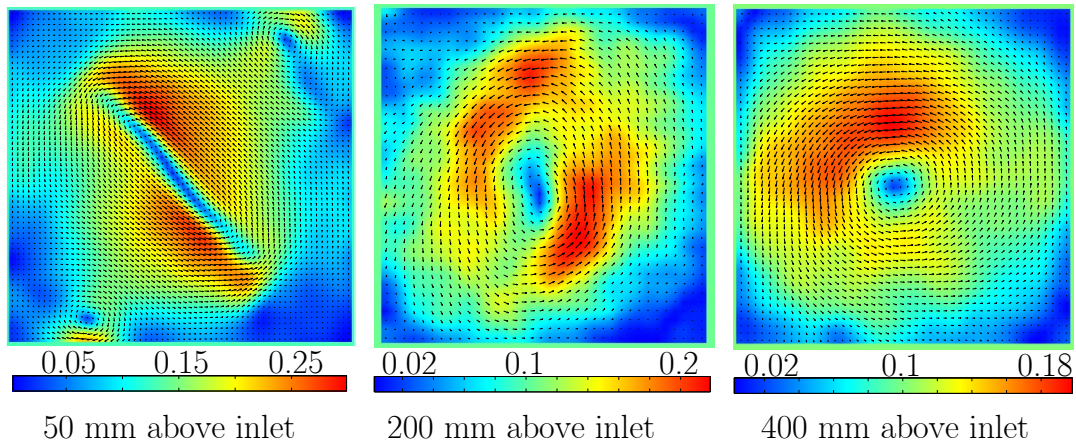


Figure 4.6: Time averaged velocity fields over the channel cross section for the twisted tape insert at heights of 50, 200 and 400 mm above the inlet (left to right), the colormap shows the velocity magnitude in m/s.

4.3 Measuring techniques: setup and methods

The following section describes the setup of the applied measuring techniques, as well as the methods used in running the experiments and in the operation of the measuring techniques and the processing of the results.

4.3.1 Thermocouples

As mentioned in Sec. 4.1.1, thermocouples inserted in the heater are used to measure heat fluxes and surface temperature. The thermocouples are mounted in three rows of four type K thermocouples each. The rows are positioned at 50, 100 and 150 mm from the leading edge of the heater (see Fig. 4.3). For each row, the thermocouples are mounted at 1, 9, 17 and 25 mm beneath the heater surface in the middle axis of the heat transferring area. The diameter of the thermocouples is 0.5 mm for the ones mounted closest to the heater surface and 1 mm for the others. From these, the heat flux is calculated for each row using the temperature gradient between the two thermocouples closest to the heater surface according to Fourier's law assuming one dimensional heat transfer. The surface temperature is calculated using a polynomial extrapolation over each row of thermocouples.

4.3.2 High-speed photography

High-speed photography is used to analyze the distribution of the vapor phase, the numbers and sizes of isolated vapor bubbles and larger agglomerations, and for the determination of the velocity of the vapor phase.

4.3.2.1 Set-up

The photographic setup is a classical backlit setup, with two 500 W floodlights mounted behind a diffusing screen as shown in Fig. 4.7. The camera

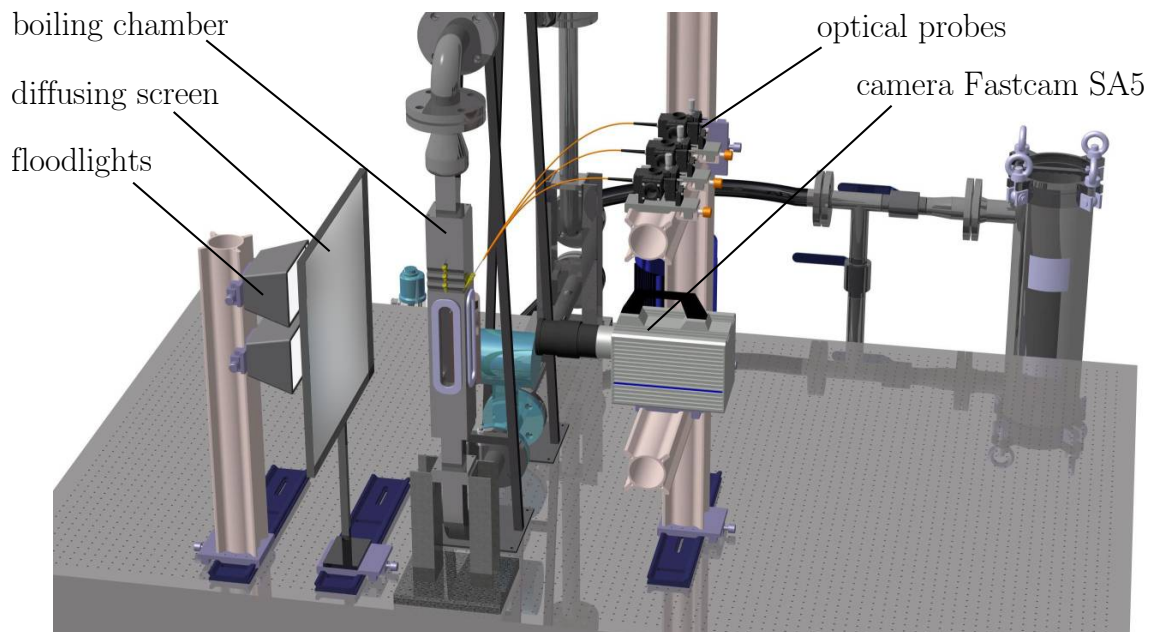


Figure 4.7: Setup for high-speed photography together with the optical probes.

used is a Photron Fastcam SA 5 with a Tamron SPAF 24-135mm lens. The camera specifications are given in Tab. 4.2. For most of the experiments, the frame rate is set at 2000 fps and the shutter time is $1/8000$ s. The interrogated area is 40 by 20 mm with a resolution of 1024x640. At this resolution, 17469 images can be recorded for each experiment, giving recording times of 8.73 s.

4.3.2.2 Processing steps used for photographic analysis

After acquisition, the images are processed using different algorithms implemented in Matlab for a fully automated analysis. For all processes, the

Table 4.2: Camera specifications

Type	Photron Fastcam SA5
Resolution	1024x1024 pixel
Pixel size	20 μm
Sensor size	20.5x20.5 mm^2
max. framerate (at full resolution)	7000 fps
min. shutter time	10^{-3} ms
number of frames (at full resolution)	10 000

images are first binarized as shown in Fig. 4.8 (a) and (b). From the binary image, a mean intensity for each pixel line perpendicular to the heater surface (vertical direction in Fig. 4.8) is calculated as shown in Fig. 4.8 (c). The resulting intensity plot can be used to provide statistical information on the void fraction and the distribution of the vapor phase. For

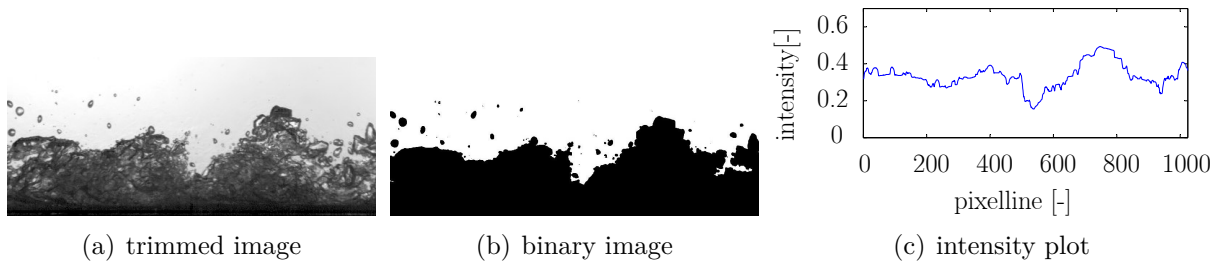


Figure 4.8: Numerical processing steps for the images taken from high-speed photography.

further processing, different methods are used as described in the following paragraph.

4.3.2.3 Void fraction

For calculation of the void fraction for each picture, the mean intensity is used. This provides the overall percentage of bubbles in the whole recorded field, and is thus depth integrated.

4.3.2.4 Bubble size distribution

Near CHF, the vapor was observed to be concentrated mainly near the heater surface, consisting mostly of larger coalesced structures (see Fig. 4.8).

However, a number of bubbles were also observed to move freely in the channel. For these, a size distribution could be calculated by removing the layer near the surface using a border clearing algorithm and subsequently filling and measuring the remaining single bubbles with adequate algorithms. Using a calibration target, the resulting pixel sizes can be transformed to mm^2 .

4.3.2.5 Vapor agglomerations

At high heat fluxes, larger agglomerations of vapor are observed in the channel. To analyze these, algorithms for the detection of the size, velocity and frequency of the agglomerations are used. Firstly, all single bubbles in the channel are removed from the binarized images using a filtering algorithm, so that only the coalesced layer near the wall remain in the images. From this, a matrix (C) is calculated giving the distance the vapor layer penetrated into the channel for each line of the images. By averaging this parameter over all images, the mean height (dimension perpendicular to the wall) of the agglomerations is calculated. By binarizing the matrix C with the mean height as threshold, the matrix is divided into areas with agglomerations (value 1) and no agglomerations (value 0). By counting the continuous areas of value 1, the mean number $S(k)$ of agglomeration per picture k is calculated. Furthermore, the ratio of agglomerations present in each picture $D(k)$ is calculated as the mean of the binarized matrix C. The mean length $L(k)$ (dimension parallel to the wall) for each picture is then calculated by dividing the ratio $D(k)$ with the number of agglomerations and multiplying with the image height in pixel:

$$L(k) = \frac{D(k)}{S(k)} \cdot 1024 \quad (4.1)$$

Using the same calibration as for the bubble sizes, the dimensions in mm are calculated. The parameters are always calculated for all images of each recording, i.e. approx. 17.000 images, giving well averaged statistical data.

4.3.2.6 Frequencies

For detection of the frequencies at which the agglomerations appear, two different algorithms are used. First, a FFT analysis is performed on the

signals, with the maximum of the FFT showing the main frequency. As a second and more robust method, a peak detection algorithm is used on the signals to detect the time distance between two agglomerations.

4.3.2.7 Velocity

To detect the average velocity of the vapor phase in steady state boiling, a cross-correlation algorithm is applied [1]. The resulting velocities are averaged over all images for one recording, and averaged for each pixel row of the sensor.

4.3.3 Optical probes

While the photographic measurements give valuable information about the general structure and motion of the vapor phase, it has significant shortcomings in areas of high vapor concentration due to its depth integrative nature. This is especially true for the area close to the heater surface, where the method becomes practically blind at higher heat fluxes due to the high number of bubbles present. However, this area is naturally of special interest with regard to the boiling processes taking place close to CHF. To overcome this challenge, optical micro-probes were developed in the course of the project to provide minimally invasive point measurements of the vapor distribution for distances of down to 0.1 mm from the heater surface. The setup, fabrication and preliminary evaluation of the probes have been described in detail by the author in [14], and are therefore only shortly discussed here.

4.3.3.1 Background

Fiber optical probes are used for measuring a variety of physical parameters, including temperature, strain and vibration. Fiber sensors are becoming more and more common due to their advantages like high physical robustness and insensitivity to electrical fields and high spatial and temporal resolution. For point measurements of void distribution in multiphase flows, fiber optical probes have been used by a number of authors over the last 40 years. An overview on the subject is given by Spindler and Hahne

in [93] and Cartellier and Achard in [25] and Delhaye in [79]. Detailed reviews of the technique were also given by Cartellier [27], Vejražka et al. [128], Cartellier and Barrau [26], Mena et al. [103], Hong et al. [71], and Juliá et al. [77]. Different types of probes have been proposed, of which the most common are the so called U-shaped fiber probe which consists mainly of a bent fiber with an emitter at one and a sensor at the other end and the monofiber probe where the light travels bidirectional in the fiber. Both types of probes detect different phases (gas/liquid) via the change in refractive index at the fiber tip and resulting changes in reflection of the beams according to Snellius' law [93]. With liquid present at the tip, the beam coming from the light source is emitted into the liquid, while with gas present total reflection occurs at the tip and light is reflected in the direction of the sensor. Using this effect, highly reliable time resolved point measurements of the void fraction can be achieved with minimum intrusiveness.

4.3.3.2 Working principle

While the U-shaped fiber can be used with a less complex optical setup, the monofiber probe can have a smaller and more robust probe tip. As the setup of the tip was of high importance for the boiling experiments, the monofiber setup was chosen. For all types of probes, the shape of the

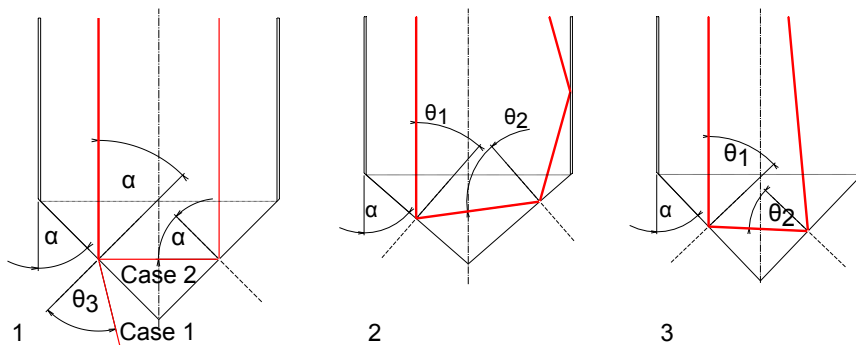


Figure 4.9: (1) Tip-angle of 45 degrees, showing case 1 for transmission of light due to liquid and case 2 for total reflection due to gas at probe-tip; (2) maximum tip-angle (3) minimum tip-angle.

tips is of high importance. For the monofiber probe, the best tip-geometry in two-phase-flows is usually regarded to be a conical shape at a half cone angle between 43 and 51 degrees [25]. For a simplified assumption of beams

propagating parallel to the fiber axis, the three theoretical cases for the tip angles where the beam is reflected at both probe interfaces are shown in Fig. 4.9. In reality, the criteria for reflection at the tip are more complex due to beams propagating at different angles in multimode fibers, so that changes in refractive index can also be measured with tips of smaller and larger angles. A more detailed discussion is given by Cartellier and Achard in [25]. For the probes discussed here, a tip half-cone angle of 45° was chosen.

4.3.3.3 Separation of beams

For monofiber probes, there are two general setups used for separating the sending and transmitting beam proposed in literature. Firstly, the use of a beam splitter inserted between the fiber and the light source and secondly the use of a fiber coupler. For the probes presented here, the beam splitter setup was chosen because of the greater flexibility when using fibers with different diameters, the better access to the single beams and the lower costs for fibers of diameters above $100\ \mu\text{m}$. This setup is shown schematically in Fig. 4.10.

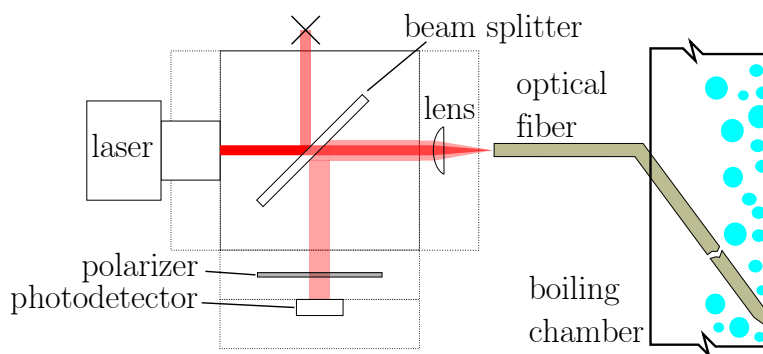


Figure 4.10: Schematic drawing of the beam setup for the optical probes.

4.3.3.4 Setup of the optical needle probe

The probe setup used in this report consist of silica multimode fibers with a core diameter of $200\ \mu\text{m}$ (Ratioplast-Optoelectronics HCS $200/230\ \mu\text{m}$) with a numerical aperture (NA) of 0.37. The fiber tips are polished conically to an angle of 45 degrees using a diamond lapping film and a polishing setup

specially designed for this purpose as described in [14]. A microscope image of the fiber tips is given in 4.11 The fibers are illuminated with a diode-laser

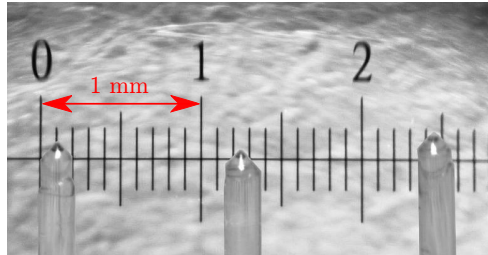


Figure 4.11: Microscope image of 3 tips of the optical probes with 200 micron fibers. The scale is in millimeters.

(Global Laser 1250 CW Cameo) with a wavelength of 650 nm and an output power of 1 mW. The beams are collimated into and out of the fiber via a plano-convex lens with a focal length of 5 mm. The sending and the reflected beam are separated via a beam splitter with a transmission/reflection ratio of 50:50. The intensity of the reflected beam is measured with a silicon photodiode (Siemens BPX 61) with a switching time of 20 ns attached to a signal amplifier and a data acquisition system. Parasitic reflections at the lens and at the end of the fiber are reduced using a polarizing filter positioned in front of the photodiode. The optical setup is realized using the Qioptiq/Linos Microbench system as shown in Fig. 4.12. To ensure mechanical stability, the fibers are housed in stainless steel tubes with an outer diameter of 1.4 mm. The probes are mounted axially moveable into the test channel using 1/16 in vacuum fittings with o-ring seals (Swagelok SS-1-UT-A-4) as shown in Fig. 4.13. The probes are mounted at a fixed angle of 30 degrees to the channel wall. With the used fittings, this makes it possible to position the probes at varying height and distance combinations to the heater surface.

4.3.3.5 Signal processing

The installed photodiodes allow for maximum recording frequencies of up to 1 MHz. Preliminary experiments had shown frequencies of 1 kHz to be sufficient for all experiments in the boiling chamber. As the amount of data created by the probes is relatively small, a data acquisition frequency of 3 kHz was chosen for the boiling experiments, thus allowing for more detailed

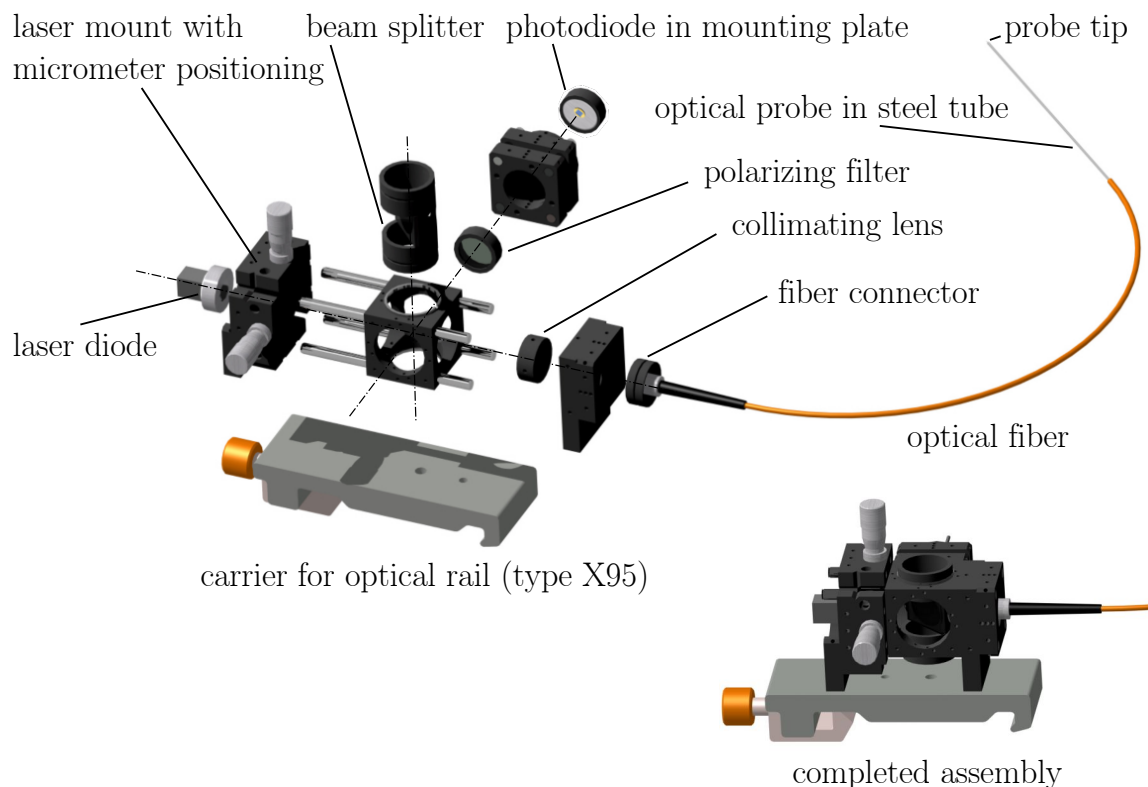


Figure 4.12: CAD rendering showing an exploded view and fully assembled setup of the main optical components for the probes.

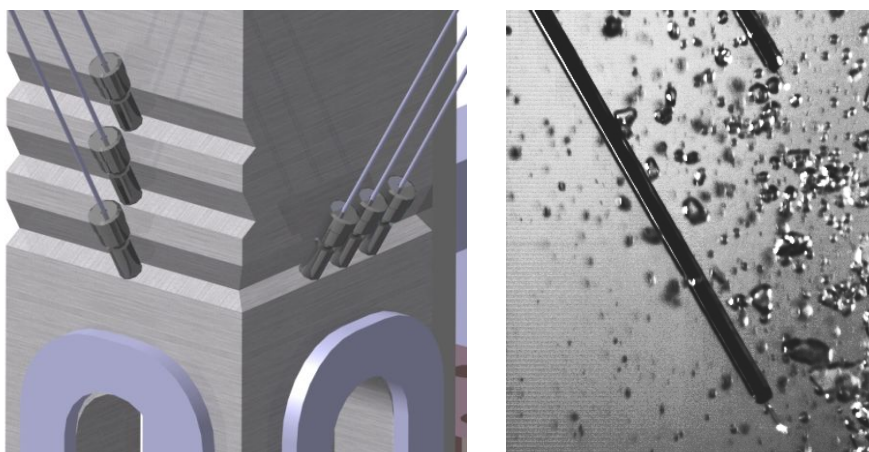


Figure 4.13: Mounting of the probes in the channel used for boiling experiments: (left) CAD-drawing of channel with axially moveable mounted probes, (right) photograph of 2 probes in boiling flow.

data evaluation where necessary. Like this, recording times of several hours were technically possible, allowing a recording of the complete boiling cycle for each experiment. The signals received from the photodiode are amplified

to a range of 0-10 V. With the used setup, only little background noise was observed. Fig. 4.14 shows the received signal for two bubbles of different sizes in a boiling flow. The left part of Fig. 4.14 shows the raw voltage signal, and the right part shows the binarized signal used for further processing below. The signals are binarized using a phase indicator function (PIF) as described by [22] (see Eq. (4.2)).

$$PIF(\vec{x}, t) = \begin{cases} 1 & \text{for } U \geq U_t & \text{(vapor)} \\ 0 & \text{for } U < U_t & \text{(liquid)} \end{cases} \quad (4.2)$$

PIF Phase indicator function [-]
 U analogue voltage signal [V]
 U_t threshold voltage [V]

The threshold voltage U_t was defined as 2 Volts above the highest fluctuations of the basic noise measured for the probe in single phase liquid. Thus, a safe determination of vapor could be achieved.

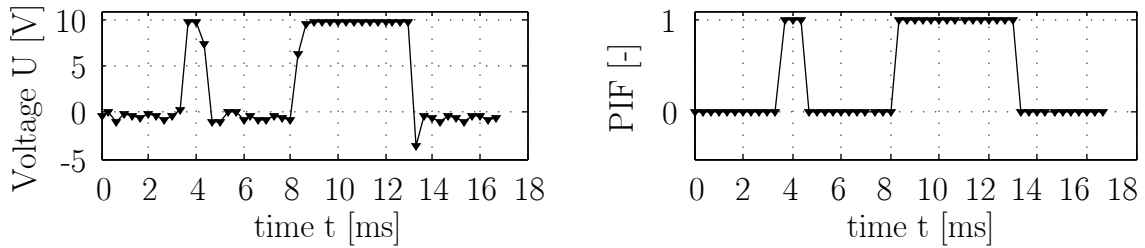


Figure 4.14: Signal treatment for the optical probes: Analogue voltage signal and binarized signal (phase indicator function, PIF) for two detected bubbles of different sizes.

4.3.3.6 Gas holdup

The gas holdup $\epsilon(t)$ for a given time is calculated from the binarized signals using a simple moving average function as given in Eq. (4.3). For the measurements discussed here, the moving average was calculated over one second, i.e. $n=3000$ values.

$$\epsilon(t) = \frac{1}{n} \cdot \sum_{i=1}^n PIF(t - n + i) \quad (4.3)$$

4.3.3.7 Bubble size distribution

Using the phase indicator function, single bubbles or other continuous vapor structures are detected as a constant series of non-zero values. The duration of the signals, denoted as the contact time t_c , is directly proportional to the size of the bubbles. An algorithm is used to create a matrix of the detected signal lengths, allowing to compare the relative changes in the vapor structure sizes for different regimes and during the CHF transient. As the velocity of the vapor phase can not be measured with the probes, only an approximation of the actual bubble size is possible using the fluid superficial velocity v_s , as given in Eq. (4.4).

$$d_b = t_c \cdot v_s \quad (4.4)$$

4.3.3.8 Detection of vapor agglomerations

In fully developed nucleate boiling, larger agglomerations of vapor with some liquid dispersed inside are observed. To detect these with the probes, a pattern matching algorithm is used. The algorithm uses two criteria: firstly, the vapor fraction from the moving average is required to be above a certain threshold value ϵ_a which was set at approx. 1.5 times the average void fraction for the given thermohydraulic parameters (subcooling and flow rate). Furthermore, the length of the area with higher void fraction is required to be above a certain critical time duration t_a which was set at approx. 4 ms. Using this, a matrix of agglomeration appearances over time is created from which the time between two agglomerations and thus the frequency can be deduced. For this, both a FFT analysis and simple arithmetic averaging of the time distances are used.

4.3.4 Particle image velocimetry (PIV)

Using high-speed photography and optical probes, extensive knowledge about the distribution, shape and motion of the vapor phase can be gained. However, hardly any information about the behavior of the liquid layer can be obtained with these techniques. Therefore, experiments using particle image velocimetry (PIV) were conducted to gain enhanced insight into the motion of the liquid phase both for single phase and in boiling experiments.

PIV is a non invasive measuring technique based on tracking the motion of artificial tracer particles moving with the fluid [112]. The particles are usually illuminated using a thin, nearly two dimensional laser sheet. For the experiments discussed in this thesis, two different PIV setups were used which shall be discussed in the following paragraphs. As tracer particles, silver coated hollow glass spheres (S-HGS) with a mean diameter of $20\ \mu\text{m}$ were used for all the experiments. The particle density of $1400\ \text{kg}/\text{m}^3$ was close enough to the fluid density to make errors due to slip and buoyancy negligible.

4.3.4.1 Time averaged PIV for single-phase flow analysis

As flow analysis using optical techniques techniques poses a number of challenges when applied in two phase flows, the flow structure was first analyzed for single phase, unheated flows. To give better optical access, the test chamber was replaced with a transparent channel of identical inner dimensions. The camera can be mounted in three positions, two of which are given in Fig. 4.15. The first two positions have the camera mounted horizontally, with the camera mounted on the same height as the test chamber and viewing either directly on the heater surface or parallel to it. The third position is used to analyze secondary flows created by the inserts. For this, the camera is mounted atop the test chamber, viewing vertically downward through an immersion pipe as shown in Fig. 4.15. Measurements were conducted at heights of 0, 200, and 400 mm above the inlet for all inserted geometries except for the twisted tape insert where the lowest measurement was at 50 mm due to the length of the insert. The measurements were conducted at superficial velocities of 0.3, 0.6 and 1.2 m/s. The time delay between two double pictures was 100-800 μs , depending on the flow rate and the camera position. The pictures were processed using the programs Dantec Flowmanager, Matlab, and the Matlab based PIV toolbox PIVlab [1]. Using these, velocity vector fields, turbulence intensity and vorticity were obtained.

4.3.4.2 High-speed PIV for boiling flows

To study the flow during boiling, high-speed PIV has to be applied due to the fast and unsteady motion of the vapor. The PIV setup used here consists

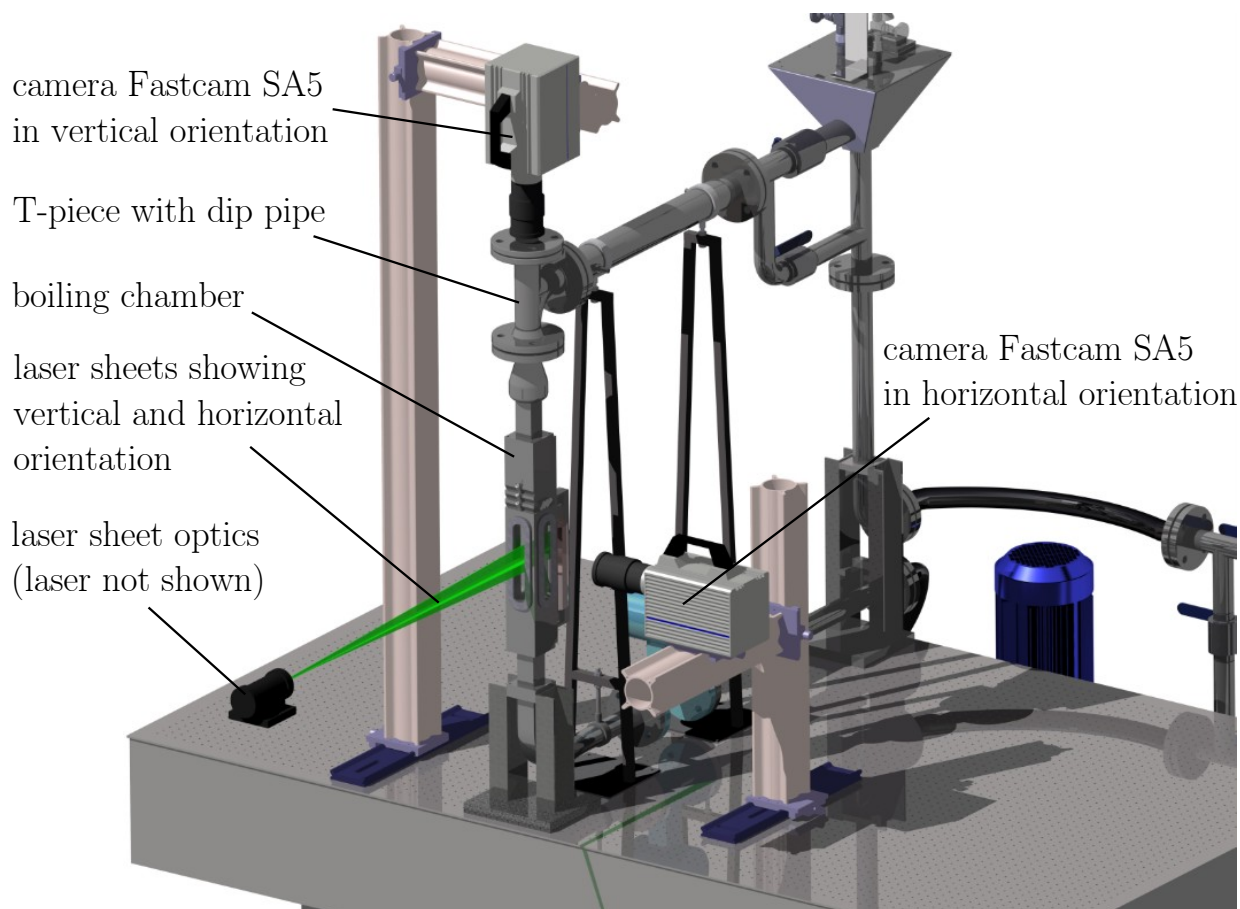


Figure 4.15: PIV setup showing two possible orientations for the cameras and laser sheets.

of a 527 nm high-speed dual cavity Nd:YLF Laser (Type New Wave Pegasus) with a maximum repetition rate of 20 kHz and a pulse energy of 10 mJ at 1 kHz (both heads). For the experiments discussed here, the repetition rate is 7 kHz. The same Photron Fastcam SA5 camera as discussed in Sec. 4.3.2 for the high-speed photography is used for the high-speed PIV. The lens used for the PIV experiments is a Nikon Nikkor 200 mm f/4.0, giving an interrogation area of $25 \times 25 \text{ mm}^2$. The camera is run at 7 kHz, with shutter times of $1/14000 \text{ s}$. Positioning of the laser and camera is done in the horizontal orientation as shown in Fig. 4.15, allowing to view the motion parallel to the main flow and heater orientation. The laser sheet is positioned at a distance of 1 mm to the heater edge to avoid disturbances from bubbles moving in front of the laser sheet. The camera is positioned at a height of 620 mm above the table, so the interrogated area is exactly in the middle of the heated section.

4.3.5 Digital holographic interferometry, holographic interferometric velocimetry

With the techniques discussed above, information can be gathered on the structure and motion of the vapor phase (high-speed photography), velocity fields in the liquid phase (PIV), vapor distribution within the vapor layer (optical probes) as well as temperatures in the heater (thermocouple arrays). However, no information is available on the temperature distributions within the liquid, apart from the mean subcooling measured by thermocouples. To gain insight into these effects, an optical setup for the application of digital holographic interferometry (DHI) was constructed and evaluated [5, 11, 15]. Preliminary experiments based on the algorithms presented by Ilchenko [72] showed the applicability of digital holography for depth reconstruction of bubble positions in adiabatic two phase flows [5]. For these preliminary experiments, an in-line setup with both object and reference beam passing through the test chamber was used due to the less complex setup. However, in boiling flows, the light passing through the test chamber is deformed due to density fields to such an extent that a flat reference wave is no longer achievable. This challenge could only be overcome by expanding the setup to an in line setup with separated object and reference beams, with the reference beam passing behind the boiling chamber. Using this setup, the aforementioned digital holography could be expanded to a fully digital holographic interferometry setup, making it possible to visualize density gradients in the flow. Furthermore, the high sensitivity of the setup allowed a coupling of the technique with a cross-correlation algorithm to create a new velocimetric technique that yielded results similar to PIV and could be used to confirm the PIV results [15]. The next paragraphs shall give an overview on the background of the holographic technique and present the applied optical setup.

4.3.5.1 Setup of the digital holographic interferometer

The setup applied is shown schematically in Fig. 4.16. A Siemens He-Ne laser with a wavelength of 633 nm and an output power of 40 mW is used for illumination. The laser beam is separated using a variable beam splitter and then enlarged via two beam expanders with a 20 μm spatial filter. The object beam is led directly through the boiling test chamber, while the reference

beam passes behind it. This separation of the object and reference beam is necessary to keep a plane reference wave. As the possible angle of incidence for the two beams is limited by the spatial resolution of the CCD-sensor, the two beams are combined using a 50:50 beam splitter plate in front of the camera, so that the angle of incidence is the same for both beams. The camera used for the experiments is the same Photron Fastcam SA5 as discussed in Sec. 4.3.2 for the high-speed photography, which is used without lens for the holographic recordings. The camera specifications are given in Tab. 4.2. For most of the experiments discussed here, the camera was run at acquisition rates of 7.000 fps with shutter times of $1/14.000$ s (≈ 71 μ s).

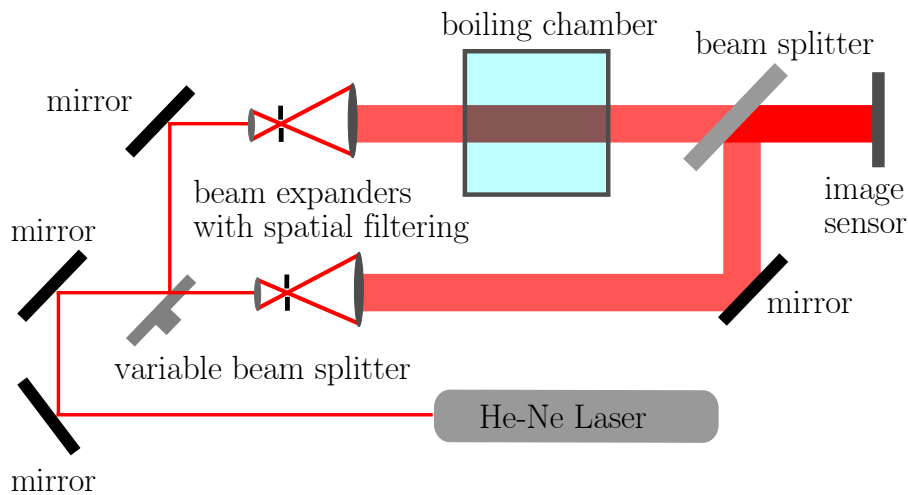


Figure 4.16: Schematic setup of the digital holographic interferometer.

As no lens is used on the camera, the recorded area is the same as the size of the camera sensor, i.e. 20.5×20.5 mm². To avoid disturbing wave fronts from solid objects, the holograms are taken at a distance of 3 mm parallel to the heater surface (see Fig. 4.18). The holograms are recorded at the middle of the heated section, i.e. 200 mm above the inlet. Fig. 4.18 shows a resulting hologram for a boiling process in comparison to a photographic image of the same regime. The heater surface is on the right hand side of the pictures. In the hologram, the phase boundary can be clearly seen as marked by the dashed line in Fig. 4.18. Far more detail can be derived from the calculated interference phase plots as shown in Fig. 4.19 (a) for the same hologram. The resulting structures represent the changes in phase from the reference to the active hologram. On the right hand side of the boundary, the object wave is blocked due to high vapor concentrations, so that only

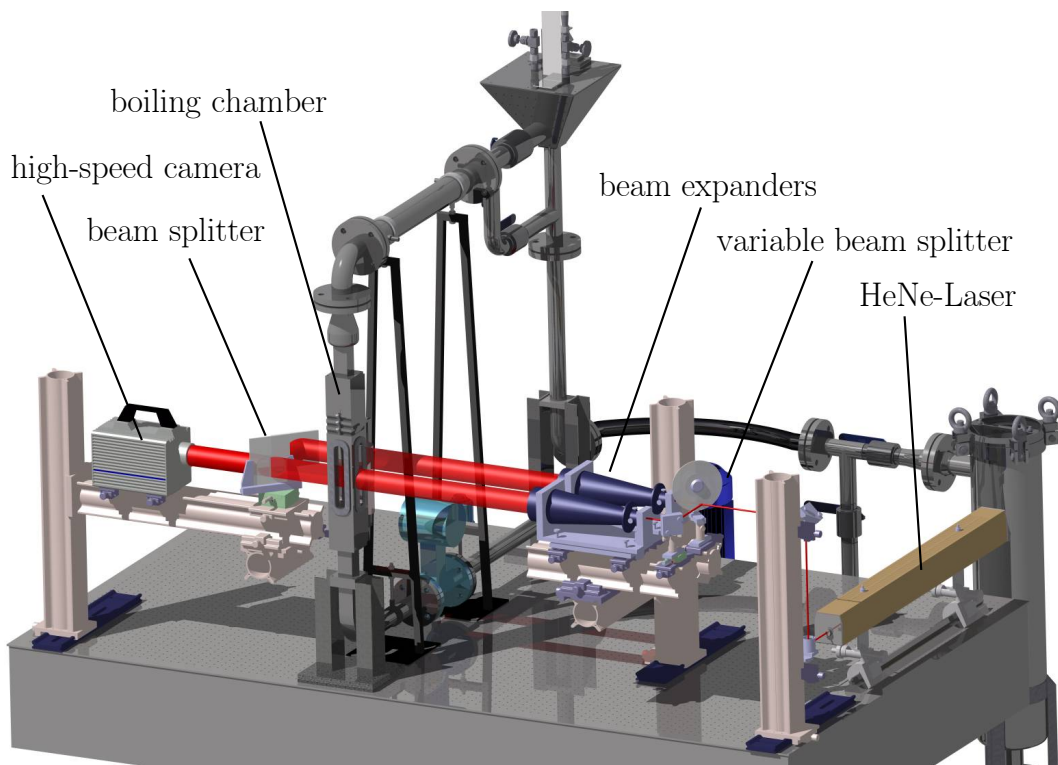


Figure 4.17: CAD model showing the implementation of the digital holographic interferometer at the boiling test-rig.

the reference wave is recorded and no further information can be deduced. On the left hand side, subcooled liquid can be observed with slight thermal disturbances, notable as darker blots. These will be discussed in more detail in the following paragraphs.

4.3.5.2 Image to Image sequential interferometric technique (I2I)

Using the presented setup, it is possible to create sequential interferograms from high speed holographic recordings that show the changes in the density fields between two subsequent pictures. For this, the phase information of the directly preceding reconstructed frame is added to the current frame (see Eq. (3.3)) instead of that of the cold reference hologram. This technique will be further denoted as Image2Image (I2I) interferometry. It can offer a number of advantages in comparison to the classical method. For example, the slight changes in temperature from one frame to the next are often lost when using a cold reference hologram, and can be visualized more clearly when applying the I2I technique. This is especially true for moving density

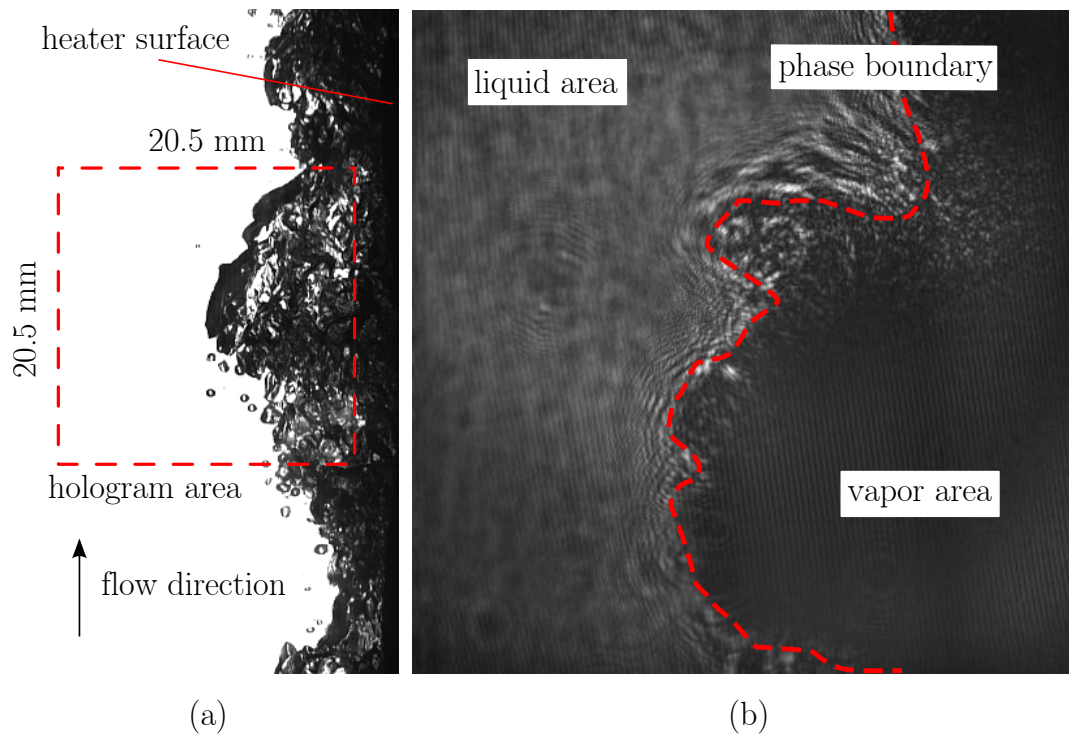


Figure 4.18: Interrogation area and sample results for DHI: (a) Photographic image of the boiling process with interrogation area for holographic recording, marked in red, and recorded hologram of the boiling process at same thermohydraulic parameters (b).

fields, as prevalent through the turbulent eddies in many flows. Here, the I2I technique can provide a significant increase in sensitivity. Also, disturbances in the optical path such as dust on the heating chambers windows, optical impurities and other contaminants could sometimes not be removed completely from the pictures using the cold reference because of slight changes in the setup during the heating process. Using the sequential method, these disturbances are removed completely. Furthermore, due to the size of the apparatus it proved difficult to create reference pictures for the setup with actually no density gradients present at all. Disturbances from waves of slightly warmer liquid were often observed for the cold reference holograms, which in turn lead to distortions in the holographic interferograms. By using the directly preceding hologram as reference, these errors can be removed as well. As a result, the I2I technique provides clearer holographic interferograms with a higher sensitivity for changes in the density fields. It has to be noted however, that the technique naturally only shows the changes from one hologram to another. In contrast to using a cold reference hologram,

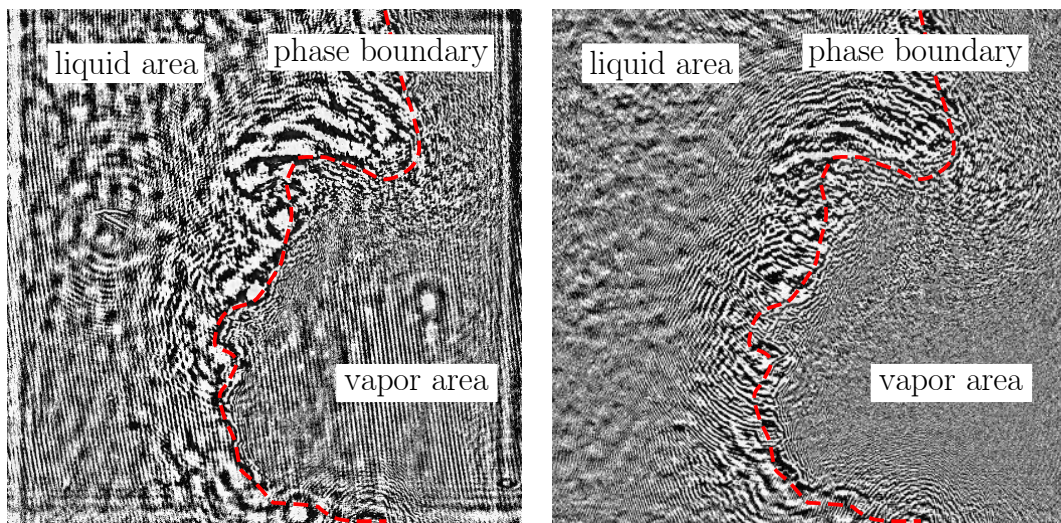


Figure 4.19: Different reconstruction techniques for DHI: (a) interference phase plot using a reference hologram of the cold channel, (b) interference phase plot using the directly preceding hologram as reference ($\Delta t=0.14$ ms).

areas without any density change will be subtracted from the interferogram. Therefore, very slow processes can be lost. For the experiments discussed here, both methods were used and evaluated, with the I2I technique giving the better results in the majority of cases. All interferograms shown within this thesis are therefore I2I interferograms, unless noted otherwise. Fig. 4.18 shows the raw hologram for a boiling process. Fig. 4.19 (a) shows the resulting interference phase plot using a hologram of the cold setup as reference, while Fig. 4.19 (b) shows the I2I interferogram, resulting from using the hologram taken $1/7000$ s (0.14 ms) earlier as reference. With increasing time distance Δt between the holograms, the structures in the I2I interferograms become more coarse as shown in Fig. 4.20. This can be used to better enhance gradients in density over longer time scales. However, at longer time distances possible errors due to contaminations can not be eliminated as easily. For the measurements discussed here, the smallest possible time distance for the given camera resolution and exposure time was chosen. Except for CHF transition, this was $1/7000$ s (0.14 ms) for all experiments. For CHF transition, a longer recording time was required, resulting in a recording frequency of 500 fps, giving a time distance of $1/500$ s (2 ms) for the I2I interferograms.

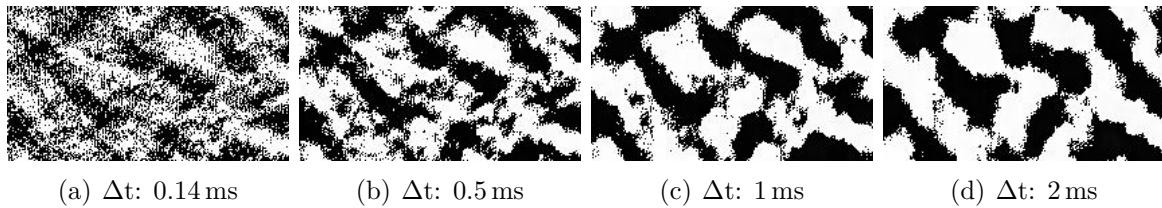


Figure 4.20: Influence of time interval in DHI :Image to Image sequential technique used for a cold flow at 0.3 m/s with different time intervals between the interfering digital holograms. At higher time distances, the structures become more coarse.

4.3.5.3 Holographic interferometric image velocimetry (HIIV)

As discussed above, the presented setup could visualize very small density gradients in fluids. The effects of turbulent eddies in the fluid were enough to create well visible structures in the image2image interferograms. These structures move at the same speed as the fluid, making it possible to trace them similar to the particles used in particle image velocimetry and other techniques derived thereof. By applying a standard PIV cross-correlation algorithm [1] on the interferograms, velocity vector fields of the liquid surrounding the vapor phase could be calculated. As no lens was used in front of the sensor, no calibration target was needed. The vector velocities in m/s could be calculated directly from the pixel values [15]. This method was denoted as holographic interferometric image velocimetry (HIIV) and was successfully applied in nucleate and film boiling as well as on single-phase flows [15]. In comparison to methods using artificial tracer particles such as PIV, this method offered several advantages: Firstly, information on both temperature and velocity distribution in the flow could be obtained. Also, no contamination from particles as well as errors due to particle drift had to be considered. Furthermore, the setup could be run with lower requirements on the equipment: while the PIV system for the same setup required at least 20 W of laser power, the holographic interferograms could be taken using a He-Ne Laser with only 40 mW output power. On the other hand, it has to be noted that the process is depth integrating, giving averaged information on the whole channel depth rather than for an isolated layer as in PIV applications. A similar approach was taken by a number of researchers in the past, using the Schlieren method in combination with a cross correlation

algorithm to detect velocity fields in flows [66, 76, 97]. In comparison, the holographic approach offers higher sensitivity than the Schlieren method, as shown by the author in [11], and a setup that despite being more complex, can be built significantly smaller.

4.4 Experimental procedure for boiling experiments

The boiling experiments were conducted as follows: at the beginning of each experiment, the setup was at room temperature. First, the fluid subcooling was set via the preheater and the coolant flow in the heat exchangers. As the heater surface was always in contact with the fluid, the heater temperature was identical to the fluid temperature at the beginning of the experiments. After reaching a steady state temperature, the heater power was turned on, leading to an increase in surface temperature. The power transferred to the heater depended on the boiling mode used for the respective experiments. For transient experiments, a constant heating power of 2.2 kW was used. This led to a constant increase of the surface temperature until film boiling was achieved for all possible subcoolings and flow velocities. After reaching film boiling, the heating power was shut off manually. For steady state experiments, the heater power was set to a predetermined value at which the desired boiling regimes were reached, resulting in a final steady state heater temperature and associated boiling phenomena. In the preliminary experiments discussed by the author in detail in [13], it could be shown that the heat fluxes achieved in steady state and transient mode were largely identical. Therefore, where applicable, the transient heating mode was used. This was especially the case for the measurements of the critical heat fluxes, which imply a transient process by nature. Steady state heating was used to gain statistical data at given operating points, mainly at the CHF(-) point shortly before the departure from nucleate boiling.

5 Nucleate boiling

In this chapter, experiments in the nucleate boiling regime from the onset of nucleate boiling (ONB) up to the critical heat flux (CHF) shall be discussed. In the first paragraphs, observed boiling regimes and heat fluxes for the channel without inserts shall be discussed to give an overview of the phenomena present in the experiments. After this, effects of the flow inserts shall be discussed with special regard to the changes in critical heat flux. Parts of this chapter have also been published in [7] and [10].

5.1 Observed regimes

After onset of boiling, several regimes could be observed. At low gas-holdups, isolated single bubbles were observed. Following the definitions of Galloway and Mudawar [51], this regime will be denoted as *discrete bubble regime*. At higher wall temperatures and gas holdups, the single bubbles started to coalesce, forming a *coalescent bubble regime*, with bubbles of different size distributions. At heat fluxes close to CHF, Galloway and Mudawar [51] reported a continuous *wavy vapor layer regime*, allowing contact of fresh fluid with the heater only at periodically appearing *wetting fronts*. A similar regime was observed, consisting of larger vapor agglomerations appearing at approximately constant frequencies. These agglomerations also entailed gaps of lower vapor concentration. To distinguish from the definitions of Galloway and Mudawar [51], the regime will be denoted as *highly coalesced bubble regime* and the gaps between the agglomerations as *vapor gaps*. This regime is shown in Fig. 5.1 for a subcooling of 9 K. Similar regimes were also reported by Jiji [75].

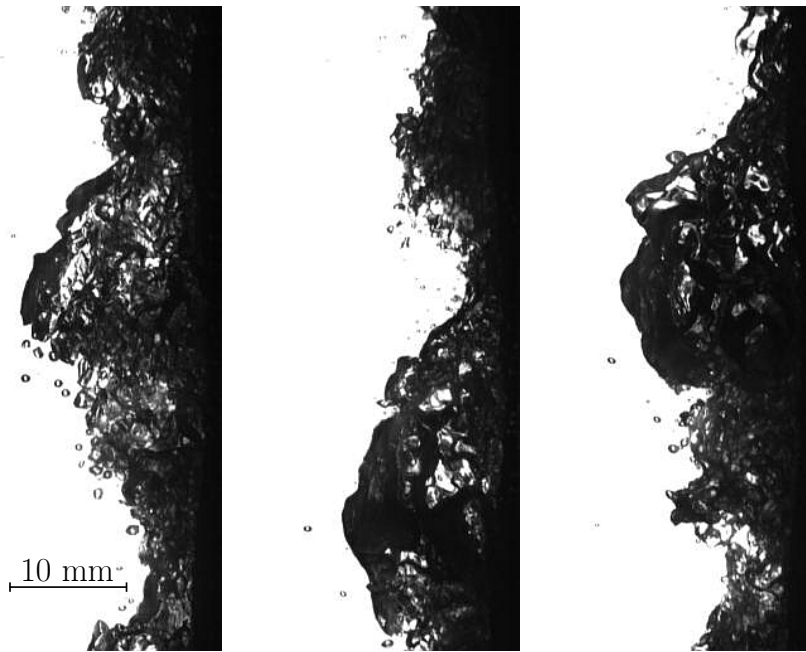


Figure 5.1: Fully developed nucleate boiling in the highly coalesced regime at a subcooling of 9 K, showing vapor agglomerations in the flow. The heater surface is at the right hand side, the flow direction is upwards at a superficial velocity v_s of 0.6 m/s)

5.2 Distribution and velocity of vapor phase

The distribution of the vapor phase over the channel cross section is of particular interest with regard to the phenomena causing the departure from nucleate boiling. Therefore, measurements at CHF(-) were conducted using both high-speed photography and optical probes.

5.2.1 High-speed photography

Fig. 5.2 shows a statistical analysis of the void distribution as averaged intensity per pixel column for a total of 17.000 images recorded at 2 kHz. The heater surface is at the right hand side of the plot at 40 mm, as seen in the above photographs (Fig. 5.1). To determine the velocity of the continuous vapor phase near the heater surface, a cross-correlation algorithm was applied to the high-speed photography images. Fig. 5.3 shows the resulting velocity distribution for subcoolings of 9, 14 and 19 K. For the cross-correlation, the binarized images were used for better detection of the vapor phase. The single bubbles in the channel were removed from the

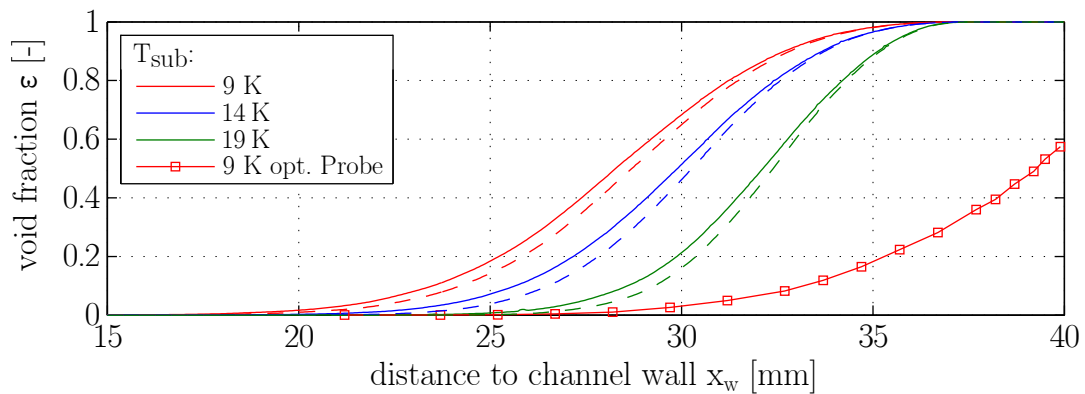


Figure 5.2: High-speed photography: Distribution of the vapor phase over the channel cross section for different subcoolings (heater surface is at the right hand side at $x_w=40$ mm, $v_s=0.6$ m/s). Dashed lines indicate the void fraction after removal of isolated bubbles.

pictures to obtain only the motion of the continuous vapor phase. This resulted in slightly lower overall void fractions, as indicated by the dashed lines in Fig. 5.2. Results were time-averaged over 6000 images, i.e. 3 s. It was shown that the velocity assumes an initial value close to the superficial velocity (0.6 m/s) in areas of low gas holdup, and increases linearly in the region of higher holdups towards the heater surface. The maximum values were observed at distances of 2-4 mm besides the heater surface, with values ranging up to 1.1 m/s. Measurements directly above the heater were not possible due to high vapor concentration. This increase in velocity could be attributed to buoyancy effects brought about by the high vapor concentration close to the heater.

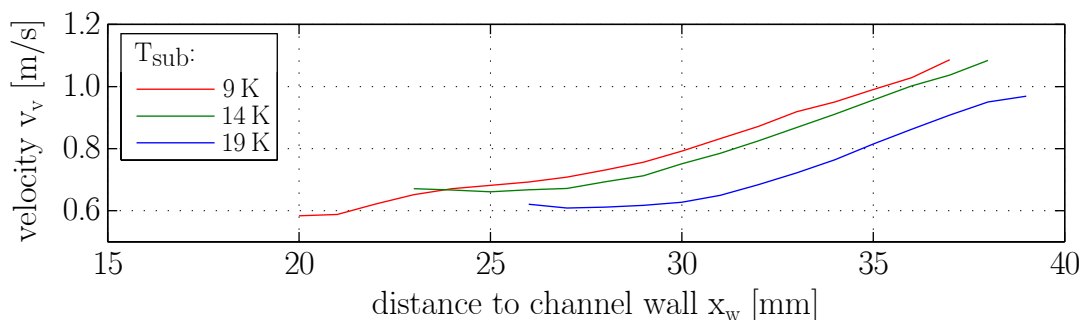


Figure 5.3: High-speed photography: Velocity profiles of the vapor phase for different subcoolings from cross correlation ($v_s=0.6$ m/s).

5.2.2 Probe measurements

Fig. 5.2 also serves to show one of the major shortcomings of the photographic technique, i.e. the inability to observe three-dimensional flows with higher void fractions, as they become opaque due to the depth integrative nature of the technique. In Fig. 5.2, this is revealed by the void fraction showing up as 100% near the heater surface, whereas the actual concentration is significantly lower. As such, the void measurements from photographic methods are of a rather qualitative nature for a channel with significant depth as used here. For void measurements, the optical probes offer better applicability due to the point wise measurement. In Fig. 5.2, the vapor distribution at 9 K for probe measurements at varied positions is shown together with the results from HS photography, showing a similar distribution but significantly lower void values, reaching a maximum of 0.57 at a distance of 0.1 mm to the heater surface. As discussed in Sec. 4.3.3, the probes allow time resolved measurements over the whole boiling curve for transient experiments, in contrast to the photography which was limited to recording times of less than 10 s. Fig. 5.4 shows the measured maximum void fractions measured in transient experiments at fixed probe positions of 2, 4 and 6 mm from the heater surface at the trailing edge. It was observed that the actual void fractions were significantly lower than what would be expected from the photographic method, and they also showed a strong increase with decreasing subcooling.

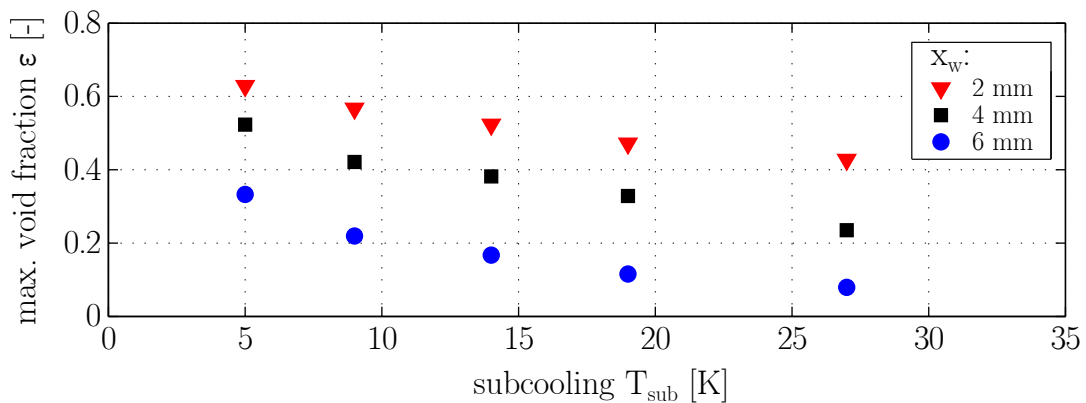


Figure 5.4: Optical probes: maximum void fractions plotted against the fluid subcooling at different distances from the heater surface x_w ($v_s=0.6$ m/s).

Summarizing the results from high-speed photography and optical probes, the following statements can be made: In channel flow without inserts, the

vapor phase is concentrated mainly near the heater surface, penetrating no further than to the middle of the channel cross section at 20 mm. The flow was observed to consist mostly of a larger area of coalesced vapor structures, with only few isolated bubbles. Removing the isolated bubbles from the images resulted in less than 10% reduction in void fraction from all subcoolings. The overall void fraction increases with decreasing subcooling, leading to an increased thickness of the vapor layer which thus penetrates further into the channel. While the photographic technique gives only qualitative information on the concentration of vapor due to depth integration, quantitative values can be obtained with the optical probes. Using a traversing probe, the vapor concentration could be shown to range up to 57% at a distance of 0.1 mm to the heater surface, decreasing with further distance. Using probes at fixed positions in transient boiling experiments, the vapor distribution over the whole boiling curve could be analyzed, showing increases in the maximum void fraction with decreasing subcooling for all probe positions.

5.3 Vapor agglomerations

At higher heat fluxes, larger agglomerations of vapor were observed in the channel for all subcoolings, forming the *highly coalesced regime* as shown in Fig. 5.1. These agglomerations appeared periodically at approximately constant frequencies. Due to the large fluctuations of vapor fraction, fluid velocities and flow directions in the wake of these agglomerations, these can be expected to pose an important factor in heat transfer close to CHF. Therefore, special interest was given to the behavior of these agglomerations, especially to the size and frequencies of the vapor structures themselves and to the effects happening in the wake, such as liquid motion and temperature distribution in the fluid. Fig. 5.5 shows the structure of typical vapor agglomerations for a fluid subcooling of 9 K over the whole optically accessible area and in a detailed view.

5.3.1 Size

As a first measurement, the average dimensions of the agglomerations were calculated from high-speed photography. The resulting dimensions for dif-

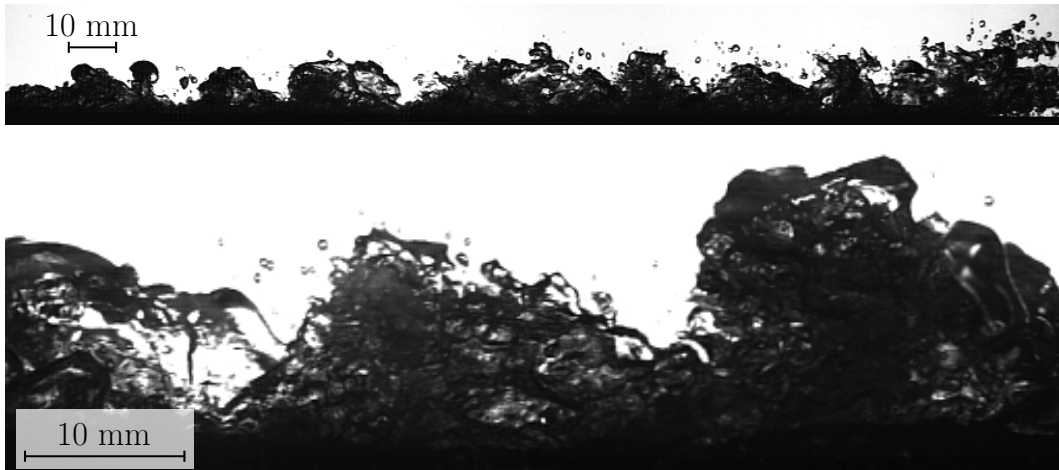


Figure 5.5: Photographs of the vapor structure over a larger area (above) and in detailed recording of the middle section (below), both for fully developed nucleate boiling at inlet subcooling of 9 K and flow superficial velocity of 0.6 m/s (images not synchronous). The images are rotated by 90 degrees, i.e. the inlet is on the left side.

ferent subcoolings are given in Tab. 5.1. For a decrease in subcooling, a linear increase of the mean agglomeration area was observed.

Table 5.1: Length (in flow direction), width, and area for vapor agglomerations close to CHF at different subcoolings from high-speed photography.

T_{sub} [K]	Length [mm]	Height [mm]	Area [mm ²]
19	5,5	10,0	55,1
14	7,0	11,9	83,2
9	8,5	13,1	111,4

5.3.2 Liquid entrainment

While the vapor agglomerations appeared as continuous vapor structures in the videometric measurements, the optical probes offered further insight into the structure of the agglomerations. The probes detected the vapor bulks as a scatter of single signals, meaning that liquid was still distributed within the agglomerations. Fig. 5.6 shows the resulting signal for one larger agglomeration, taken from a synchronous measurement with high-speed photography and optical probes. The fraction of liquid entrained within

the agglomerations was measured to range between 5 and 30%. These results are in contrast to the results given by Galloway and Mudawar [51], who reported continuous vapor phases close to CHF.

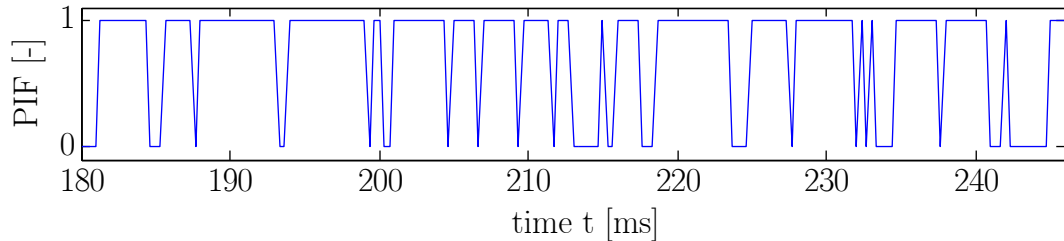


Figure 5.6: Probe measurement showing the structure of one agglomeration with entrained liquid (probe at 2 mm distance to the heater surface, subcooling 5 K). Liquid entrainment is evidenced by the scatter of the phase indicator function (PIF), which is 1 for vapor and zero for liquid.

5.3.3 Frequencies

Another important aspect taken into account was the average frequency at which the vapor agglomerations appeared in the channel. The frequencies were detected from high-speed photography using both a FFT analysis and a peak detection algorithm. In addition, the frequencies were also calculated from the probe measurements using an FFT-algorithm. The frequencies calculated from high-speed photography approximately showed a constant distribution of the frequencies, with a mean frequency of approx. 25 Hz for all subcoolings. As the agglomerations were most developed at low subcoolings, the results were clearest here. However, also for lower subcoolings average frequencies in the range of approx. 25 Hz were observed. The distribution of the frequencies for subcoolings of 9, 14 and 19 K is shown in Fig. 5.7. The frequencies showed a rough Gaussian distribution for all the subcoolings (shown in red in Fig. 5.7). The probe measurements gave values of 18 to 21 Hz for different subcoolings, with the values slightly increasing with subcooling as given in Tab. 5.2. The results from the probe measurements are given in Tab. 5.2. The clearest results were detected for the probe 6 mm from the heater surface, as the other probes tended to be immersed in the vapor layer, especially for lower subcoolings. As the foot of the agglomerations often still touches the probes, agglomerations with smaller entrained wetting gaps can not always be detected, thus a lower

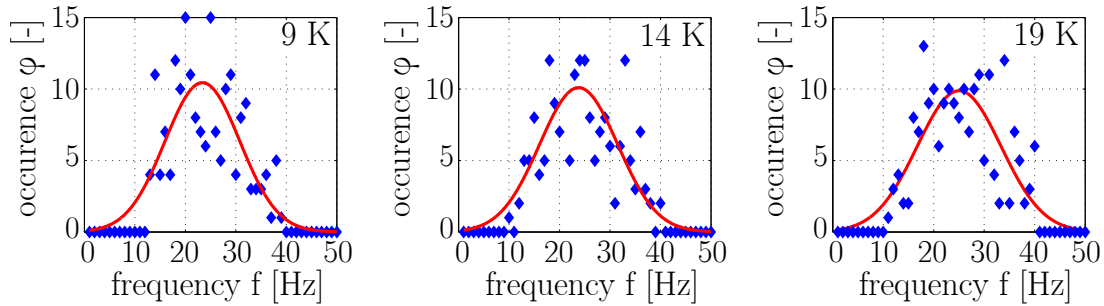


Figure 5.7: Distribution of agglomeration frequencies for steady state boiling at CHF(-) for different subcoolings, calculated from high-speed photography, each for a recording time of 8.73 s and 17469 images ($v_s=0.6$ m/s).

Table 5.2: Average frequencies of vapor agglomerations measured by optical probes at different distances to the heater surface. Frequencies were calculated from first 10 Maxima of the FFTs.

$T_{sub}[K]$	average frequency [Hz]		
	N1 (2 mm)	N2 (4 mm)	N3 (6 mm)
5	11,71	11,67	17,60
9	10,89	13,38	18,99
14	13,00	14,12	20,32
19	12,16	15,83	20,99

frequency is measured. Even though subcooling showed a strong influence on the absolute size of the agglomerations, the average frequencies stayed mostly constant for both photographic and probe measurements. This led to the assumption that the initial formation of the agglomerations takes place in a superheated sublayer close to the heater surface, on which the bulk flow temperature has only little influence.

5.3.4 Velocities

Using a cross-correlation algorithm as discussed in Sec. 4.3.2.2, the average velocity of the agglomerations was calculated from the high-speed videos. For a superficial flow velocity of 0.6 m/s and different subcoolings, the calculated velocities of the agglomerations are given in Tab. 5.3. For the given flow rate, it was observed that the average slug velocity was significantly higher than the superficial velocity and approximately constant for all subcoolings. Previous PIV-measurements had shown the fluid velocity to be in

the range of the superficial velocity, thus the velocity of the agglomerations was approx. 50% above the mean flow velocity. The measured velocities show the average for all larger slug like structures, and are thus slightly higher than the averaged vapor velocity shown in Fig. 5.3. The velocity was measured separately for the peaks of the agglomerations, i.e. the area penetrating furthest into the channel, and the tails of the agglomerations, meaning the broader base of the agglomerations close to the heater surface. It was observed that the velocity measured for the peaks was lower than that of the tails, meaning the area closer to heater surface moved at higher velocities.

Table 5.3: Velocities for peaks and tails of agglomerations and increase in relation to the superficial flow velocity v_s (0.6 m/s) at different subcoolings.

T_{sub} [K]	vertical velocity [m/s]		increase in rel. to superf. flow vel. v_s [%]	
	peaks	tails	peaks	tails
19	0,93	1,18	55	97
14	0,93	1,25	55	108
9	1,01	1,24	68	107

5.3.5 Behavior in the wakes of vapor agglomerations

The group of Mudawar et al. [50, 55] described so called wetting fronts (see Sec. 2.3.2.4), areas of lower void fraction between larger vapor structures, and identified them as an important aspect for heat transfer in highly developed nucleate boiling. Similar structures were observed here, however the wavy behavior was less clear than shown in the reports cited above. This can be attributed to the increased channel depth used here: while the reports cited above used channels of 1.6 mm depth, the channel used here had a depth of 40 mm resulting in a far more “three dimensional” flow. Thus, clear view of the wetting fronts in the vapor structure was often obstructed by bubbles in front of the area not covered by vapor. However, gaps in the vapor structure following the larger agglomerations could still clearly be seen. Examples of these gaps are shown in Fig. 5.5. To further analyze the effect of these areas of lower void fraction on the boiling process, the flow field was observed with high-speed PIV, and the the temperature

distribution was analyzed with digital holographic interferometry. These experiments will be discussed in the following paragraph.

5.3.5.1 Flow field in the wake of vapor agglomerations

To give insight into the flow fields around and in the wake of the vapor agglomerations, high-speed particle image velocimetry (PIV) was used. As the vapor phase negatively influenced the analysis, it was masked and thus excluded from the PIV process. The resulting vector fields for the wake of a vapor gap are shown in Fig. 5.8 (a). For better visualization, the mean vertical flow velocity was subtracted from the vectors in this image. This parameter was also analyzed using the holographic velocimetry HIIV

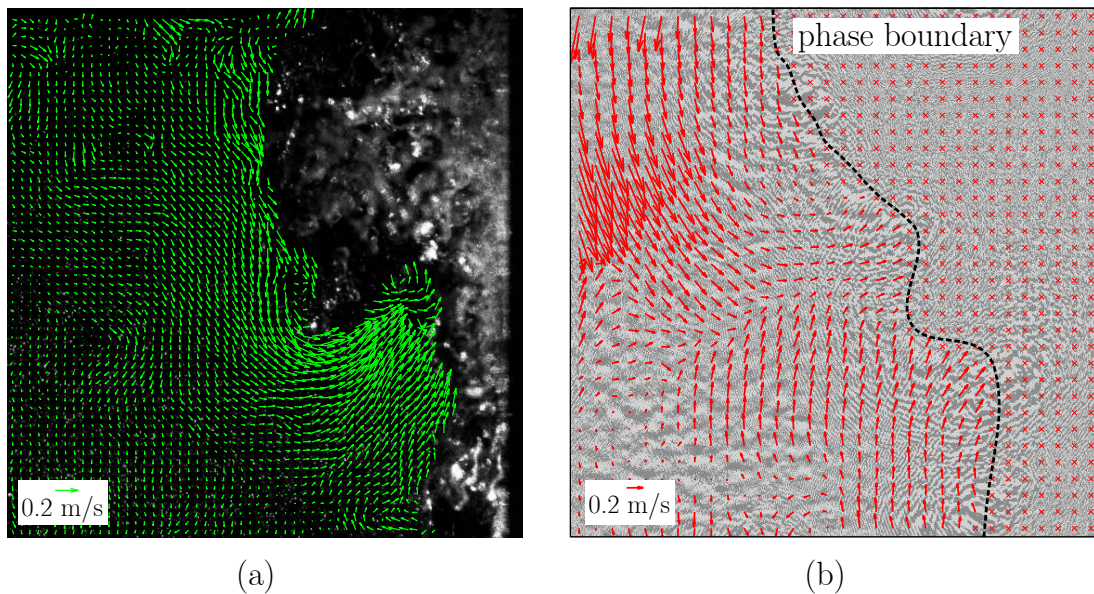


Figure 5.8: Velocity field in the wake of a vapor agglomeration from PIV (a) and HIIV (b) measurement (mean vertical flow subtracted for both techniques). The heater surface is at the right hand side, the main flow direction is upward at a superficial velocity v_s of 0.6 m/s.

developed within the project [15]. The resulting vector fields are given in Fig. 5.8 (b). Both techniques showed an acceleration of the liquid phase towards the heater surface at horizontal velocities in the range of 0.2 m/s. Considering the thin vapor layer present in these areas, it has to be assumed that the fluid accelerated in the wake reaches the heater, causing additional cooling of the surface.

5.3.5.2 Temperature distribution in the wake of the agglomerations from digital holographic interferometry

An important parameter in discussing the heat transfer close to CHF is the temperature distribution in the fluid. Due to difficult accessibility of this parameter, only few results have been published. However, especially for discussing the effects of the vapor gaps (or wetting fronts), it is important to know if the fluid that reaches close towards the heater is subcooled or saturated to correctly evaluate the importance of the quenching effects occurring in the vapor gaps. For a superficial flow velocity of 0.6 m/s and fluid subcooling of 5 K, two intensity plots of the holographic interferograms are given in Fig. 5.9. The right border of the image is at a distance of 3 mm to the heater surface. The lines in the images represent areas of constant density, or, for fluids, constant temperature. The phase boundary can be clearly distinguished from the bulk flow, while around the phase boundary only little thermal differences can be observed. The inhomogeneities present in the flow can be attributed to the stochastic density distributions of the turbulent cells and were also observed in unheated single phase flow. Concerning the vapor gaps and the temperature distribution of the fluid in the wakes, the holographic interferograms showed a mostly homogeneous fluid temperature distribution between the vapor agglomerations. The fluid temperature was in the range of the bulk flow temperature, meaning strongly subcooled liquid was present between the agglomerations. With regard to the heat transfer mechanism, it may be concluded that the gaps or wetting fronts do indeed have a strong influence on the heat transfer mechanisms close to CHF.

5.3.6 Dynamic behavior of vapor agglomerations

The previous paragraphs mainly gave a statistical overview for the agglomerations and showed results on the flow patterns for very short time intervals. As the behavior of the boiling system was highly dynamic, the following section shall provide a more detailed description of the transient behavior of the agglomerations. It was observed that the shape and structure of the agglomerations hardly remained constant while propagating along the channel. Ongoing coalescence as well as breakup and motion perpendicular to the bulk flow direction led to a constant variation of the agglomeration's

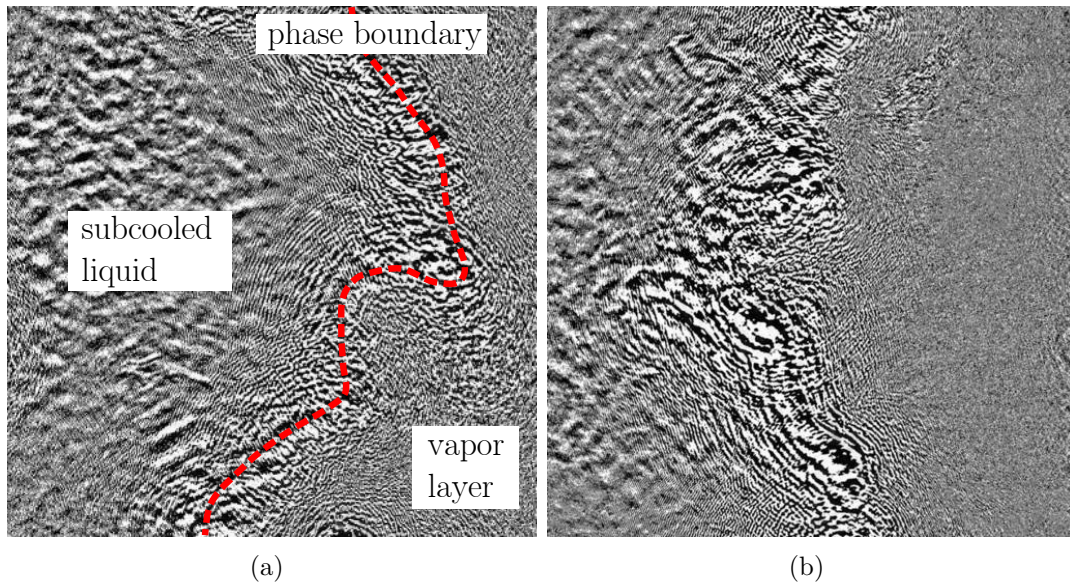


Figure 5.9: Temperature distribution in the vicinity of vapor agglomerations from DHI: Interference phase maps of a wetting front (a) and a vapor agglomeration (b), showing the subcooled liquid in the bulk and the wake of the agglomerations. The heater position is 3 mm outside the right hand border, the recorded area is $20.5 \times 20.5 \text{ mm}^2$.

overall structure. Fig. 5.10 shows photographic images of one vapor agglomeration propagating upwards in the channel over time from two independent recordings. In general, the following main observations were made: As ag-

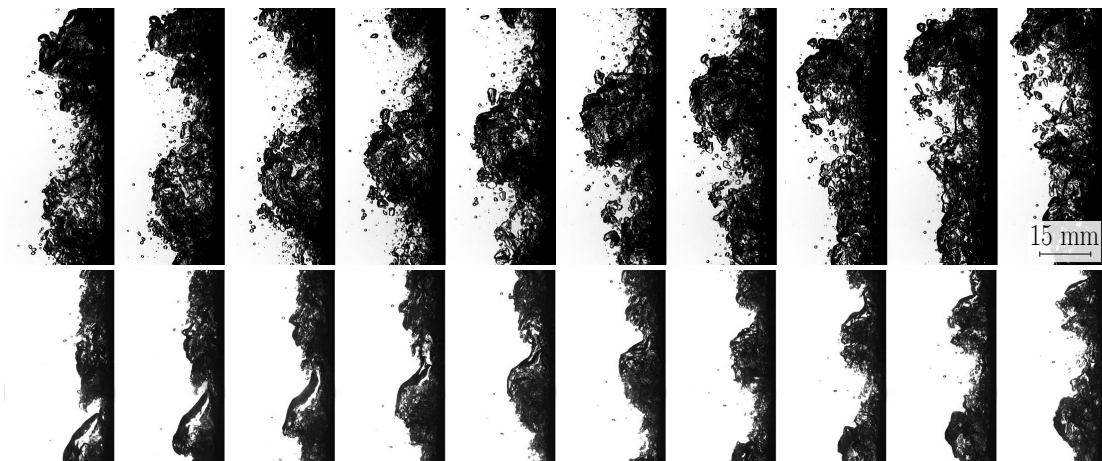


Figure 5.10: Development of vapor agglomeration over time from two independent recordings (subcooling: 9 K, bulk flow velocity: 0.6 m/s, time interval between pictures: 4 ms).

glomerations propagate upwards along the channel, vapor from the lower third of the agglomerations has a tendency to move towards the heater sur-

face, reducing the size of the overall agglomerations. This could also be interpreted as a larger part of agglomeration being sucked into the main vapor layer. This effect can be attributed to the velocity gradient perpendicular to the heater surface, seen as velocity difference between the peaks and the gaps of the agglomerations (see Tab. 5.3) and also evidenced in the gradient towards the heater surface discussed in Sec. 5.2.1. This velocity difference and the associated difference in pressure act as a driving force, pulling larger bubbles towards the layer that moves at higher velocity. This velocity difference between the phases and the associated lift-force are discussed in further detail in Sec. 8.4.1. Also, as the agglomerations move upwards, non coalesced single bubbles were observed to detach from the main agglomeration and to remain behind, often coalescing into the next agglomeration.

5.4 Influence of inserts

To study the influence of turbulence and secondary flows on the boiling process, experiments with different fluid subcoolings and flow rates were conducted with the inserts discussed in Sec. 4.2. The results were also published in [6, 10, 12]. For an illustration of the macroscopic changes in the boiling process with added turbulence, Fig. 5.11 shows photographic images of the vapor distribution in the channel at CHF(-) over a length of 200 mm for the case without inserts (a) and with the single hole orifice (b). It can clearly be seen that the added turbulence leads to an increased distribution of vapor in the channel. Even from these images alone, it is possible to imagine the changes resulting from the additional turbulence, such as better heat transfer due to mixing of saturated and subcooled liquid and the better removal of vapor from the heater surface. These points shall be further elaborated in the following paragraphs, with special emphasis on the impact on the critical heat flux and the vapor and bubble size distribution.

5.4.1 Heat fluxes

Due to the technical importance, the resulting heat fluxes with inserts in comparison to the empty channel without inserts were of special interest. All experiments discussed here were conducted in transient mode (see Sec. 4.4).

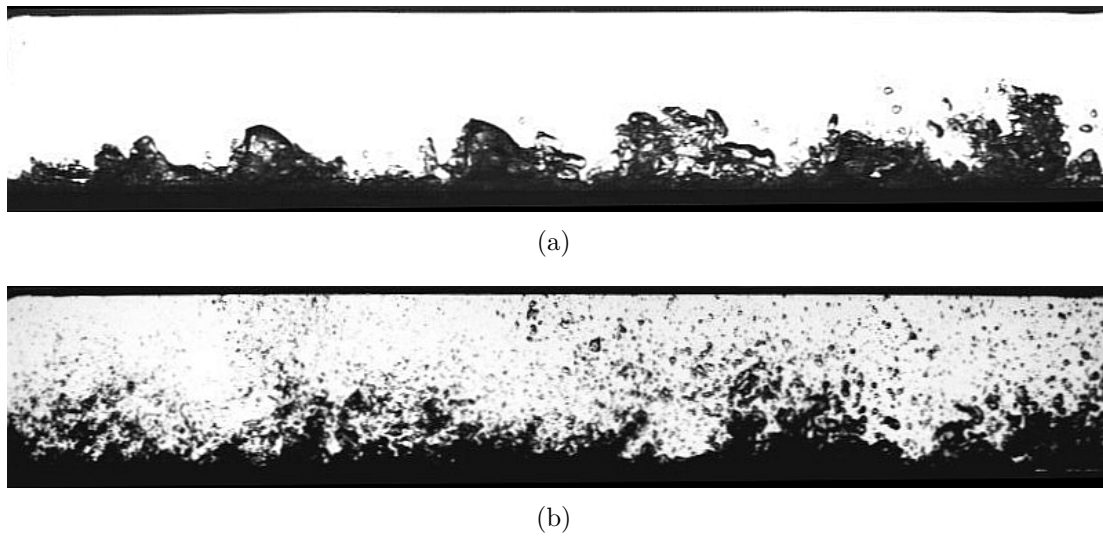


Figure 5.11: Flow regimes close to CHF along the channel without inserts (a), and with single-hole orifice (c) ($T_{sub}=9$ K, $v_s=0.6$ m/s).

5.4.1.1 Overall heat flux

At first, the heat flux over the whole boiling curve was analyzed. Fig. 5.12 shows the heat fluxes \dot{q} for the orifice and the empty channel at a subcooling of 27 K. It was observed that with the orifice inserted, the heat flux is increased over the whole boiling curve, including the return to nucleate boiling hysteresis. Similar behavior was observed for the twisted tape insert as soon as boiling occurred, however the effects were weaker than with the orifice. For lower subcoolings the distance between the boiling curves was observed to decrease, an effect which will be discussed in detail for the CHF in the next paragraphs.

5.4.1.2 Critical heat flux

Special regard was given to the critical heat fluxes obtained with the inserts. As seen from the results discussed earlier, critical heat flux was increased by the inserts as well. To give more insight, changes with subcooling and flow rate were analyzed in particular.

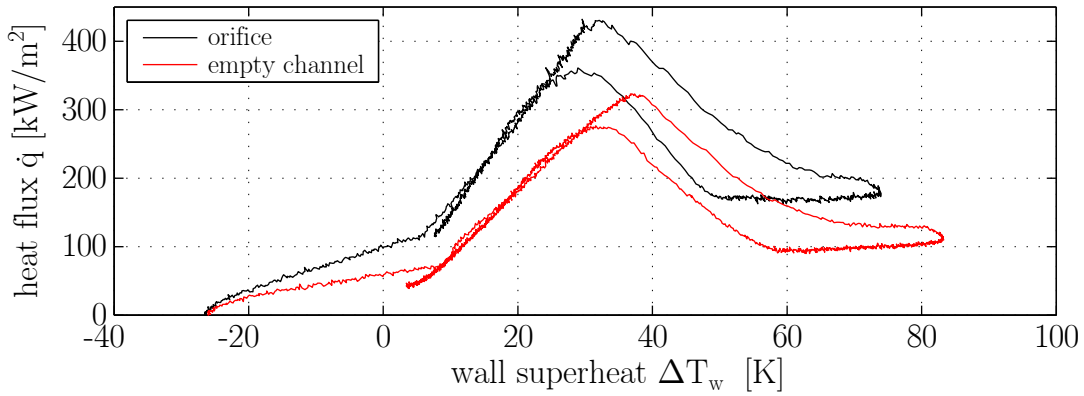


Figure 5.12: Heat fluxes along the entire boiling curve up to fully developed film boiling (upper part of curves) and back into nucleate boiling (lower part) for empty channel and orifice insert ($T_{sub}=27$ K, $v_s=0.6$ m/s).

5.4.1.3 Influence of subcooling

Fig. 5.13 shows the measured critical heat fluxes at the upstream measuring position for the two inserts and the empty channel at superficial fluid velocity of 0.6 m/s. It can be observed clearly that both inserts enhance the critical heat flux, with the orifice again showing stronger influence than the twisted tape. A linear dependence of CHF to subcooling was observed, however the inserts showed a steeper slope, meaning their influence increased with higher subcoolings. The increases towards the empty channel case were observed to range between approx. 17 to 28% for the orifice and 4 to 7% for the twisted tape for subcoolings ranging from 5 to 27 K. The calculated increases in critical heat flux are given in Tab. 5.4.

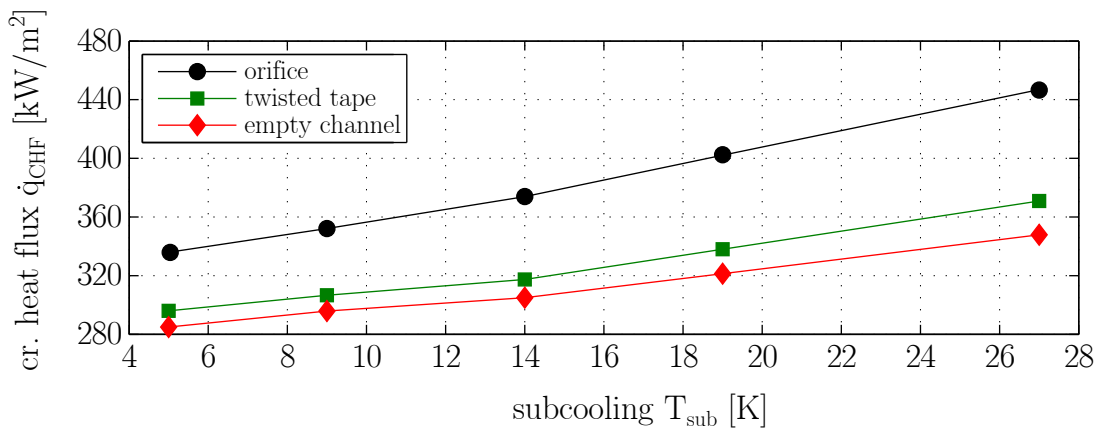


Figure 5.13: Influence of inserts on CHF at different fluid subcoolings ($v_s=0.6$ m/s).

Table 5.4: CHF increase to reference for different subcoolings at $v_s=0.6$ m/s.

CHF increase [%]	T_{sub} [K]				
	5	9	14	19	27
twisted tape	3.9	3.6	4.1	5.2	6.6
orifice	15.9	19.0	22.6	25.3	28.4

5.4.1.4 Influence of flow rate

To study the influence of the flow rate on the CHF increase with the inserts, experiments were conducted at superficial flow velocities of 0.3, 0.6, and 1.2 m/s. Tab. 5.5 gives the resulting increases in CHF compared to the empty channel case for a fluid subcooling of 27 K. It was observed that all

Table 5.5: CHF increase to reference for different flow velocities at $T_{sub}=27$ K.

CHF increase [%]	superficial velocity [m/s]		
	0.3	0.6	1.2
twisted tape	1.2	6.6	9.7
orifice	19.4	28.4	61.6

inserts show linear increase of CHF with the flow rate as expected from literature, however the inserts provide a steeper increase. Again, this effect was most notable for the orifice.

5.4.2 Influence on vapor distribution

As mentioned above, added turbulence and secondary flows led to significant changes in the distribution of vapor in the channel. While the vapor was mainly concentrated near the heater surface for the case without inserts, a more homogeneous distribution of vapor in the channel was observed with inserts.

5.4.2.1 Photographic analysis

High-speed photography was used to measure the integral concentration of vapor with and without the inserts as well as sizes and numbers of bubbles dispersed in the flow. For the empty channel and the two inserts, the twisted tape and the single-hole orifice, a photographic image of the vapor distribution is given in Fig. 5.14. The time averaged distribution of the void

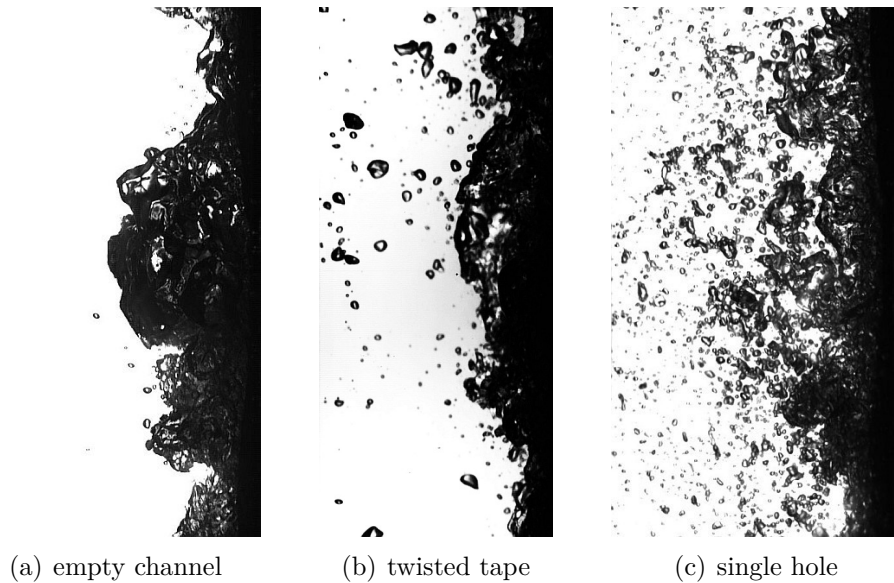


Figure 5.14: Detailed view of the flow regimes close to CHF for channel without inserts, with the twisted tape, and with single-hole plate ($T_{sub}=9$ K, $v_s=0.6$ m/s).

fraction is shown in Fig. 5.15 for the two inserts and the empty channel at different fluid subcoolings. As can already be seen from the photographs in Fig. 5.14, the vapor is distributed more evenly over the channel for the cases with the inserts, with the orifice showing a stronger effect than the twisted tape. As discussed above (see Sec. 5.2), in regions close to the heater (<5 mm) the photographic method always showed a gas holdup of 1 as result due to the depth integration. This was also observed for the analyzed inserts, however the observed decline in vapor at distances further from the heater surface was far less steep than for the empty channel case, with both inserts showing gas holdups over the whole visually accessible channel section. As expected from the turbulence intensities, the effects of the twisted tape insert were between the values achieved for the empty channel and the orifice. This can mainly be attributed to the higher number of isolated bubbles present in the channel, as can also be seen in the bubble size

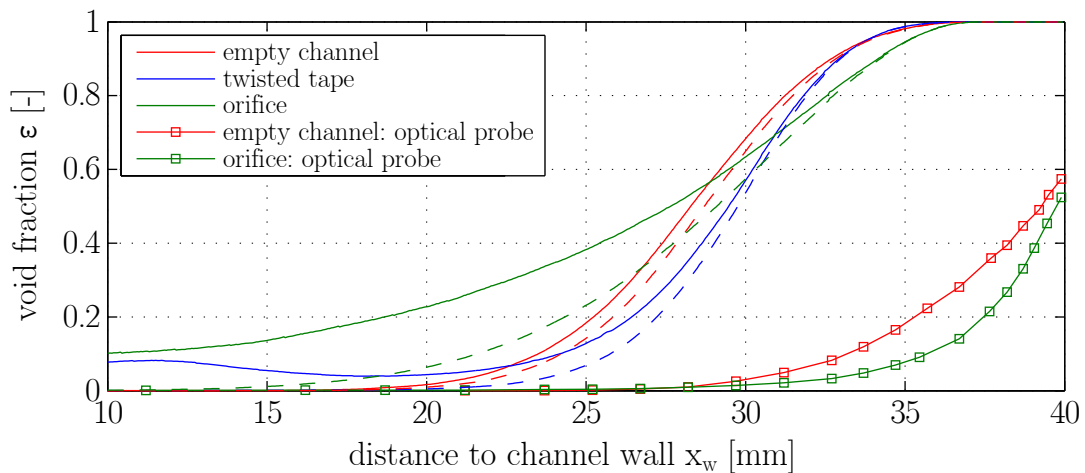


Figure 5.15: High-speed photography: Time averaged distribution of the void fraction in the channel for different inserts at 9 K subcooling. The heater surface is at the right hand side at 40 mm ($v_s=0.6$ m/s). Dashed lines indicate the void fraction after removal of isolated bubbles.

distribution. Fig. 5.16 shows the number and size distributions of isolated bubbles time averaged over 17 469 single images (≈ 8.73 s). As can already be deduced from the photographic images shown in Fig. 5.14, the inserts lead to a higher number of single bubbles, especially with the orifice.

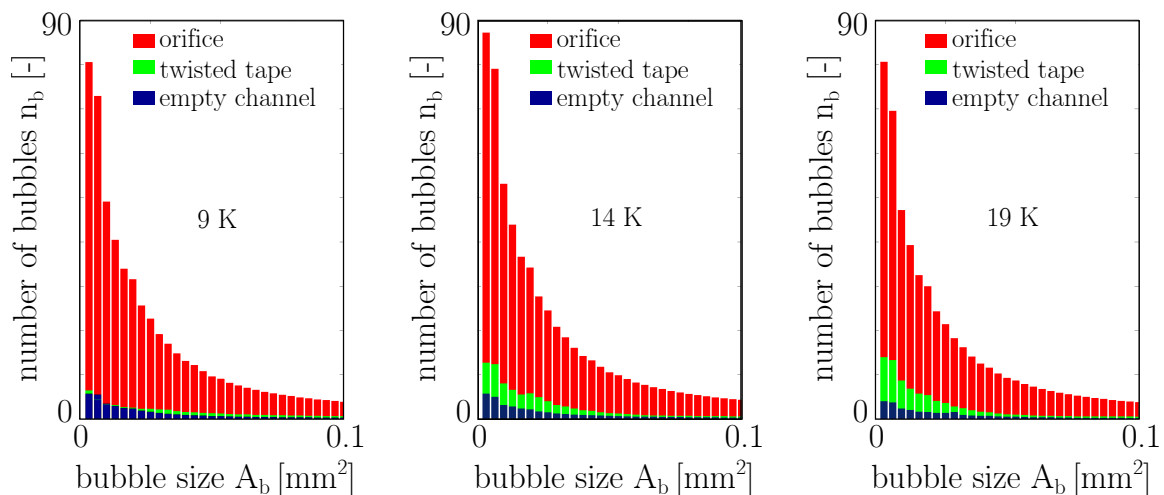


Figure 5.16: High-speed photography: Time averaged size distribution of isolated bubbles (continuous vapor layer near heater surface removed) in the channel for different subcoolings and inserts ($v_s=0.6$ m/s).

5.4.2.2 Optical probes

To gain further insight into the effects of the insert on the layer close to the heater surface, optical probes were employed. As differences were most significant for the orifice, only this insert was compared to the empty channel. In addition to the results from high-speed photography, Fig. 5.15 also shows the results obtained by traversing an optical probe for the empty channel and the orifice at 9 K subcooling. As discussed above for the empty channel case (see Fig. 5.2), the probes offered precise local measurements in contrast to the depth integrated results from photography. The probes were

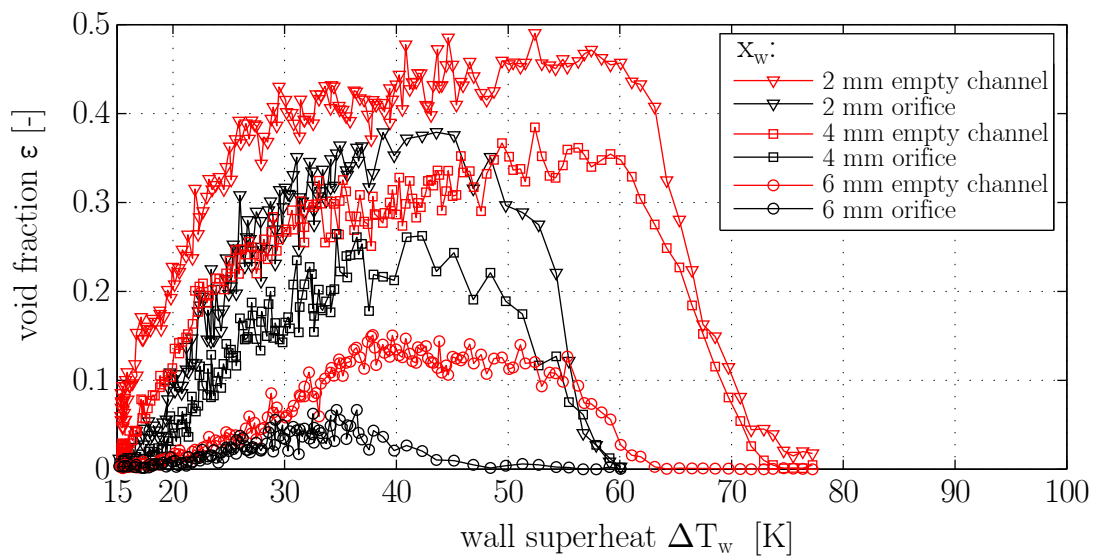


Figure 5.17: Optical probes: Development of void fraction over the whole boiling curve at a subcooling of 14 K for the single whole orifice and the empty channel for three fixed probe distances from the heater surface x_w ($v_s=0.6$ m/s).

also used in transient experiments over the whole boiling curve. Fig. 5.17 shows the development of the void fraction over the whole boiling curve at a subcooling of 14 K for the empty channel and the orifice for fixed probe positions or 2, 4 and 6 mm. Similar to the results shown in Fig. 5.15 for steady state boiling, the local void fraction was observed to be lower for all positions. Apart from this, it was observed that the maximum void fraction was reached at lower wall superheat with the orifice despite the higher heat fluxes, similar to the effects achieved by increasing the subcooling for the empty channel. Fig. 5.18 shows the measured maximum void fractions for varied subcoolings with the orifice and for the empty channel case. It was observed that the influence of the inserts on the max. void fraction increases

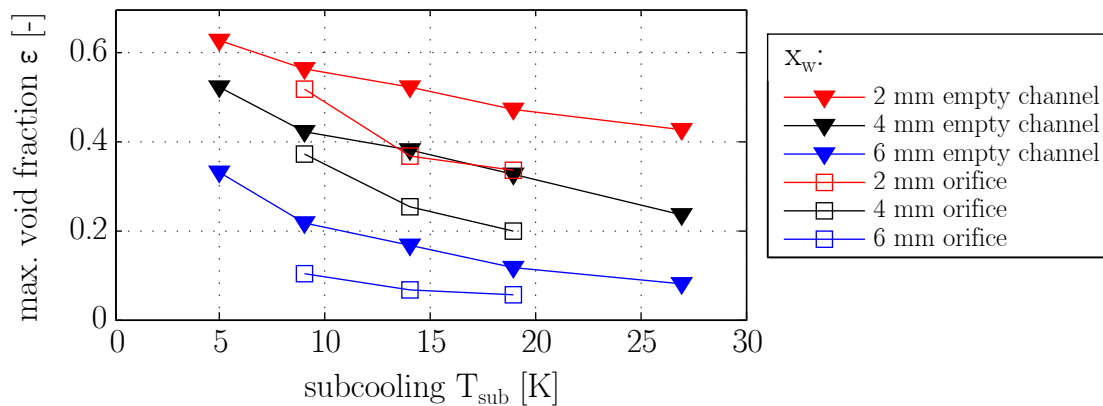


Figure 5.18: Maximum void fractions measured with the optical probes for the empty channel case and the orifice plotted against the fluid subcooling at different distances from the heater surface x_w ($v_s=0.6$ m/s).

with the distance to the heater and the fluid subcooling, as evidenced by the smaller distance of the curves in Fig. 5.18 for these operating points. Comparing the maximum void fractions for the case with the orifice and the empty channel reference, at a subcooling of 9 K only a relative reduction of 8 % in max. void fraction was measured at 2 mm from the heater. This increased to 12 % at 4 mm and 52 % at 6 mm. Similarly, for subcoolings of 14 and 19 K, the change in max. void increased from 29 to 61 % and from 30 to 65 % respectively. Tab. 5.6 summarizes these values. This behavior could

Table 5.6: Change in maximum local void fraction compared to reference for different positions of the optical probes at varying subcoolings ($v_s=0.6$ m/s).

relative change in max. void fraction [%]	probe distance to heater surface		
	2 mm	4 mm	6 mm
9 K subcooling	8	12	52
14 K subcooling	29	33	61
19 K subcooling	30	39	65

be attributed to two effects: firstly, secondary flows are generally blocked by the vapor phase close to the heater. Thus, the inserts mainly affect the outer regions of the coalesced layer while the regions close to the surface remain unaffected. With lower subcoolings, the overall vapor concentration increases, leading to the formation of a thicker coalesced vapor area above the heater surface. This adds to the first effect, leading to even smaller

effects closer to the heater surface. From the results shown here, it can be concluded that the thickness of the coalesced layer present at 9 K (approx. 5 mm as seen in Fig. 5.15) poses a limit for the possible penetration depth of the turbulence. At even lower subcoolings and thus higher void fractions, it has to be expected that the inserts will have negligible effect on the void fraction close to the heater.

5.4.3 Periodic behavior of vapor layer

As discussed in Sec. 5.3 for the channel without inserts, the vapor layer was observed to show a periodic behavior at high heat fluxes, with larger vapor agglomerations passing through the channel at constant intervals. This behavior was also observed with the flow inserts. Due to the higher number of isolated bubbles in the channel, the agglomerations were smaller and less clearly observable, but could still be detected using the techniques given above.

5.4.3.1 Sizes of agglomerations with flow inserts

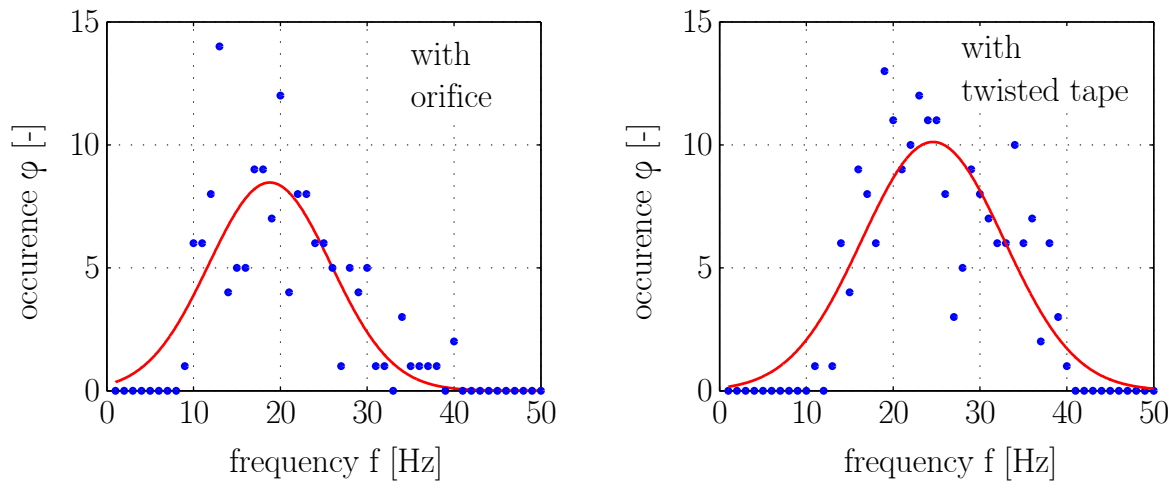
As mentioned, the size of the agglomerations was observed to decrease together with the local void fraction for all inserts. Tab. 5.7 shows the measured geometries for the agglomerations at different subcoolings with the two main inserts. As expected from the general vapor behavior, the change in size compared to the empty channel case was strongest at higher subcoolings, and it was higher for the orifice than for the twisted tape.

5.4.3.2 Frequencies

The frequencies of vapor agglomerations were also analyzed for the experiments with flow inserts, as shown in Sec. 5.3.3 for the case without inserts. Fig. 5.19 shows the resulting distribution of frequencies for a subcooling of 14 K for both inserts calculated from high-speed photography. For the twisted tape, no significant change was observed in comparison to the empty channel case, with an average value of 25 Hz for the frequencies. For the orifice, the frequency was slightly lower, with an average value of 18 Hz. This could be attributed to the higher number of single bubbles and the

Table 5.7: Dimensions of vapor agglomerations for different inserts and subcoolings ($v_s=0.6$ m/s).

T_{sub} [K]	Length [mm]	Height [mm]	Area [mm ²]	Δ_{Area} [%]
orifice				
19	2,3	5,0	11,6	- 78,9
14	4,2	7,3	31,0	- 62,7
9	6,2	9,6	59,3	- 46,8
twisted tape				
19	2,7	9,6	25,6	- 53,5
14	4,3	11,2	47,7	- 42,7
9	4,3	13,1	56,4	- 49,4

**Figure 5.19:** Distribution of agglomeration frequencies for steady state boiling at CHF(-) with the orifice insert (left) and with the twisted tape (right) for different subcoolings. The frequencies were calculated from high-speed photography, each for a recording time of 8.73 s and 17469 images ($v_s=0.6$ m/s).

smaller size of the agglomerations, making detection of the agglomerations more challenging. Thus, the used algorithm detected fewer agglomerations, leading to lower frequencies. However, it has to be expected that the actual frequency is still in the same range as for the empty channel and the twisted tape. Other subcoolings were analyzed as well, but again showed no significant influence on the agglomeration frequencies. The frequencies were also analyzed with the optical probes, which confirmed the results.

5.4.4 Velocities of vapor agglomerations with inserts

The velocities of the agglomerations were analyzed for the channel with inserts as well. Changes of velocity in comparison to the empty channel were rather small and within the error margin, leading to the conclusion that similar to the frequency, the inserts have only limited effect on the agglomeration velocity.

5.4.5 Heat distribution from holographic interferometry

Digital holographic interferometry revealed the heat distribution in the flow to be highly heterogeneous when inserts were added. Fig. 5.20 shows the resulting interference phase maps of the holographic interferograms. While the empty channel case resulted in a mainly separated flow of unheated liquid in the bulk and hot vapor and liquid near the heater surface (see Sec. 5.3.5.2), the inserts showed strong mixing of liquid of different temperatures in the flow. Clear phase boundaries could no longer be observed.

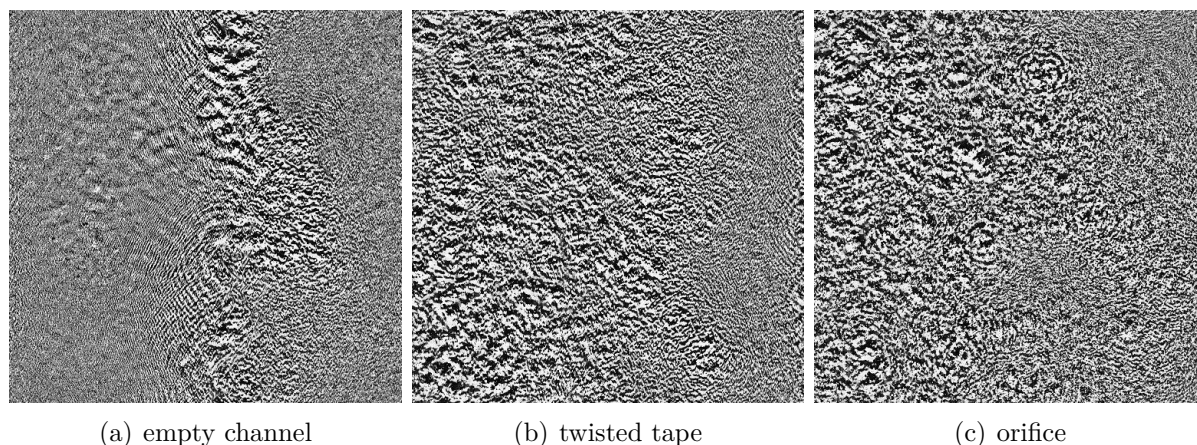


Figure 5.20: Interference phase maps showing the heat distribution in the channel with and without inserts ($T_{sub}=27\text{ K}$, $v_s=0.6\text{ m/s}$).

5.4.6 Summary on the influence of inserts

In summary, the following effects were observed with the addition of flow inserts: while the overall character of the boiling regimes remained largely

unchanged, significant changes in the distribution of vapor were observed. As was seen both from HS photography and optical probes, the vapor became more evenly distributed over the channel cross section. This could mainly be attributed to a significantly larger number of isolated bubbles in the channel, as was seen from the bubble size distributions calculated from the photographs. As the area of concentrated vapor near the heater surface became smaller with the application of inserts, the periodically appearing vapor agglomerations were also observed to decrease in size. However, the frequency of the agglomerations remained constant at around 25 Hz as seen for the empty channel case. This confirmed the assumptions discussed earlier, that the initial growth of the agglomerations takes place in a sublayer close to the heater that is largely isolated from the main flow and thus is not affected by the effects of the inserts. Apart from the better distribution of vapor in the channel, using digital holographic interferometry it was also shown that the heat distribution becomes more heterogeneous. In contrast to the empty channel case, the recorded holographic interferograms showed no clear phase boundaries but instead showed stochastic, unstructured mixing of fluid at different temperatures. Concerning heat flux, it was shown that the addition of inserts generally enhances the heat flux over the whole boiling curve, with the influence increasing at higher heat fluxes. It was shown that the effect of the inserts also increases with higher flow rates and fluid subcoolings. The linear dependence of the critical heat flux on flow rate and fluid subcooling was confirmed for the inserts as well, but the slopes of the resulting linear fits turned out to be steeper with the inserts. All the discussed effects were seen for all types of inserts, but were strongest for the single hole orifice, and thus for the insert creating the highest turbulence intensity.

The effects of the inserts on the overall and critical heat flux could mainly result from two concurrent effects: better vapor removal from the surface, resulting in less tendency of vapor blockage of the heater surface, and better supply of cold liquid from the bulk towards the heater surface through increased mixing. Both effects decrease with the flow rate, explaining the strong dependence of the inserts' effect on this parameter. A decrease in subcooling mainly affects the influence of stronger mixing, as the enthalpy difference between the bulk flow and the layer near the heater surface decreases, reducing the effects of liquid from the bulk being transported towards the heater. With regard to the periodic behavior of the vapor layer

discussed above, this means that inserts lead to smaller vapor layers, thus the wetting fronts remain more stable at higher wall superheats. Furthermore, liquid mixing is better, resulting in colder liquid near the heater and in the wetting fronts. Generally, it was shown that turbulence and secondary flows do not affect nucleation, bubble growth etc., as these take place in a layer that is isolated from these effects in the bulk flow. However, the addition of inserts provides colder liquid and lower vapor concentration near the heater surface. As the consequence, the inserts have similar effects as an increase in subcooling, leading to a potential increase in efficiency of the heat transferring equipment.

6 Fully developed film boiling

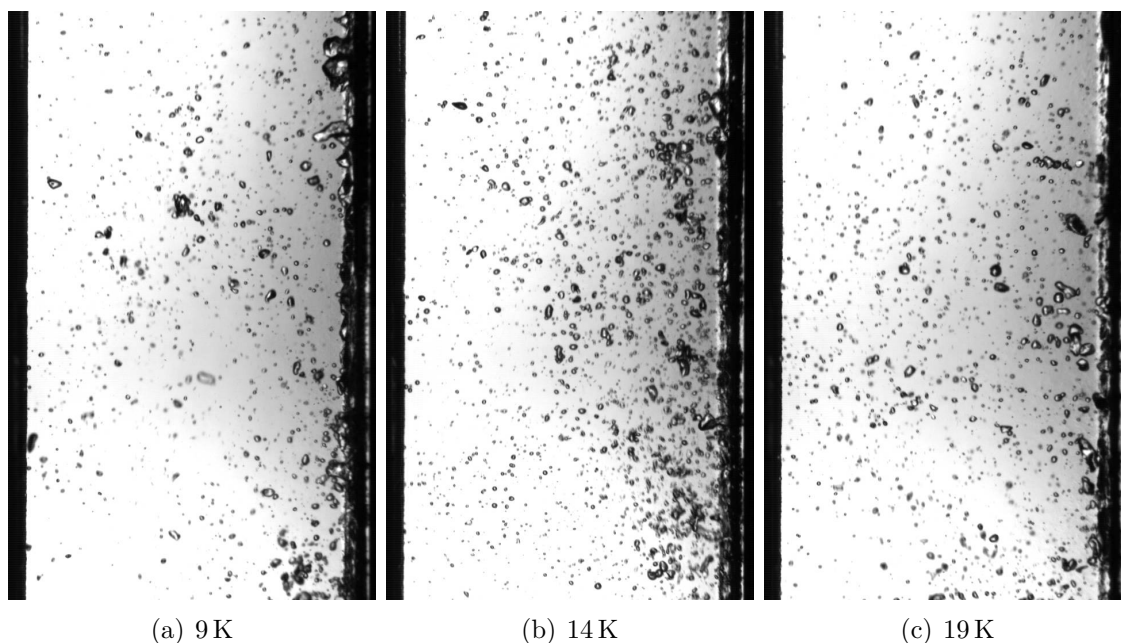
Even though the main interest in boiling studies usually lies in the processes happening up to CHF due to the higher technical importance, film boiling is also of interest for a number of applications, especially in cryogenics. Furthermore, the effects happening in fully developed film boiling can contribute in broadening the understanding of the boiling process in general, and especially of the departure from nucleate boiling, which is mainly a transient state between fully developed nucleate and film boiling. Film boiling may therefore be regarded as the upper boundary condition for the CHF transient. Therefore, the following section shall give an overview on the observed phenomena in fully developed film boiling, derived with the measurement techniques as discussed previously (see Chap. 4).

6.1 Gas distribution

To give a first overview of the regime, measurements on gas distribution were conducted in fully developed film boiling at different flow parameters. Fig. 6.1 shows photographic images of partially and fully developed film boiling at a fluid subcooling of 27 K at a flow velocity of 0.6 m/s (channel with orifice). It can be seen that the vapor is mostly concentrated in a very thin film layer close to the heater surface. Using the high-speed photographic setup with the camera positioned at 90° to the heater surface as shown in Chap. 5 for the nucleate boiling, no vapor fraction could be seen at all for the empty channel case. For the channel with the orifice, Fig. 6.2 shows the observed distributions of vapor for different subcoolings. It can be observed that the vapor is present only in a very concentrated layer close to the heater, while a small number of isolated bubbles is present in the boiling flow. The number of bubbles was observed to vary only slightly with subcooling. As the thickness of the vapor layer was too small to be measured using photographic techniques, optical probes were used to gain more detailed information. For this, analogous to the measurements shown in Fig. 5.2 and Fig. 5.15, the probes were positioned at a distance to the



Figure 6.1: Development of film boiling: partially (left) and fully (right) developed film boiling (flow boiling with orifice insert, $T_{\text{sub}}=27\text{ K}$, $v=0.6\text{ m/s}$) .



(a) 9 K

(b) 14 K

(c) 19 K

Figure 6.2: Photographs of film boiling at different subcoolings with the orifice insert ($v_s=0.6\text{ m/s}$).

heater surface of approx. 0.1 mm, and moved backwards stepwise during the experiment at otherwise steady state operating conditions. The void fractions were averaged over 1 min of measurement for each data point. Fig. 6.3 shows the measured void fractions for steady state film boiling. The measured void fractions closest to the heater were 9% for the empty channel case (round symbols in Fig. 6.3) and 31% with the orifice insert (square symbols). The probe did not enter the actual vapor film, evidenced by the low vapor fractions. This means that the film thickness was below the min-

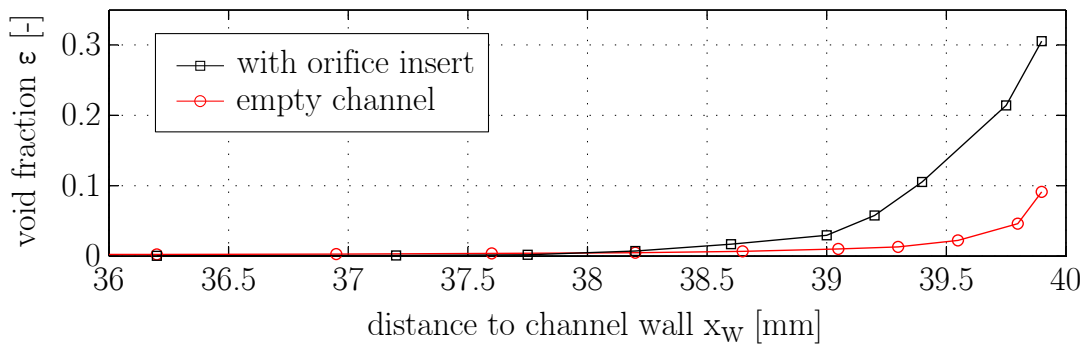


Figure 6.3: Optical Probes: distribution of the void fraction near the heated wall for fully developed film boiling ($T_{\text{sub}}=9\text{ K}$, $v_s=0.6\text{ m/s}$).

imum probe distance of 0.1 mm. Thus, the measured void fractions show the amount of smaller bubbles that were separated from the vapor film. At larger distances to the heater, slightly higher void fractions were observed for the orifice due to the stronger removal of vapor from the heater surface.

6.2 Velocity distribution in the liquid phase from PIV and HIIV

PIV and HIIV measurements were conducted to show the behavior of the liquid phase during film boiling. For the channel without added turbulence, a very homogeneous velocity distribution similar to the unheated case was observed from both PIV and HIIV. Fig. 6.4 shows histograms of the velocity distributions measured from HIIV, proving very homogeneous velocity distributions along the channel. The average vertical velocity over 350 frames was measured as 0.627 m/s. The calculated horizontal velocities were low, with mean velocities of no more than 0.01 m/s. This was in good accordance with the results from earlier PIV measurements which also gave little to no difference in velocity fields between cold flow and film boiling.

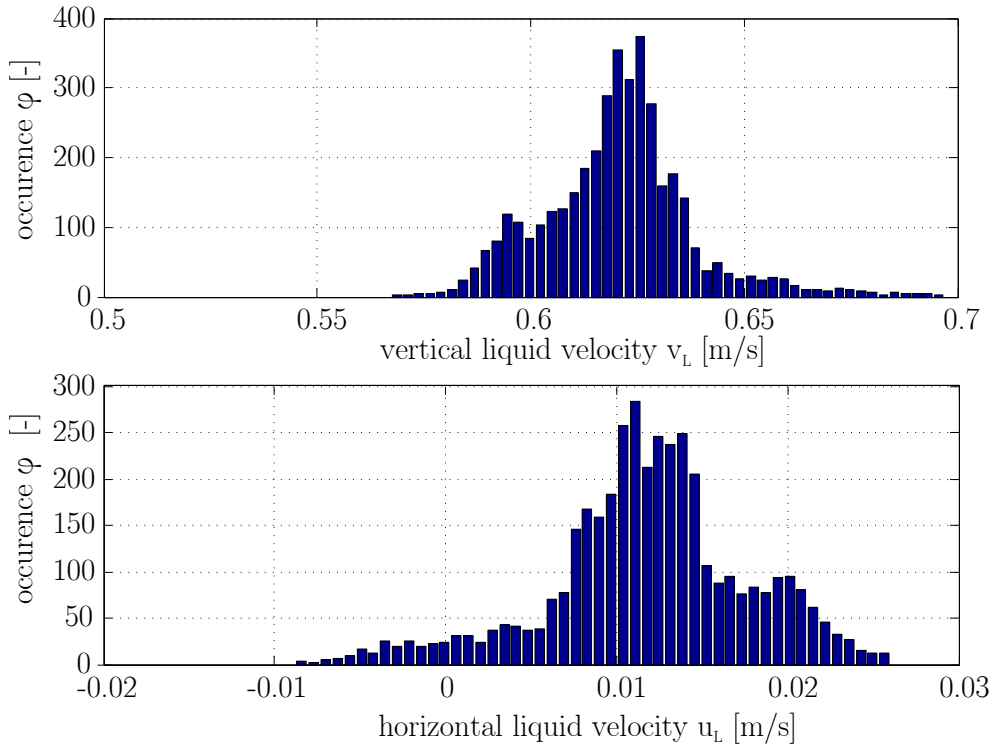


Figure 6.4: Histograms of vertical and horizontal velocities in film boiling derived from HIIV, averaged over 350 frames for channel without inserts.

6.3 Heat distribution from digital holographic interferometry

In steady state film boiling, digital holographic interferometry was used to determine the temperature distribution in the flow. As the layer of vapor on the heater surface was very thin in film boiling (≤ 0.1 mm, see Sec. 6.1), no continuous vapor phase was present in the recorded area. The holograms therefore showed only the temperature distribution in the liquid phase. Here, mainly a stratified flow of hotter liquid was observed for most experiments, reaching about 8 mm into the channel for a subcooling of 5 K. At times, larger structures or slugs of hotter liquid were observed to pass through the channel, covering nearly the entire hologram area, i.e. reaching about 23 mm deep into the channel. These slugs appeared at random intervals, with frequencies of approx. 15 Hz per second. For fluid subcoolings of 9, 14 and 27 K, similar results were obtained. Fig. 6.5 shows the two mentioned states for different subcoolings. This confirmed that in film boiling only limited transport of fluid from the bulk to the heater surface

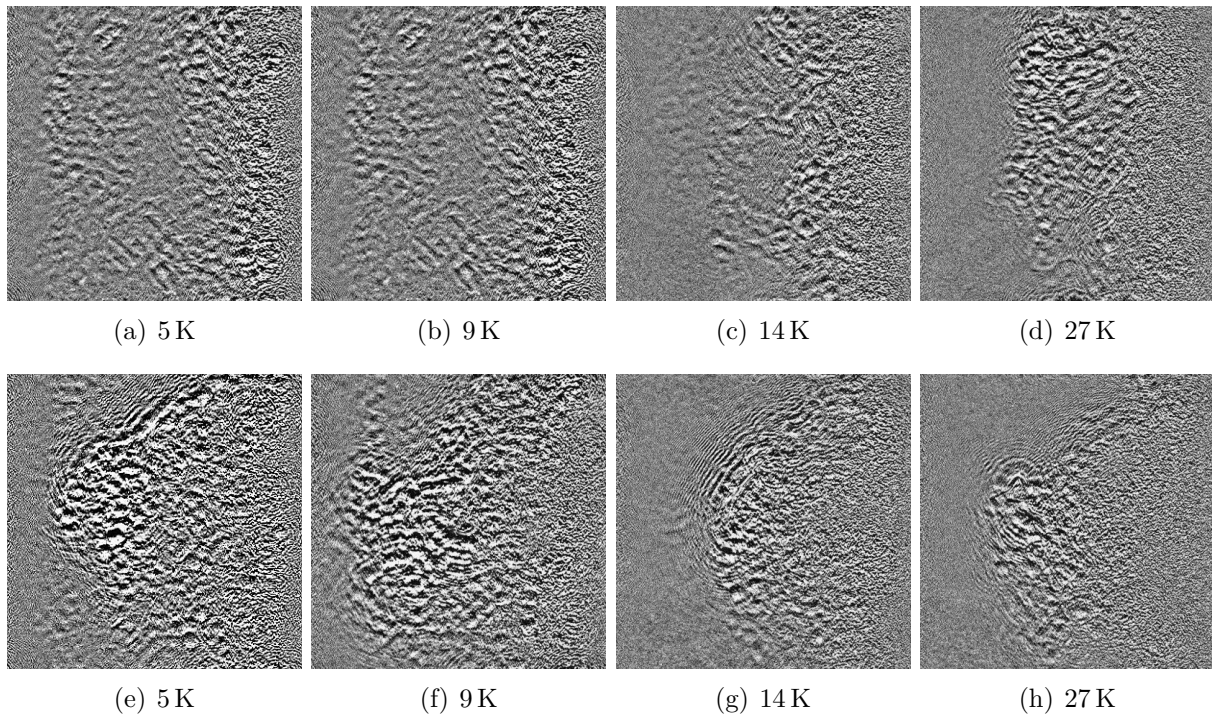


Figure 6.5: Interference phase maps of steady state film in the channel without inserts boiling at different subcoolings ($v_s=0.6$ m/s). Top row: stratified flow, bottom row: slugs of heated fluid. The heater surface is 3 mm outside the right hand border, the recorded area is 20.5×20.5 mm².

is present. The flow of hot liquid near the heater and subcooled liquid in the bulk are highly separated. The analysis of the velocity fields with HIIV showed very homogeneous velocity distributions for the whole film boiling regime. A detailed analysis of the velocities for the heated liquid slugs with HIIV showed no differences in vertical flow velocity to the surrounding liquid. This means that no measurable buoyancy effects were observed for the heated liquid slugs. Regarding the influence of subcooling on the temperature distribution in the liquid phase, it was observed that the layer of heated liquid reaches further into the channel at higher subcoolings, as seen in Fig. 6.5. For subcoolings of 9 K the structure was largely the same as discussed above for 5 K, with liquid reaching approx. 8 mm into the channel. For subcoolings of 14 and 27 K, the fluid was observed to reach 10 and 12 mm into the channel respectively. The size of heated slugs was also observed to increase with decreasing subcooling.

Experiments were also conducted on the influence of turbulence and secondary flows on film boiling. These were done using the orifice plate and

the twisted tape as discussed in Sec. 4.2). Fig. 6.6 shows the resulting interference phase maps for film boiling with the inserts at a subcooling of 27 K. In comparison to the plots shown in Fig. 6.5, a much coarser structure of the interferogram was observed, as was also shown for the nucleate boiling case in Sec. 5.4.5, indicating significantly stronger mixing of liquid within the channel. Among the two inserts, the orifice again showed a stronger influence as evidenced by the more finely distributed structure in the interferogram. This confirmed the assumptions that the addition of

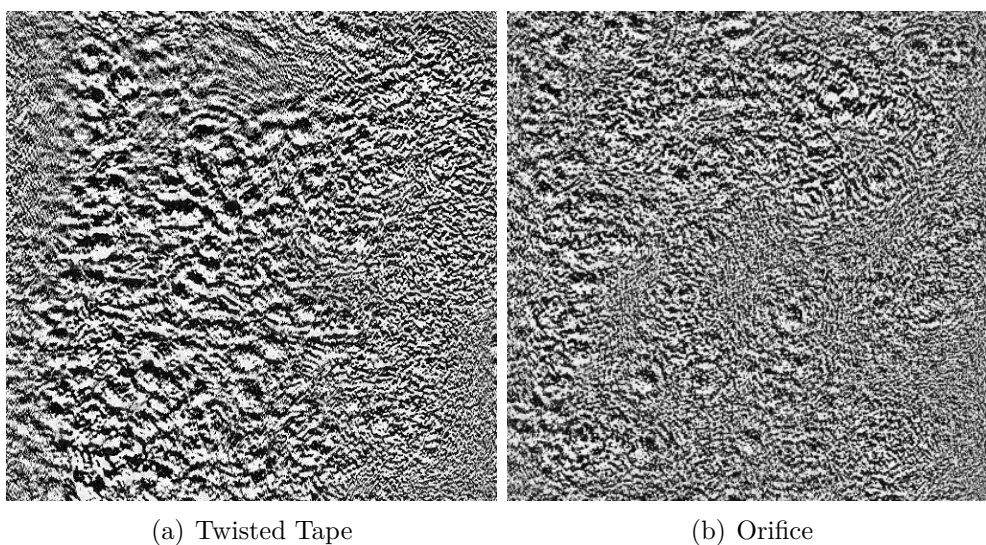


Figure 6.6: Interference phase maps showing film boiling with different flow inserts at a subcooling of 27 K and flow velocity of 0.6 m/s. The heater surface is 3 mm outside the right hand border, the recorded area is 20.5x20.5 mm².

inserts creating turbulence or secondary flows enhances mixing in the channel, thereby enhancing heat transfer. The strong mixing indicates a more uniform distribution of heat in the channel than for the case without inserts.

6.4 Summary on film boiling results

A number of interesting results concerning film boiling were shown: firstly, it was observed that the actual film layer thickness was below 0.1 mm, while single bubbles reached up to approx. 2 mm into the channel. Concerning the velocity distribution in the channel, it was shown by PIV and HIIV measurements that without flow inserts a very uniform velocity distribution

was observed, comparable to cold flow without boiling. Furthermore, concerning the temperature distribution, DHI measurements showed a strongly stratified flow regime, with warmer liquid reaching approx. 8 mm into the channel. At random intervals, slugs of warmer liquid were observed, reaching about 23 mm into the channel. With increasing subcooling, the layer of heated liquid was observed to reach further into the channel due to the larger temperature gradients. With added turbulence and/or secondary flows, enhanced mixing was observed to lead to a more uniform distribution of temperature in the channel. This also confirmed the results from Sec. 5.4 for nucleate boiling, showing the increased mixing in the liquid phase with flow inserts.

7 CHF transition

The results discussed so far were mainly focused on evaluation of the effects happening in steady-state boiling before (nucleate) and after (film) the CHF transition. Thus, the regimes forming the boundaries for this technically highly interesting phenomenon were defined. In the following chapter, a detailed description of the investigated effects during the CHF transient for various thermo-hydraulic parameters with the measuring techniques discussed in Sec. 4.3 shall be given. Subsequently, a critical comparison of the effects to the assumptions of available phenomenological models shall be given, and finally a refined mechanistic approach shall be presented. Thus, the first part of this chapter is based on general observations, while the second part focuses on the comparison to specific mechanistic models.

7.1 Gas-holdup

To give a first overview on the CHF transition, Fig. 7.1 shows photographs for the process at different fluid subcoolings. The decrease in void fraction can be clearly observed for all subcoolings.

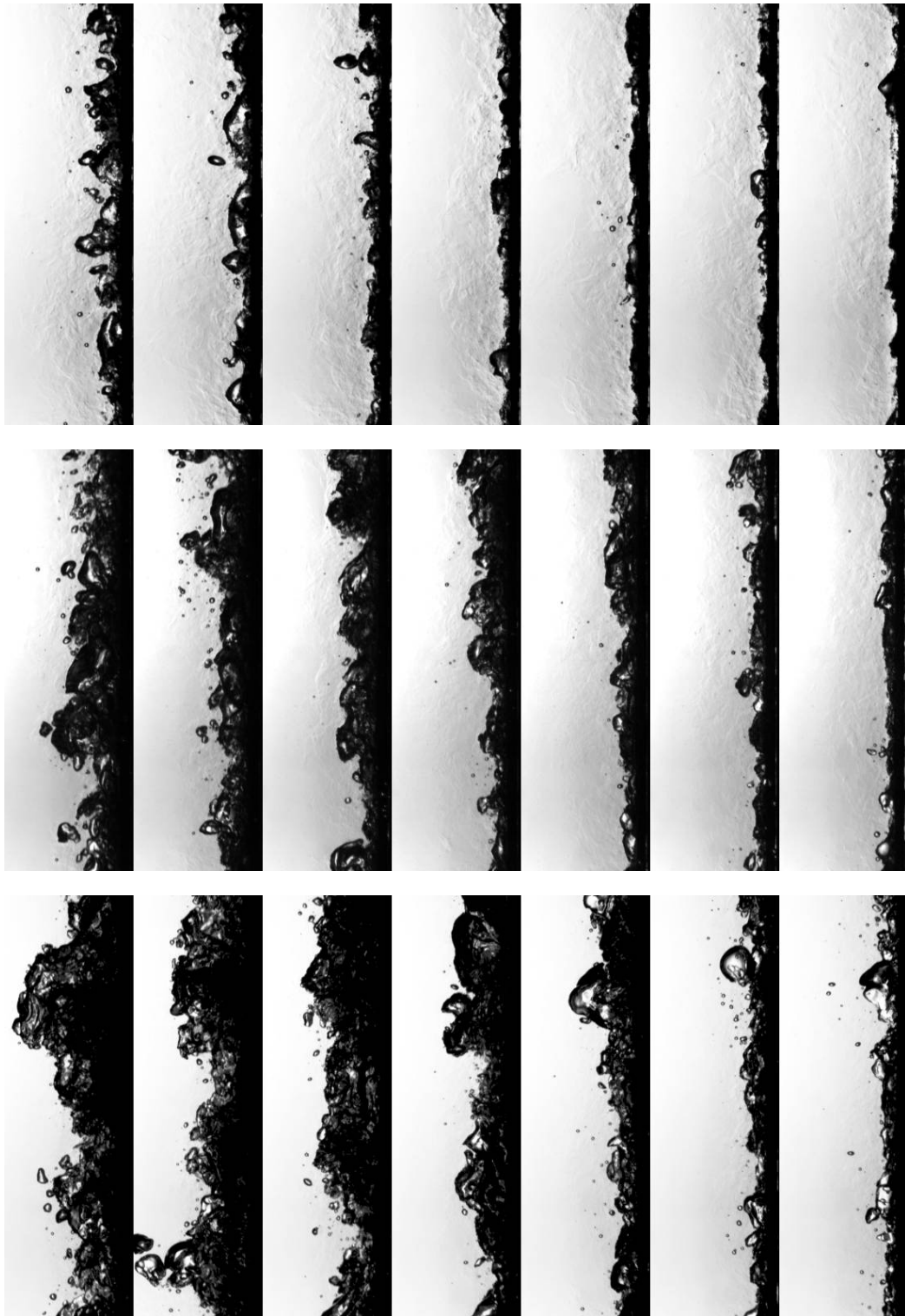


Figure 7.1: Photographic images of transition from nucleate boiling into transition boiling for subcoolings of 27, 14 and 9K (from top) at $v_s=0.6$ m/s. Duration from left to right is 17.5s for each sequence.

7.2 Frequencies of vapor agglomerations

Following the assumptions of the interfacial lift-off model, the frequency of vapor agglomerations would be expected to remain constant during transition, while a change in frequency would suggest effects such as a closing of the wetting fronts or a collapse of the wavy regime altogether. Considering the potentially strong influence of the wetting fronts discussed for the steady state experiments in Sec. 5.3, this effect is of high interest regarding the mechanisms of CHF. Therefore, the frequencies of the agglomerations were also analyzed for the transition process. Due to its transient nature, the algorithm was changed from the aforementioned FFT method to a more simple and robust peak detection algorithm. This algorithm recorded the time difference between each larger agglomeration, which was then averaged over 500 frames (1 s) for each data point. The results showed nearly constant frequencies during the transition process for all three analyzed subcoolings. The results from the optical probes gave a similar trend. Thus, the results strongly indicate that the wavy nature of the highly coalesced regime stays intact during the transition process, with only the amplitude of the waves decreasing.

7.3 Transition from holographic interferometry

Digital holographic interferometry enabled more insight into the heat distribution before and after CHF. Fig. 7.2 shows interference phase maps for the transition process at different points of time. As discussed in Sec. 5.3, before the transition wetting fronts with cold liquid were observed to occur between larger agglomerations, as can also be seen in Fig. 7.2 (a). In fully developed film boiling, a layer of heated liquid was observed reaching up to 8 mm into the channel, as can be seen in Fig. 7.2 (d). During CHF transition, a mixture of both effects was observed: while the amplitude of the vapor agglomerations became smaller towards film boiling, a layer of hotter liquid was observed above the vapor phase, see Fig. 7.2 (b) and (c). These results demonstrate the change in heat transfer taking place during the transition. While in nucleate boiling, heat is transferred mostly

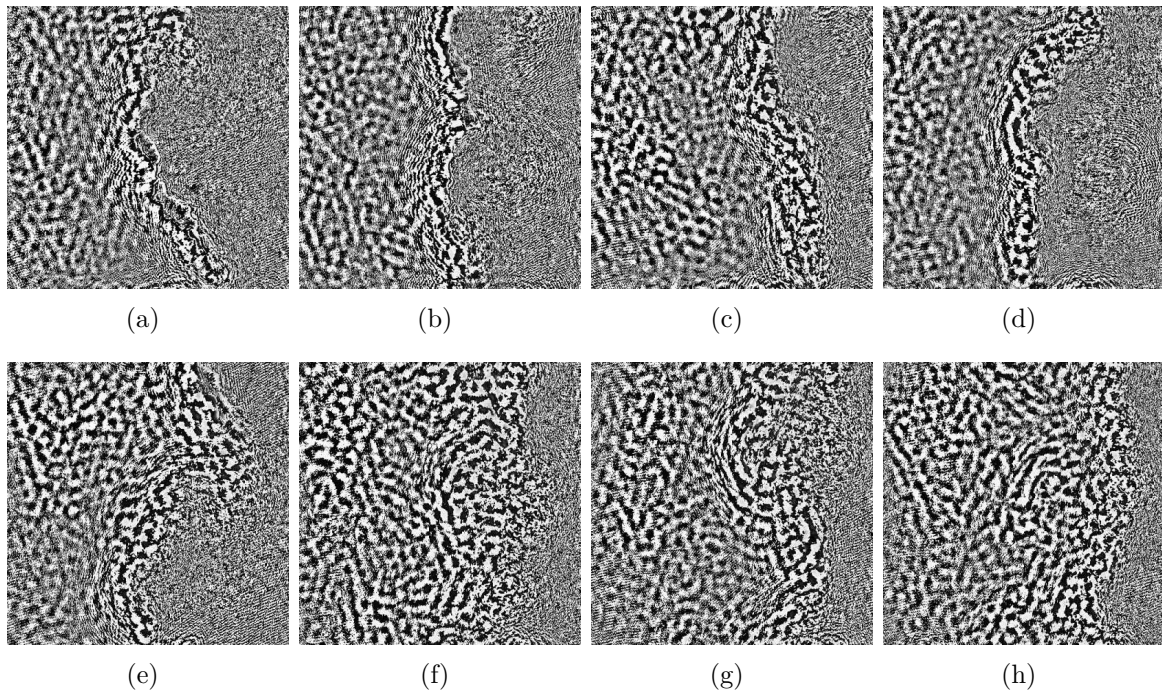


Figure 7.2: Interference phase maps for CHF transition: (a): fully developed nucleate boiling, (b)-(c): transition, (d): film boiling ($T_{sub}=5$ K, $v_s=0.6$ m/s). The heater surface is 3 mm outside the right hand border, the recorded area is 20.5×20.5 mm².

through evaporation, this changes to the conductive transfer prevalent in film boiling, which results in larger amounts of hotter liquid in the channel.

7.4 Vapor layer behavior during DNB from probe measurements

The optical enabled high-speed measurements during the CHF transition, which allowed to study the point wise behavior of the vapor layer. Fig. 7.3 shows the development of heat flux, void fraction and bubble size (contact time) plotted versus time for the CHF transient at a subcooling of 5 K for values averaged over 0.5 s. Measurements were also conducted for subcoolings of 9, 14, 19 and 27 K (results not shown). For all subcoolings, the following behavior was observed: upon reaching CHF, the probe at a distance of 6 mm from the heater surface detected decreasing vapor fraction, while two probes closer to the heater surface still showed an increasing void fraction. After passing CHF(+), the void fraction was observed to decrease steeply for all probe positions together with the heat flux. Furthermore, the average bubble contact time, which is equivalent to the bubble size, was observed to increase strongly after CHF, indicating increased coalescence of bubbles in the vapor layer. Furthermore, a FFT analysis of the probe signals showed the overall frequency of the vapor layer to increase by a factor of 40 to 100 % during the transition, indicating a significant increase in vapor velocity.

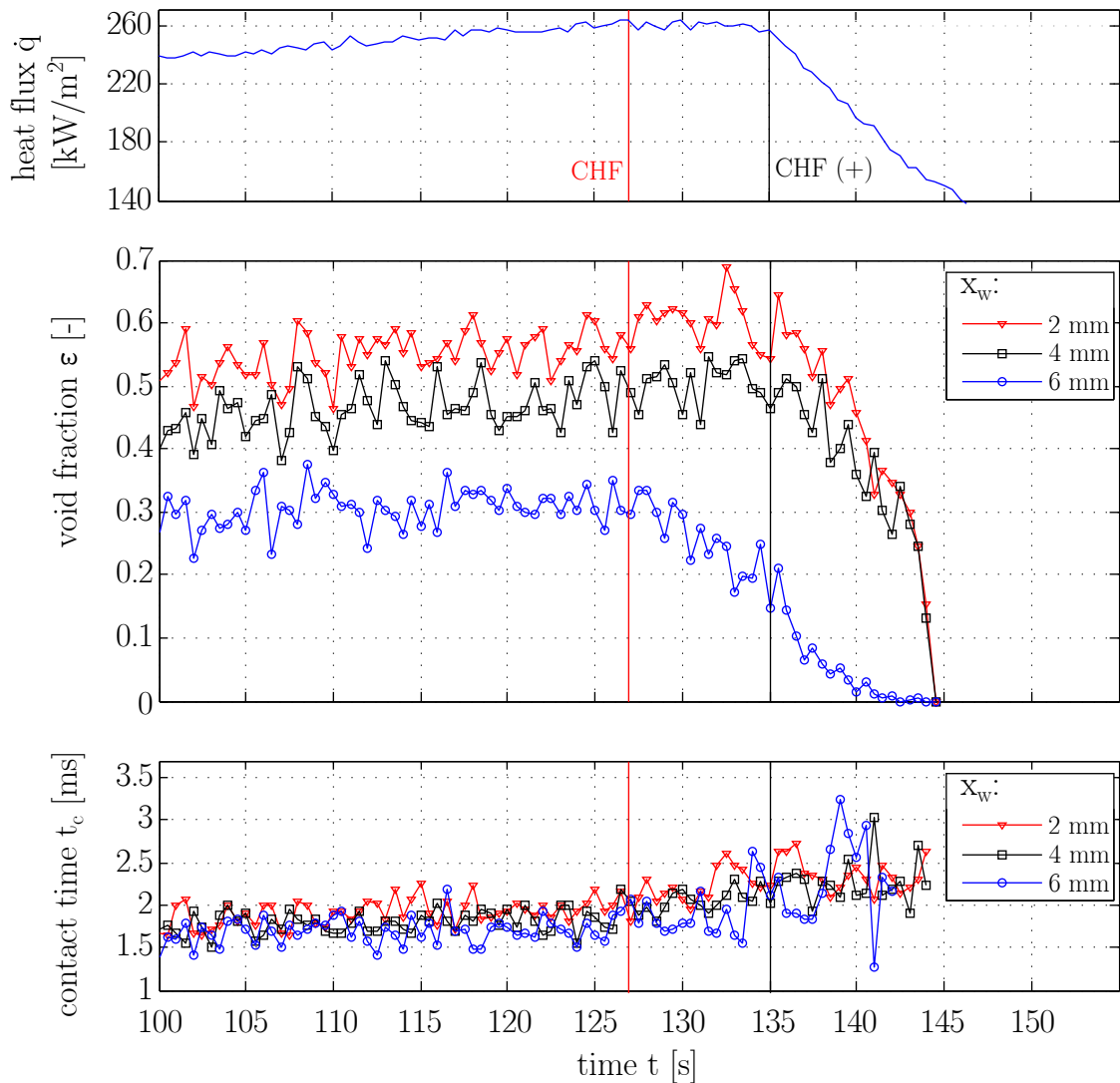


Figure 7.3: Development of the heat flux, the void fractions and bubble sizes/contact times over time for the CHF transient at 5K subcooling. The void fractions and the contact times were measured with optical probes at different distances from the heater surface x_w . The time scale gives the overall time from beginning of the experiment with a cold heater ($v_s=0.6$ m/s).

7.5 Summary on the CHF transition

Summarizing, the following statements can be made concerning CHF/DNB in the studied geometry: The heat fluxes were observed to decrease only slowly at first after reaching the maximum heat flux (CHF), and decreased steeply several seconds later, at a point denoted as CHF(+). Both holographic interferometry and HS photography showed a decrease of the overall gas holdup at CHF. The agglomerations were observed to decrease in size to-

gether with the overall vapor layer, while the frequencies remained constant over the transition. The optical probes showed a more detailed behavior of the vapor layer during CHF: with three probes mounted at distances of 2, 4 and 6 mm from the heater surface, the vapor fraction was observed to decrease at the 6 mm position at CHF, while still increasing at the two other positions. At the same time, the average size of the bubbles was observed to increase at all probe positions together with an increase in the overall frequency of the vapor layer, indicating more bubble coalescence and a higher velocity. Finally, upon reaching CHF(+), the vapor fraction also decreased at the other positions, showing the actual transition into film boiling. This behavior could be interpreted as a saturation of the vapor layer close to the wall, especially of the wetting fronts present between the agglomerations, with vapor bubbles upon reaching CHF. The bubbles begin to show significant coalescence at CHF, leading to an insulation of the heater surface. In the following section, the mentioned mechanisms shall be discussed in further detail and be compared to the available mechanistic models presented in Chap. 2.

8 Critical review of the results, formulation of a new modeling approach

In the following section, CHF trigger mechanisms proposed by the mechanistic models discussed in Sec. 2.3 are critically reviewed with reference to the experimental results. Furthermore, the experimentally derived phenomena discussed in the previous chapters are reviewed with special regard to the validation of the mechanistic models, and a concept for a new phenomenological approach is presented. Significant parts of this chapter were also previously published by the author in [16].

8.1 Bubble crowding model

As turbulent interchange is one of the main mechanisms of the bubble crowding model, experiments were conducted on the actual influence of the turbulent flow on the vapor interface and the critical heat flux (see Sec. 5.4). To study this, boiling experiments were conducted with varying degrees of turbulence and secondary flows using an orifice placed at the inlet of the boiling chamber. It was observed that increasing turbulence lead to a better distribution of the vapor and therefore to a thinner vapor layer in the proximity of the heater surface. Studying this influence statistically at different fluid subcoolings yielded the results shown in Fig. 8.1. The figure shows the averaged intensity per pixel column for a total of 17,000 images for each curve. It was observed that the penetration depth of turbulence regarding the vapor, i.e. the difference in vapor layer thickness was approximately constant for the orifice at the studied subcoolings. Taking the difference at 90 % void fraction, a reduction of 1.2, 1.3 and 1.5 mm in thickness was observed at subcoolings of 9, 14 and 19 K respectively. This was equivalent to 17, 21 and 31 relative reduction. Comparing this to the observed increases in CHF yielded good agreement, as CHF increase was observed at 19, 23 and 25 % for subcoolings of 9, 14 and 19 K respectively (see Tab. 5.4). While this does not fully confirm the assumptions of the

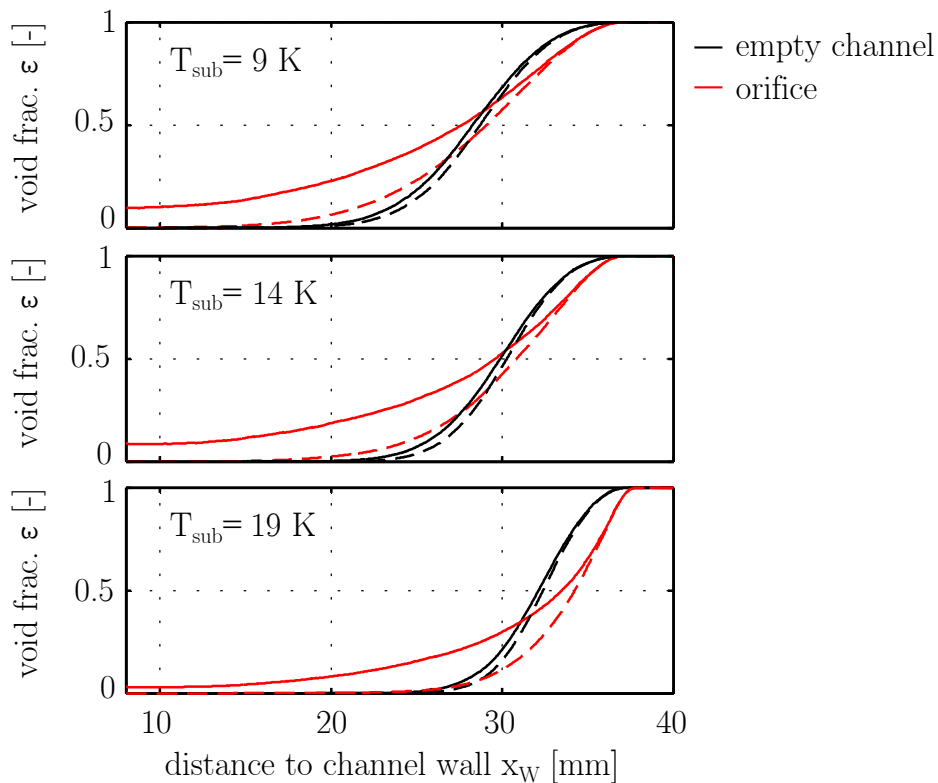


Figure 8.1: Vapor layer distribution over the channel cross section at CHF(-) for the reference case (empty channel, black lines) and case with added turbulence by orifice (red lines) at different subcoolings. Dashed lines indicate values after numerical removal of isolated bubbles. The heater surface is at the right hand side, at 40 mm.

model concerning a linear influence of turbulence intensity as would be considered from Eq. (2.6), it does confirm that there appears to be a critical vapor thickness for given thermohydraulic parameters. The reduction of this thickness results in an increase in CHF equivalent to the reduction of the vapor layer. However, considering the idea of vapor blockage as a mechanism causing DNB, it would be assumed that for given subcooling and bulk flow rate, CHF should always occur at the same vapor layer thickness. Considering Eq. (2.4), when the bulk turbulence is increased it would further be assumed that a higher vapor layer thickness should be possible to be supported before CHF takes place. Comparing these assumptions to the results shown above, where added turbulence increased the CHF, while the vapor layer thickness at CHF decreased resulted in the assumption that the critical parameter is not the thickness of the overall vapor layer, but rather a smaller region closer to the heater. This assumption was further

substantiated by conducting measurements with optical probes. For these measurements, the system was run in steady state boiling at CHF(-), and the probes were moved backwards from the heater starting at a distance of 0.1 mm. Fig. 8.2 gives a detailed view of the probe measurements given in Fig. 5.15, showing the distribution of void fraction for the reference case (empty channel without inserts) and the orifice over the distance to the heater surface for a subcooling of 9 K. While for distances further away from the heater (35-38 mm) the curves were even further apart than the ones calculated from photography, the values close to the heater surface at 0.1 mm, differed by only 8.7%, corresponding to approximately half the reduction seen for the overall vapor layer. This again confirmed the assumption of a sublayer existing beneath the main vapor layer that is less affected by bulk flow turbulence. As a short recapitulation, the following summary

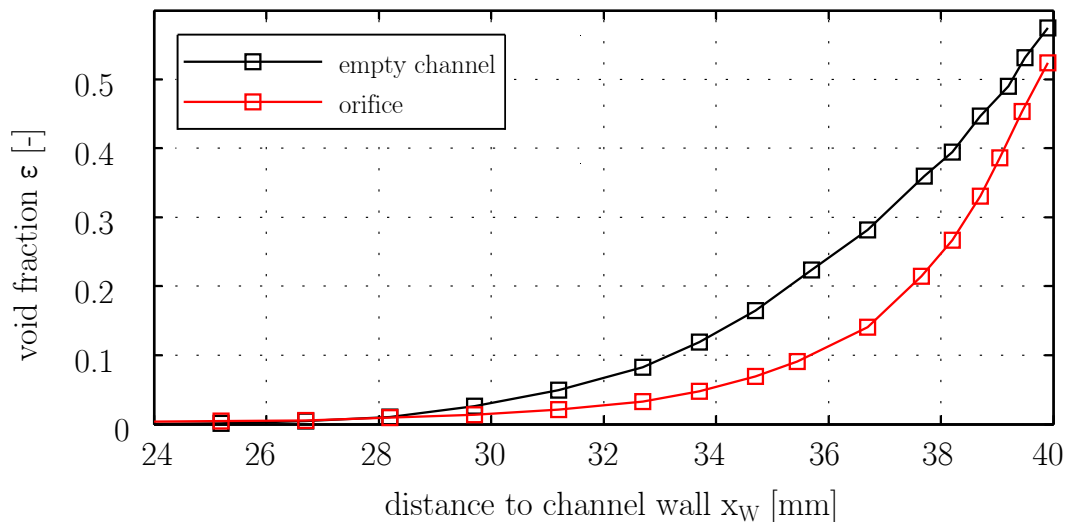


Figure 8.2: Measurement of void fractions from optical probes ($T_{sub}=9$ K and $v_s=0.6$ m/s).

shall be given for effects concerning the bubble crowding mechanism:

1. The 82% void fraction as criterion for CHF do not appear reasonable, as probe measurements close to the heater have shown much lower void fractions. This has been reported as one of the major weaknesses of the model in a number of reports before [28, 91, 139].
2. Added turbulence reduces the overall vapor layer by a constant penetration depth.

3. As this value is constant, the relative influence of added turbulence decreases with subcooling as vapor layer thickness increases. This was in good accordance with the results shown in Sec. 5.4.2.
4. The reduction of the overall vapor layer thickness leads to better access of liquid to the relevant bubbly sublayer, increasing CHF by a similar factor as the relative reduction of the vapor layer thickness.
5. Added bulk flow turbulence has less influence on the layer relevant to DNB. This is also evidenced by the constant frequencies of agglomerations for various flow inserts, subcoolings etc. as shown in Sec. 5.4.3.
6. This also suggests that the two-phase enhancement factor used for calculation of the turbulent interchange (see Eq. (2.2)) is not correctly formulated as the vapor layer actually blocks bulk flow turbulence, and does not enhance it.
7. The actual CHF trigger parameter is not the thickness or concentration in the overall vapor layer, but rather an effect in the relevant bubbly sublayer. However, reducing the vapor layer by turbulence (or subcooling) delays this effect.
8. The use of Prandtl mixing theorem as location of bubbly/bulk interface does not seem appropriate as turbulent interchange is expected to be blocked by the vapor layer before actually reaching the relevant sublayer.
9. Finally, a coupling of the model with a viable description of the periodic vapor structure is necessary with the aim of defining the relevant sublayer by analysis of areas of lower vapor concentration.

8.2 Sublayer dryout model

The mechanisms presented in the sublayer dryout model are generally difficult to investigate experimentally. To access the actual sublayer in regions of several μm to the heater surface, optical probes of smaller diameters and with a very precise positioning mechanism should be applied. However, some insight could also be given with the applied techniques. With the

used optical probes, measurements up to 0.1 mm distance to the heater surface were possible. The measured void fractions given above in Fig. 8.2 show no significant change in void as the probes reach the heater. Therefore, at least in regions of 0.1 mm up to the heater surface, no liquid sublayer could be detected. The equivalent diameter of the vapor cylinders is assumed to be equal to the departure diameter of bubbles under the respective thermal hydraulic conditions, and is expected to stay constant [91]. Considering this mechanism, even as the actual liquid sublayer is not accessible with the available techniques, it should be possible to detect the vapor cylinders close to the heater surface. In Fig. 7.3, the behavior during CHF at a 5 K subcooling measured with optical probes was shown. For a subcooling of 9 K, the same measurement is shown in Fig. 8.3, giving similar results. In the

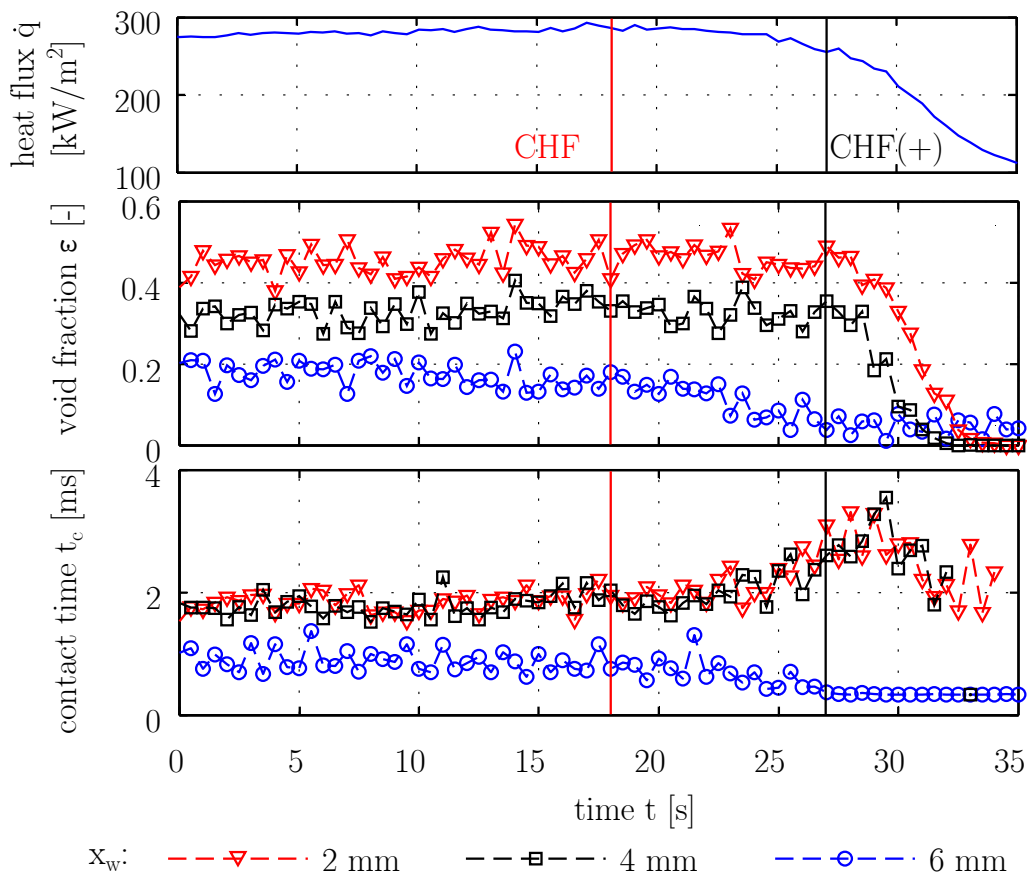


Figure 8.3: Development of the heat flux, the void fractions and bubble sizes/contact times over time for the CHF transient at 9 K subcooling. The void fractions and the contact times were measured with optical probes at different distances from the heater surface x_w ($v_s=0.6$ m/s).

lower plot of Fig. 8.3, the bubble contact time at the probes is given, which represents the bubble size. It was observed that after passing CHF(+), the

measured contact times at the 2 mm and 4 mm positions started to grow significantly, increasing from a mean value of approx. 2 ms up to 3 ms. At the lower subcooling given in Fig. 7.3, the same behavior was also observed for the 6 mm position, indicating a thinner relevant bubbly sublayer at higher subcoolings. This behavior could be interpreted as the formation of larger vapor bubbles or blankets in the direct vicinity of the heater surface. As this behavior directly precedes the abrupt breakdown of the vapor layer (see middle plot in Fig. 8.3) and the associated decrease in heat flux, it can be assumed that the formation of these larger bubbles is actually part of the CHF trigger mechanism. Taking into account that the effects reach up to the position of the second optical probe at 4 mm from the heater surface for the given subcooling, the bubbles can be expected to stretch at least 2 mm in the radial direction. An extrapolation of the vapor velocity from the photographic measurements shown in Sec. 5.2.1 (see Fig. 5.3) gave an estimate of about 1.5 m/s near the heater surface. This would yield bubble lengths of 4.8 mm for the maximum contact times of 3.2 ms. Comparing this to the critical Helmholtz wavelength as calculated by Eq. (2.10) yields good agreement, with L_m calculated as 4.9 mm for this estimation. It remains somewhat unclear from these measurements how the velocity in the bubbly layer actually develops during the CHF transient. Considering the distinctive velocity gradient towards the heater surface shown in Sec. 5.2.1 and the increase in bubble size shown in Fig. 8.3 and Fig. 7.3 however, it has to be assumed that the velocity increase near the heater is significant. Following the results discussed in Sec. 8.1 for the bubble crowding model, the formation of larger bubbles shown here supports the assumption of relevant effects taking place in a bubbly sublayer close to the heater surface.

8.3 Interfacial lift-off model

As discussed in Chap. 5, in regions close to CHF a periodic behavior of the vapor layer was observed, with the appearance of larger vapor agglomerations leading to a flow regime denoted as highly coalesced regime. Such effects were not taken into consideration in the two models discussed above, but form some of the basic assumptions of the interfacial lift-off model. Using the measured vapor velocities close to the heater surface as estimate for the vapor velocity \bar{U}_g , a comparison of the wavelength λ_{cr} as given in

Eq. (2.12) to the wavelengths experimentally observed yielded good agreement. Also, the ratio of the wetting front length in comparison to the total vapor wavelength, given as 0.2 by Sturgis and Mudawar [121, 122] (see also Eq. (2.14)) could be confirmed from the photographic studies discussed in Chap. 5. Furthermore, digital holographic interferometry showed that sub-cooled liquid is present between larger vapor agglomerations (see Fig. 5.9), supporting the assumption of a quenching mechanism relying on the so called wetting fronts, or vapor gaps. Different observations were made during an analysis of the dynamic behavior of vapor agglomerations. Here, it could be observed from the high-speed photography that the shape and structure of the agglomerations hardly remained constant while propagating along the channel. Ongoing coalescence as well as breakup and motion perpendicular to the bulk flow direction led to a constant variation of the agglomeration's overall structure. As shown in Sec. 5.3.6 (see Fig. 5.10), for vapor agglomerations moving upwards along the heater surface, vapor from the lower third of the agglomerations is transported towards the heater surface due to velocity gradients perpendicular to the flow direction. These results disagree with the model assumptions given by Galloway and Mudawar [52] for the description of the wavy vapor layer leading to the formulation of the interfacial lift-off model. In the model, a constant vapor layer is assumed at CHF(-), moving at a fixed wave propagation speed. It can be assumed that the narrow channel (depth of 6.4 mm in [52] and 5 mm in later publications [55, 86, 88, 122, 139]) used in the experiments defining this model does not allow for the formation of a velocity gradient perpendicular to the heated surface, resulting in a rather constant wavy layer. Most likely, the descriptions for the interfacial lift-off can not directly be applied to larger scale channels. While the general structure may appear similar, the periodic vapor behavior is more strongly governed by the behavior of the larger agglomerations. It can be assumed that the increased buoyancy has a strong effect on the vapor behavior, leading to discrepancies with the model's assumptions. This will be discussed in more detail in Sec. 8.4.1. Using the optical probes, further studies were conducted on the applicability of the interface lift-off as DNB trigger mechanism for the geometry used here. Placing probes at fixed distances of 2, 4 and 6 mm above the heater surface at the trailing edge, following the assumptions of the model, an increase in void fraction at all probe positions would be expected as the interface lifts off shortly prior to CHF. Fig. 7.3 and Fig. 8.3 show the

results of these measurement at inlet subcoolings of 5 and 9 K. Instead of an increase at all probe positions, at CHF a decrease of void fraction was observed only for the 6 mm probe. The other probes however measured an ongoing increase in void fraction, accompanied by an increase in bubble size and frequency. This describes a contraction of the vapor layer accompanied by an increase in vapor velocity, rather than a lifting of an otherwise intact wavy interface. These results were also obtained for other subcoolings [7], with flow inserts and the empty channel and also at higher mass fluxes of up to 2000 kg/m² s. Summarizing, the following statements could be made concerning the use of the interfacial lift-off model:

1. The periodic behavior is taken into consideration, but the larger diameter of the channel used in the current study leads to increased influence of larger scale coalescence and effects due to larger vapor agglomerations.
2. Therefore, a velocity gradient and involved acceleration perpendicular to the heater surface are observed that are not considered in the model so far.
3. The actual trigger mechanism of the lift-off of the vapor interface was not observed in the experiments.
4. Rather a critical drift flux appears to be leading to a critical void fraction in the bubbly sublayer, which finally breaks down the turbulent interchange with the bulk flow.

8.4 Conceptualization of a refined phenomenological model

While photographic studies support the findings concerning the periodic behavior of vapor layer as given by Mudawar et al. for the interfacial lift-off model, the results received from the optical probes contradict the actual lift-off mechanism. However, the increase of void fraction closer to the heater at CHF suggests a mechanism similar to the near wall bubble crowding model, brought on by an additional increase in void velocity. The discussed results also appear to hold for cases with added turbulence as shown in [10].

Following these points, a refined phenomenological approach is suggested as a combination of available mechanistic models. The following sections describe the assumptions being made for the new model and present a refined phenomenological concept.

8.4.1 Drift-flux gradient and lift-force in the vapor phase

An important aspect which seems to have gotten too little attention in the previous models is the velocity of the vapor interface. As shown in Fig. 5.2, a strong velocity gradient towards the heater surface is present. This suggests significant influence of the added buoyancy and swarm effects within the agglomerated structures affecting the vapor layer. It has to be noted that the velocity close to the heater surface was almost twice as high as the liquid bulk flow velocity. As seen in Fig. 5.10, this leads to the transportation of vapor from the trailing edge of agglomerations towards heater surface. This behavior is considered to be crucial regarding the effects leading up to CHF. The observed behavior can be attributed to a number of phenomena: first, the increased vapor fraction towards the heater, as seen in figures 8.2 and 5.2, causes an increase of the velocity difference between the vapor phases. Using a drift-flux approach and calculating the slip velocity using the expression given by Chisholm [38, 39] from the void fractions measured with the optical probes as shown in Fig. 8.2 yields a velocity distribution as shown in Fig. 8.4. It can be observed that, while fitting the general

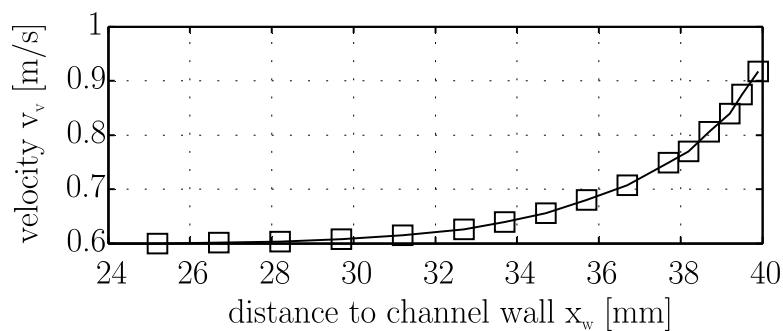


Figure 8.4: Slip velocity calculated by Chisholms correlation.

observations on the vapor velocity, the curves as calculated by Chisholms correlation show slightly lower values than measured from the high-speed photographs. This indicates that in addition to the higher void, swarm effects in the vapor layer lead to a decrease of drag and therefore a higher

velocity as was shown e.g. by Roghair et al. [114]. Furthermore, the motion of large vapor structures towards the heater surface can be explained taking into consideration the lift-force acting on the vapor phase. The velocity gradient discussed above constitutes a shear flow. It has been shown experimentally by Tomiyama et al. [125] and numerically by Bothe et al. [18] that the direction of the lift force for single bubbles reverts after a critical diameter is exceeded (around 5 mm for water). Both authors have shown that the lift force for larger bubbles generally points in the direction of the higher surrounding velocity, which in the present case explains the motion towards the heater surface.

8.4.2 Refined phenomenological approach

The critical comparison of the experimental results to available mechanistic models given in the three previous sections confirmed some of the assumptions given for the bubble crowding model and the interfacial lift-off model concerning turbulent interchange and vapor behavior respectively. The trigger mechanism proposed for the interfacial lift-off model could not be confirmed in the present results. The bubble crowding mechanism still appears viable, but the result showed a definite need for an expansion of the model to also take coalescence induced effects into consideration. Also, experiments with varying turbulence showed that vapor layer thickness itself is not a viable CHF trigger. It was shown that nearing CHF, the bubble size also increased considerably in the layer below 4 mm from the heater surface, with an estimation confirming the observed bubble sizes to fit the assumptions for the vapor plumes given for the sublayer dryout model. All these points led to the assumption that the actual CHF trigger mechanism can indeed be found in a sublayer close to the heater, as suggested by the bubble crowding and sublayer dryout models. Furthermore, measurements from optical probes, PIV and high-speed photography allowed to give an estimate of drift-flux or slip velocity in the vapor phase towards the heater. It was concluded that this creates a lift force acting towards the heater surface for larger vapor structures. Finally, a concept for an enhanced phenomenological model was developed taking into consideration the new observations. Fig. 8.5 shows the basic assumptions being made for the new model. A vapor layer consisting of two general layers, shown as coalesced layer in gray

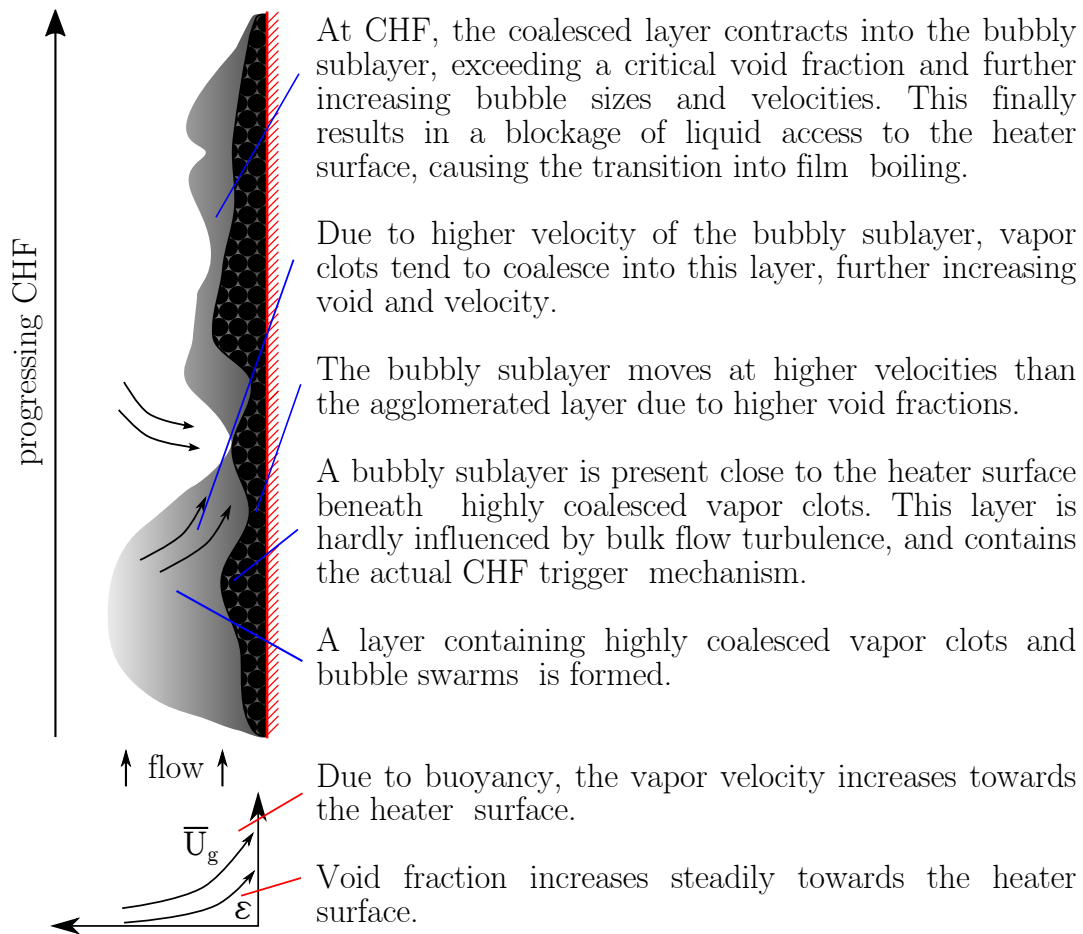


Figure 8.5: Proposed new mechanisms for CHF transition as supported by the presented experimental results.

and bubbly sublayer in black are assumed. The coalesced layer reaches far into the channel and forms agglomerations and larger coalesced structures. The smaller bubbly sublayer is present in the direct vicinity of the heater surface, i.e. approx. 2-4 mm for the present system. There is no distinct boundary between the two layers, but for practical reasons the two are discussed as separate phenomena. A velocity gradient is assumed between the outer edges of the coalesced layer and the bubbly sublayer closer to the heater surface. While at the outer edges approximately bulk liquid speed is assumed, closer to the heater the velocity reaches twice that value. The velocity difference leads to vapor from the coalesced layer being moved into the bubbly sublayer, further increasing the velocity and void fraction. At DNB, a critical velocity in the sublayer is reached that leads to a crowding mechanism close to the heater, which prevents liquid access from the heater surface. This finally leads to dryout under larger vapor structures.

This causes an increase in heater surface temperature above the Leidenfrost point, thus marking the start of transition boiling.

9 Summary and conclusions

To improve the understanding of the physical phenomena governing subcooled flow boiling, an extensive experimental study was conducted. An emphasis of the study was on the development and improvement of measuring techniques. Optical microprobes were developed for measurement of local parameters, a digital holographic interferometer was designed for the visualization of density gradients in boiling flows. Furthermore, a technique for the determination of velocity fields (HIIV) was developed based on holographic interferometry that allowed the detection of velocity fields in turbulent flows without the need for tracer particles. In addition to these techniques, particle image velocimetry and high-speed photography were applied to detect velocity fields, gas distributions, bubble sizes etc. For all techniques, algorithms for automated analysis were developed. Using these techniques, boiling experiments were conducted in a vertical, rectangular channel with one heated wall in subcooled flow at differing flow rates and fluid subcoolings over the entire boiling curve. 3M Novec 649, a low boiling carbohydrate was used as working liquid, making boiling regimes up to fully developed film boiling accessible. Turbulence and secondary flows were added through different flow inserts at the channel inlet. The wide range of measuring techniques employed allowed to create a wide data base of heat fluxes, vapor and temperature distributions and the motion of both phases. Measurements of turbulence intensity and vorticity in cold flow showed the penetration depths of the inserts. These were shown to be significantly higher for inserts creating longitudinal vortices than for perforated plate type inserts creating near isotropic turbulence.

Boiling experiments showed that the use of flow inserts can strongly enhance the overall heat flux in boiling processes, yielding increases in critical heat flux of up to 90 percent in comparison to experiments at identical conditions without inserts. The influence of the inserts was shown to be highest at high flow rates and fluid subcoolings, while at low subcoolings and flow rates the effects were negligible. The highest increase in heat flux was observed for a single hole orifice with a porosity of 0.3, which also showed the highest turbulence intensity among the examined plates. The effects could

be shown to be mainly due to better mixing and vapor removal in the channel, resulting in more subcooled liquid being transported towards the heater surface. At lower subcoolings, the larger thickness of the vapor layer limits the accessibility of the heater surface to turbulence effects, and the smaller difference in enthalpy between the bulk liquid and the liquid near the heater surface reduces the effect of liquid from the bulk being transported towards the heater.

Special regard was also given to measurements close to and during the critical heat flux transition, with the aim of adding deeper insight into the phenomenology of the mechanisms triggering the departure from nucleate boiling. The results showed larger slug-like vapor agglomerations appearing near the heater surface at constant frequencies, independently of fluid subcooling and inserts. PIV and HPIV measurements of the velocity fields around such agglomerations showed a significant increase of fluid velocity towards the heater surface in the wakes of agglomerations as well as in the gaps between subsequent agglomerations. Holographic interferometry revealed the liquid in the gaps to be at approximately the same subcooling as the bulk flow, confirming the importance of these wetting fronts for the heat transfer in regimes close to CHF.

A critical comparison of the observed phenomena with available mechanistic models on flow boiling CHF revealed some shortcomings of the available models. Following this, a concept for a refined phenomenological approach was proposed.

Supervised theses

Im Rahmen dieser Dissertation entstanden am Lehrstuhl für Thermodynamik in den Jahren 2010 bis 2013 unter wesentlicher wissenschaftlicher, fachlicher und inhaltlicher Anleitung des Autors die im Folgenden aufgeführten studentischen Arbeiten. In ihnen wurden verschiedene Fragestellungen zu Messtechnikentwicklung sowie zu Durchführung und Auswertung von Siedeexperimenten untersucht. Alle Arbeiten wurden in deutscher Sprache verfasst. Ergebnisse aus diesen Arbeiten können in Teilen in das vorliegende Dokument eingeflossen sein. Der Autor dankt hiermit nochmals explizit allen ehemals betreuten Studenten für ihr Engagement bei der Unterstützung dieser wissenschaftlichen Arbeit.

Associated with this Ph.D. thesis are a number of “student theses” (Semesterarbeiten, Diplomarbeiten, Bachelor theses or Master theses) that were supervised by the author of the present work. These theses were prepared at the Lehrstuhl für Thermodynamik in the years 2010 through 2013 under the close supervision of the present author in its full academical and professional breadth. Various issues were investigated concerning development of measuring techniques as well as the conduction and evaluation of boiling experiments. All theses were written in German. Some parts of those supervised theses may have been incorporated into the present thesis. The author would like to express his sincere gratitude to all formerly supervised students for their commitment supporting this research project.

Student	Thesis
Thomas Koller	<i>Konstruktion eines Fluidkreislaufs zur Durchführung von Siedeexperimenten</i> , Semesterarbeit, filed in July 26th, 2010.
Paul Heinz	<i>Einsatz der digitalen Holographie zur Untersuchung von Mehrphasenströmungen</i> , Bachelor thesis, filed in July 26th, 2010.

- Manuel Schöberl *Inbetriebnahme eines Vorversuchsstands und Durchführung von Siedeeperimenten zur Charakterisierung niedrigsiedender Kältemittel*, Semesterarbeit, filed in August 11th, 2010.
- Denise Schmitt *Inbetriebnahme eines Versuchsstands und Durchführung von Experimenten zum Einfluss von Turbulenzen auf das unterkühlte Strömungssieden*, Diplomarbeit, filed in May 30th, 2011.
- Florian Höfer *Auslegung und Konstruktion von Turbulenz- und Drallerzeugern zum Einsatz bei Siedeversuchen*, Semesterarbeit, filed in September 16th, 2011.
- Tobias Schechtl *Einsatz der Particle Image Velocimetry (PIV) zur Untersuchung von Turbulenz- und Drallerzeugern zum Einsatz bei Siedeversuchen*, Bachelor thesis, filed in October 12th, 2011.
- Christina Jochum *Untersuchungen zum Einfluss von Turbulenzen und Sekundärströmungen auf Wärmeübergang und kritische Wärmestromdichte beim Strömungssieden*, Diplomarbeit, filed in October 10th, 2011.
- Sergej Götz *Anwendung der digitalen Holografie zur Untersuchung adiabater Zweiphasenströmungen*, Semesterarbeit, filed in December 12th, 2011.
- Gudrun Heideker *Anwendung digitaler Holografie in Siedevorgängen*, Semesterarbeit, filed in December 12th, 2011.
- Katrin Finke *Konstruktion einer optischen Nadelsonde zum Einsatz bei Siedeversuchen*, Semesterarbeit, filed in January 17th, 2012.
- Moritz Bruder *Untersuchung der Strömungseigenschaften bei Siedeeperimenten unter Einfluss von Sekundärströmungen mittels Particle Image Velocimetry (PIV)*, Bachelor thesis, filed in February 20th, 2012.

Jürgen Loth	<i>Experimentelle Untersuchungen zur Entwicklung von Wärmeübergang und Dampfgehaltsprofilen beim unterkühlten Strömungssieden unter Einfluss von Turbulenz und Sekundärströmungen</i> , Diplomarbeit, filed in February 29th, 2012.
Marine Ilg	<i>Konstruktion von Messzellen zum unterkühlten Strömungssieden</i> , Semesterarbeit, filed in March 30th, 2012.
Johannes Elfner	<i>Entwicklung und Inbetriebnahme einer optischen Nadelsonde zum Einsatz bei Siedeversuchen</i> , Bachelor thesis, filed in April 6th, 2012.
Christoph Jenke	<i>Entwicklung eines optischen Messverfahrens auf Basis der digitalen holographischen Interferometrie zur Untersuchung von Wärmeübergängen beim Sieden</i> , Semesterarbeit, filed in May 5th, 2012.
Julian Kuczaty	<i>Anwendung der digitalen holografischen Interferometrie zur Untersuchung von Wärmeübergängen beim Sieden</i> , Bachelor thesis, filed in September 26th, 2012.
Michael Saier	<i>Untersuchung von Siedevorgängen mit optischen Messverfahren</i> , Bachelor thesis, filed in October 30th, 2012.
Wolfgang Muselmann	<i>Experimentelle Wärmestromuntersuchung beim Übergang des CHF und Betrachtung des Gasverhaltens beim stationären und instationären Blasensieden</i> , Semesterarbeit, filed in January 30th, 2013.

References

- [1] PIVLab developed by Dipl. Biol. William Thielicke and Prof. Dr. Eize J. Stamhuis, Copyright (c) 2009, W. Thielicke, <http://pivlab.blogspot.de/>.
- [2] M. A. Akhavan-Behabadi, R. Kumar, and M. Jamali. Investigation on Heat Transfer and Pressure Drop During Swirl Flow Boiling of R-134a in a Horizontal Tube. *International Journal of Heat and Mass Transfer*, 52:1918–1927, 2009.
- [3] S. Basic, L. Skerget, and J. Marn. Hydrodynamics of Partial Nucleate Boiling by PIV Technique. *International Journal of Dynamics of Fluids*, 3:11–30, 2007.
- [4] A. Bieberle, H.-U. Härtling, S. Rabha, and M. Schubert. Gamma-Ray Computed Tomography for Imaging of Multiphase Flows. *Chemie Ingenieur Technik*, 85:1002–1011, 2013.
- [5] G. Bloch, G. Heideker, S. Götz, and T. Sattelmayer. Anwendung der digitalen Holographie zur Untersuchung von Zweiphasenströmungen und Phasenübergängen. In *Lasermethoden in der Strömungsmesstechnik*, Ilmenau, Germany, 2011.
- [6] G. Bloch, D. Schmitt, and T. Sattelmayer. Influence of Turbulence Induced by Perforated Plates on Heat Transfer and Critical Heat Flux in Subcooled Flow Boiling. In *Proceedings of ITP-2011*, Dresden, Germany, 2011.
- [7] G. Bloch, W. Muselmann, M. Saier, and T. Sattelmayer. A Phenomenological Study on Effects Leading to the Departure From Nucleate Boiling in Subcooled Flow Boiling. *International Journal of Heat and Mass Transfer*, 67:61–69, 2013.
- [8] G. Bloch and T. Sattelmayer. Validation of Mechanistic CHF Models Using Optical Measuring Techniques. *Kerntechnik*, 01:57–59, 2013.

-
- [9] G. Bloch and T. Sattelmayer. Einfluss von Turbulenz und Sekundärströmungen auf das unterkühlte Strömungssieden in reaktortypischen Konfigurationen. Fachlicher Schlussbericht gem. Nr. 3.2 BNBest-BMBF 98 zum BMBF Förderkennzeichen 02NUK010E . Technical report, Technische Universität München, 2013.
- [10] G. Bloch and T. Sattelmayer. Effects of Turbulence and Secondary Flows on Subcooled Flow Boiling. *Heat and Mass Transfer*, 50(3): 427–435, 2014. ISSN 0947-7411.
- [11] G. Bloch, C. Jenke, J. Kuczaty, L. Böck, and T. Sattelmayer. Einsatz von digitaler holografischer Interferometrie zur Erfassung von Temperaturgradienten und Wärmetransport in Siedevorgängen. In *Lasermethoden in der Strömungsmesstechnik*, Rostock, Germany, 2012.
- [12] G. Bloch, C. Jochum, T. Schechtl, and T. Sattelmayer. Subcooled Flow Boiling in a Rectangular Channel With Added Turbulence and Longitudinal Vortices. In *Proceedings of the 2012 20th International Conference on Nuclear Engineering collocated with the ASME 2012 Power Conference*, Anaheim, USA, 2012.
- [13] G. Bloch, J. Loth, M. Bruder, and T. Sattelmayer. Effects of Turbulence and Longitudinal Vortices on Vapor Distribution and Heat Fluxes in Subcooled Flow Boiling. In *Proceedings of ECI 8th Boiling and Condensation*, Lausanne, Switzerland, 2012.
- [14] G. Bloch, J. Elfner, K. Finke, and T. Sattelmayer. Setup and Fabrication of Cost Effective, Robust Fiber Optical Needle Probes for Application in Multiphase Flows. In *Lasermethoden in der Strömungsmesstechnik*, München, Germany, 2013.
- [15] G. Bloch, J. Kuczaty, and T. Sattelmayer. Application of High-Speed Digital Holographic Interferometry for the Analysis of Temperature Distributions and Velocity Fields in Subcooled Flow Boiling. *Experiments in Fluids*, 55(2):1–12, 2014. ISSN 0723-4864.
- [16] G. Bloch, M. Bruder, and T. Sattelmayer. A Study on the Mechanisms Triggering the DNB in Subcooled Vertical Flow Boiling Using a Complementary Experimental Approach. *International Journal of Heat and Mass Transfer*, 92:403–413, 2016.

- [17] G. Bloch, M. Bruder, and T. Sattelmayer. A Critical Review on the Mechanisms Triggering the DNB in Subcooled Flow Boiling Using a Complementary Experimental Approach. In *Proceedings of the 9th International Conference on Boiling and Condensation Heat Transfer*, Boulder, Colorado, April 26-30, 2015.
- [18] D. Bothe, M. Schmidtke, and H.-J. Warnecke. VOF-Simulation of the Lift Force for Single Bubbles in a Simple Shear Flow. *Chem. Eng. Technol.*, 29:1048–1053, 2006.
- [19] C. Boyer, A.-M. Duquenne, and G. Wild. Measuring Techniques in Gas- Liquid and Gas- Liquid- Solid- Reactors. *Chemical Engineering Science*, 57:3185–3215, 2002.
- [20] P. Bricard and A. Souyri. Understanding and modeling DNB in forced convective boiling : a critical review. In *Proceedings of the First International Symposium on Two-Phase Flow Modelling and Experimentation, Rome, Italy, 9-11 October, 1995*, 1995.
- [21] M. Bruder, G. Bloch, and T. Sattelmayer. Critical Heat Flux in Flow Boiling - Review of the Current Understanding and Experimental Approaches. In *Proceedings of the 9th International Conference on Boiling and Condensation Heat Transfer*, Boulder, Colorado, April 26-30, 2015.
- [22] M. Buchholz, T. Lüttich, H. Auracher, and W. Marquardt. Experimental Investigation of Local Processes in Pool Boiling Along the Entire Boiling Curve. *International Journal of Heat and Fluid Flow*, 25:243–261, 2004.
- [23] M. Buchholz, H. Auracher, T. Lüttich, and W. Marquardt. A Study of Local Heat Transfer Mechanisms Along the Entire Boiling Curve by Means of Microsensors. *International Journal of Thermal Sciences*, 45:269–283, 2006.
- [24] V. P. Carey. *Liquid-Vapor Phase-Change Phenomena*. Hemisphere Publishing Corporation, 1992.
- [25] A. Cartellier and J. Achard. Local Phase Detection Probes in Fluid/Fluid Two-Phase Flows. *Review of Scientific Instruments*, 62: 279–303, 1991.

-
- [26] A. Cartellier and E. Barrau. Monofiber Optical Probes for Gas Detection and Gas Velocity Measurements: Conical Probes. *International Journal of Multiphase Flow*, 24:1265–1294, 1998.
- [27] A. Cartellier. Measurement of Gas Phase Characteristics Using new Monofiber Optical Probes and Real-Time Signal Processing. *Nuclear Engineering and Design*, 184:393–408, 1998.
- [28] G. P. Celata, M. Cumo, A. Mariani, M. Simoncini, and G. Zummo. Rationalization of Existing Mechanistic Models for the Prediction of Water Subcooled Flow Boiling Critical Heat Flux. *Int. J. Heat Mass Transfer*, 37:347–360, 1994.
- [29] G. P. Celata, M. Cumo, and F. d’Annibale. Direct Contact Evaporation of Nearly Saturated R 114 in Water. *Int. J. Heat Mass Transfer*, 38:1495–1504, 1995.
- [30] G. P. Celata, M. Cumo, A. Mariani, and G. Zummo. The Prediction of the Critical Heat Flux in Water-Subcooled Flow Boiling. *Int. J. Heat Mass Transfer*, 38:1111–1119, 1995.
- [31] G. P. Celata, M. Cumo, Y. Katto, and A. Mariani. Prediction of the Critical Heat Flux in Water Subcooled Flow Boiling Using a new Mechanistic Approach. *International Journal of Heat and Mass Transfer*, 42:1457–1466, 1999.
- [32] G. P. Celata, M. Cumo, D. Gallo, A. Mariani, and G. Zummo. A Photographic Study of Subcooled Flow Boiling Burnout at High Heat Flux and Velocity. *International Journal of Heat and Mass Transfer*, 50:283–291, 2007.
- [33] G. P. Celata, M. Cumo, and A. Mariani. Geometrical Effects on the Subcooled Flow Boiling Critical Heat Flux. *Revue Générale de Thermique*, 36:807–814, 1997.
- [34] G. P. Celata, M. Cumo, A. Mariani, and G. Zummo. Burnout in Subcooled Flow Boiling of Water. A Visual Experimental Study. *Int. J. Therm. Sci.*, 39:896–908, 2000.
- [35] G. Celata and A. Mariani. CHF and Post-CHF (Post-Dryout) Heat Transfer, Chapter 17. *Handbook of Phase Change: Boiling and Con-*

- densation, edited by Kandlikar, S.G. and Shoji, M. and Dhir, V.K., pages 443–493, 1999.*
- [36] G. Celata, M. Cumo, A. Mariani, and G. Zummo. The Prediction of the Critical Heat Flux in Water-Subcooled Flow Boiling. *Int. J. Heat Mass Transfer*, 38:1111–1119, 1995.
- [37] X. Cheng and U. Müller. Review on Critical Heat Flux in Water Cooled Reactors. Wissenschaftliche Berichte FZKA 6825, Forschungszentrum Karlsruhe, Institut für Kern- und Energietechnik, Forschungszentrum Karlsruhe GmbH, Postfach 3640, 76021 Karlsruhe, 2003.
- [38] D. Chisholm. *Two-Phase Flow in Pipelines and Heat Exchangers*. George Godwin, London and New York, 1983.
- [39] J. G. Collier and J. R. Thome. *Convective Boiling and Condensation*. Oxford University Press, 1994.
- [40] G. Comte-Bellot and S. Corrsin. The Use of a Contraction to Improve the Isotropy of Grid-Generated Turbulence. *Journal of Fluid Mechanics*, 25, part 4:657–682, 1966.
- [41] M. J. da Silva, E. N. dos Santos, U. Hampel, I. H. Rodriguez, and O. M. H. Rodriguez. Phase Fraction Distribution Measurement of Oil-Water Flow Using a Capacitance Wire-Mesh Sensor. *Measurement Science and Technology*, 22:1–9, 2011.
- [42] M. da Silva, E. Schleicher, and U. Hampel. Capacitance Wire- Mesh Sensor for Fast Measurement of Phase Fraction Distributions. *Measurement Science and Technology*, 18:2245–2251, 2007.
- [43] T. P. Davies. Schlieren Photography - Short Bibliography and Review. *Optics and Laser Technology*, 13, Issue 1:37–42, February 1981.
- [44] A. V. Dedov, A. T. Komov, A. N. Varava, and V. V. Yagov. Hydrodynamics and Heat Transfer in Swirl Flow Under Conditions of One-Side Heating. Part 2: Boiling Heat Transfer. Critical Heat Fluxes. *International Journal of Heat and Mass Transfer*, 53:4966–4975, 2010.
- [45] A. V. Dedov, A. T. Komov, A. N. Varava, and V. V. Yagov. Hydrodynamics and Heat Transfer in Swirl Flow Under Conditions of One-Side

- Heating. Part 1: Pressure Drop and Single-Phase Heat Transfer. *International Journal of Heat and Mass Transfer*, 53:4123–4131, 2010.
- [46] F. Demiray and J. Kim. Microscale Heat Transfer Measurements During Pool Boiling of FC-72: Effect of Subcooling. *International Journal of Heat and Mass Transfer*, 47 (2004):3257–3268, 2004.
- [47] J.-M. Desse and R. Deron. Shadow, Schlieren and Color Interferometry. *The Onera Journal AerospaceLab*, Issue1:1–10, 2009.
- [48] J.-M. Desse, P. Picart, and P. Tankam. Digital Three-Color Holographic Interferometry for Flow Analysis. *Optics Express*, 16, Issue 8: 5471–5480, April 2008.
- [49] M. P. Fiori and A. E. Bergles. Model of Critical Heat Flux in Subcooled Flow Boiling. Technical report, Massachusetts Institute of Technology, Department of Mechanical Engineering, Engineering Projects Laboratory, 1968.
- [50] J. Galloway and I. Mudawar. CHF Mechanism in Flow Boiling From a Short Heated Wall - I. Examination of Near-Wall Conditions With the aid of Photomicrography and High-Speed Video Imaging. *Int. J. Heat Mass Transfer*, 36:2511–2526, 1993.
- [51] J. Galloway and I. Mudawar. CHF Mechanism in Flow Boiling From a Short Heated Wall - II. Theoretical CHF Model. *Int. J. Heat Mass Transfer*, 36:2527–2540, 1993.
- [52] J. E. Galloway and I. Mudawar. Critical Heat Flux Enhancement by Means of Liquid Subcooling and Centrifugal Force Induced by Flow Curvature. *Int. J. Heat Mass Transfer*, 35:1247–1260, 1992.
- [53] W. K. George. The Decay of Homogeneous Isotropic Turbulence. *Physics of Fluids A*, 4:1492–1509, 1992.
- [54] C. Gerardi, J. Buongiorno, L. Wen Hu, and T. McKrell. Study of Bubble Growth in Water Pool Boiling Through Synchronized, Infrared Thermometry and High-Speed Video. *International Journal of Heat and Mass Transfer*, 53:4185–4192, 2010.
- [55] C. O. Gersey and I. Mudawar. Effects of Heater Length and Orientation on the Trigger Mechanism for Near-Saturated Flow Boiling

- Critical Heat Flux - II. Critical Heat Flux Model. *Int. J. Heat Mass Transfer*, 38:643–654, 1995.
- [56] I. Golobic. Effects of Heater-Side Factors on the Saturated Pool Boiling Critical Heat Flux. *Experimental Thermal and Fluid Science*, 15: 43–51, 1997.
- [57] D. C. Groeneveld, L. K. H. Leung, P. L. Kirillov, V. P. Bobkov, I. P. Smogalev, V. N. Vinogradov, X. C. Huang, and E. Royer. The 1995 Look-up Table for Critical Heat Flux in Tubes. *Nuclear Engineering and Design*, 23:1–23, 1995.
- [58] D. C. Groeneveld, L. K. H. Leung, A. Z. Vasic, Y. J. Guo, and S. C. Cheng. A Look-up Table for Fully Developed Film-Boiling Heat Transfer. *Nuclear Engineering and Design*, 225:83–97, 2003.
- [59] D. C. Groeneveld, J. Q. Shan, A. Z. Vasic, L. K. H. Leung, A. Durmayaz, J. Yang, S. C. Cheng, and A. Tanase. The 2006 CHF Look-up Table. *Nuclear Engineering and Design*, 237:1909–1992, 2007.
- [60] G. Guglielmini and E. Nannei. On the Effect of Heating Wall Thickness on Pool Boiling Burnout. *International Journal of Heat and Mass Transfer*, 19:1073–1075, 1976.
- [61] F. C. Gunther. Photographic Study of Surface-Boiling Heat Transfer to Water With Forced Convection. *Transaction of the ASME*, 73: 115–123, 1951.
- [62] D. D. Hall and I. Mudawar. Evaluation of Subcooled Critical Heat Flux Correlations Using the PU-BTFL CHF Database for Vertical Upflow of Water in a Uniformly Heated Round Tube. *Nuclear Technology*, 117:234–247, 1997.
- [63] D. D. Hall and I. Mudawar. Critical Heat Flux (CHF) for Water Flow in Tubes - II. Subcooled CHF Correlations. *International Journal of Heat and Mass Transfer*, 43:2605–2640, 2000.
- [64] D. D. Hall and I. Mudawar. Critical Heat Flux (CHF) for Water Flow in Tubes - I. Compilation and Assessment of World CHF Data. *International Journal of Heat and Mass Transfer*, 43:2573–2604, 2000.

-
- [65] Y. Haramura and Y. Katto. A New Hydrodynamic Model of Critical Heat Flux, Applicable Widely to Both Pool and Forced Convection Boiling on Submerged Bodies in Saturated Liquids. *International Journal of Heat and Mass Transfer*, 26:389–399, 1983.
- [66] M. J. Hargather, M. J. Lawson, G. S. Settles, and L. M. Weinstein. Seedless Velocimetry Measurements by Schlieren Image Velocimetry. *AIAA Journal*, 49, No. 3:611–620, March 2011.
- [67] W. Hebel and W. Detavernier. On the Velocity Profile of Vapour Bubbles at Critical Heat Flux. *Nuclear Engineering and Design*, 74: 253–257, 1982.
- [68] W. Hebel, W. Detavernier, and M. Decreton. A Contribution to the Hydrodynamics of Boiling Crisis in a Forced Flow of Water. *Nuclear Engineering and Design*, 64:433–445, 1981.
- [69] G. F. Hewitt. *Measurement of Two Phase Flow Parameters*. Academic Press, 1978.
- [70] R. Hino and T. Ueda. Studies on Heat Transfer and Flow Characteristics in Subcooled Flow Boiling - Part 2. Flow Characteristics. *International Journal of Multiphase Flow*, 11(3):283–297, 1985.
- [71] M. Hong, A. Cartellier, and E. J. Hopfinger. Characterization of Phase Detection Optical Probes for the Measurement of the Dispersed Phase Parameters in Sprays. *International Journal of multiphase flow*, 30: 615–648, 2004.
- [72] V. Ilchenko. *Digitale holographische Geschwindigkeitsmessung mittels Kreuzkorrelation und Partikelverfolgung (DHPIV)*. PhD thesis, Technische Universität München, 2007.
- [73] F. Inasaka and L. H. Nariai. Evaluation of Subcooled Critical Heat Flux Correlations for Tubes With and Without Internal Twisted Tapes . *Nuclear Engineering and Design*, 163:225–239, 1996.
- [74] F. Inasaka and H. Nariai. Enhancement of Subcooled Flow Boiling Critical Heat Flux for Water in Tubes With Internal Twisted Tapes Under One-Sided-Heating Conditions. *Fusion Engineering and Design*, 39-40:347–354, 1998.

- [75] L. M. Jiji. *Incipient boiling and the Bubble Boundary Layer Formation Over a Heated Plate for Forced Convection Flow in a Pressurized Rectangular Channel*. PhD thesis, University of Michigan, 1962.
- [76] D. R. Jonassen, G. S. Settles, and M. D. Tronosky. Schlieren "PIV" for Turbulent Flows. *Optics and Lasers in Engineering*, 44, Issues 3-4: 190–207, March-April 2006.
- [77] E. J. Juliá, W. K. Harteveld, R. F. Mudde, and H. E. Van den Akker. On the Accuracy of the Void Fraction Measurements Using Optical Probes in Bubbly Flows. *Review of Scientific Instruments*, 76:1–13, 2005.
- [78] S. G. Kandlikar. Critical Heat Flux in Subcooled Flow Boiling - An Assessment of Current Understanding and Future Directions for Research. *Multiphase Science and Technology*, 13:207–232, 2001.
- [79] S. Kandlikar. *Handbook of Phase Change: Boiling and Condensation*. Taylor and Francis, New York, 1999.
- [80] N. Kaneyasu, I. Takehiro, K. Torato, and M. Kenichi. Pool Film Boiling Heat Transfer From a Horizontal Cylinder to Saturated Liquids. *Int. J. Heat Mass Transfer*, 15:853–862, 1971.
- [81] Y. Katto. General Features of CHF of Forced Convection Boiling in Uniformly Heated Rectangular Channels. *International Journal of Heat and Mass Transfer*, 24:1413–1419, 1981.
- [82] Y. Katto. A Physical Approach to Critical Heat Flux of Subcooled Flow Boiling in Round Tubes. *Int. J. Heat Mass Transfer*, 33:611–620, 1990.
- [83] Y. Katto. Prediction of Critical Heat Flux of Subcooled Flow Boiling in Round Tubes. *Int. J. Heat Mass Transfer*, 33:1921–1928, 1990.
- [84] Y. Katto. A Prediction Model of Subcooled Water Flow Boiling CHF for Pressure in the Range 0.1-20 MPa. *Int. J. Heat Mass Transfer*, 35:1115–1123, 1992.
- [85] C. R. Kharangate, I. Mudawar, and M. M. Hasan. Experimental and Theoretical Study of Critical Heat Flux in Vertical Upflow with Inlet

- Vapor Void. *International Journal of Heat and Mass Transfer*, 55, Issues 1-3:360–374, 2012.
- [86] C. R. Kharangate, I. Mudawar, and M. M. Hasan. Photographic Study and Modeling of Critical Heat Flux in Horizontal Flow Boiling with Inlet Vapor Void. *International Journal of Heat and Mass Transfer*, 55, Issues 15-16:4154–4168, 2012.
- [87] J. Kim and J. F. Benton. Highly Subcooled Pool Boiling Heat Transfer at Various Gravity Levels. *International Journal of Heat and Fluid Flow*, 23:497–508, 2002.
- [88] C. Konishi, I. Mudawar, and M. M. Hasan. Investigation of Localized Dryout Versus CHF in Saturated Flow Boiling. *International Journal of Heat and Mass Transfer*, 67:131–146, 2013.
- [89] T. Kreis. Digital holographic Interference-Phase Measurement Using the Fourier-Transform Method. *Optical society of America*, 3:847–855, 1986.
- [90] T. M. Kreis, M. Adams, and W. P. Jüptner. Methods of Digital Holography: A Comparison. *Proceedings of SPIE*, 3098:224–233, 1997.
- [91] C. H. Lee and I. Mudawar. A Mechanistic Critical Heat Flux Model for Subcooled Flow Boiling Based on Local Bulk Flow Conditions. *Int. J. Multiphase Flow*, 14:711–728, 1988.
- [92] J. Lee, J. Kim, and K. T. Kiger. Time-and Space-Resolved Heat Transfer Characteristics of Single Droplet Cooling Using Microscale Heater Arrays. *International Journal of Heat and Fluid Flow*, 22: 188–200, 2001.
- [93] M. Lehner, D. Mewes, U. Dingreiter, and R. Tauscher. *Applied Optical Measurements*. Springer, 1999.
- [94] J. C. Lim and J. Weisman. A Phenomenologically Based Prediction of the Critical Heat Flux in Channels Containing an Unheated Wall. *Int. J. Heat Mass Transfer*, 33:203–205, 1990.
- [95] A. Lucic and F. Mayinger. Transport Phenomena in Subcooled Flow Boiling. *Heat and Mass Transfer*, 46:1159–1166, 2010.

- [96] A. Manera, B. Ozar, S. Paranjape, M. Ishii, and H.-M. Prasser. Comparison Between Wire-Mesh Sensors and Conductive Needle-Probes for Measurements of Two-Phase Flow Parameters. *Nuclear Engineering and Design*, 239:1718–1724, 2009.
- [97] A. Martínez-González, J. A. Guerrero-Viramontes, and D. Moreno-Hernández. Temperature and Velocity Measurement Fields of Fluids Using a Schlieren System. *Applied Optics*, 51(16):3519–3525, 2012.
- [98] R. J. Mattson. *A Photographic Study of Subcooled Flow Boiling and the Boiling Crisis in Freon-113*. PhD thesis, The University of Michigan, College for Engineering, Department of Mechanical Engineering, Cavitation and Multiphase Flow Laboratory, 1972.
- [99] R. Maurus. *Bestimmung des Blasenverhaltens beim unterkühlten Strömungssieden mit der digitalen Bildfolgenanalyse*. PhD thesis, Technische Universität München, 2003.
- [100] R. Maurus and T. Sattelmayer. Bubble and Boundary Layer Behavior in Subcooled Flow Boiling. *International Journal of Thermal Science*, 45:257–268, 2006.
- [101] R. Maurus, V. Ilchenko, and T. Sattelmayer. Automated High-Speed Video Analysis of the Bubble Dynamics in Subcooled Flow Boiling. *International Journal of Heat and Fluid Flow*, 25:149–158, 2004.
- [102] F. Mayinger and O. Feldmann. *Optical Measurements - Techniques and Applications*. Springer, 2001.
- [103] P. C. Mena, F. A. Rocha, J. A. Teixeira, P. Sechet, and A. Cartellier. Measurement of gas Phase Characteristics Using A Monofibre Optical Probe in a Three-Phase Flow. *Chemical Engineering Science*, 63:4100–4115, 2008.
- [104] I. Mudawar. Recent Advances in High-Flux, Two-Phase Thermal Management. *Journal of Thermal Science and Engineering Applications*, 5:021012–1–021012–15, 2013.
- [105] I. Mudawwar, T. Incropera, and F. Incropera. Boiling Heat Transfer and Critical Heat Flux in Liquid Film Falling on Vertically-Mounted Heat Sources. *International Journal of Heat and Mass Transfer*, 30: 2083–2095, 1987.

-
- [106] J. G. Myers, K. Y. Vamsee, S. W. Hussey, G. F. Yee, and J. Kim. Time and Space Resolved Wall Temperature and Heat Flux Measurements During Nucleate Boiling with Constant Heat Flux Boundary Conditions. *International Journal of Heat and Mass Transfer*, 48: 2429–2442, 2005.
- [107] S. Nukiyama. The Maximum and Minimum Values of The Heat Q Transmitted From Metal to Boiling Water Under Atmospheric Pressure. *J. Jap. Soc. Mech. Eng.*, 37:367–374 (translated in Int. J. Heat Mass Transfer, vol. 9, pp. 1419–1433, 1966), 1934.
- [108] S. B. Pope. *Turbulent Flows*. Cambridge University Press, 2000.
- [109] A. K. Prasad. Particle Image Velocimetry. *Current Science*, VOL. 79, NO. 1, 10 JULY 2000, 79:51–60, 2000.
- [110] H.-M. Prasser, A. Böttger, and J. Zschau. A new Electrode-Mesh Tomograph for gas-liquid flows. *Flow Measurement and Instrumentation*, 9:111–119, 1998.
- [111] H.-M. Prasser, D. Scholz, and C. Zippe. Bubble Size Measurement Using Wire-Mesh Sensors. *Flow Measurement and Instrumentation*, 12:299–312, 2001.
- [112] M. Raffel, C. Willert, and J. Kompenhans. *Particle Image Velocimetry - A practical guide*. Springer, 1998.
- [113] P. Roach. The Generation of Nearly Isotropic Turbulence by Means of Grids. *Heat and Fluid Flow*, 8:82–92, 1987.
- [114] I. Roghair, Y. Lau, N. Deen, H. Slagter, M. Baltussen, M. van Sint Annaland, and J. Kuipers. On the Drag Force of Bubbles in Bubble Swarms at Intermediate and High Reynolds Numbers. *Chemical Engineering Science*, 66(14):3204–3211, 2011.
- [115] T. Rule and J. Kim. Heat Transfer Behavior on Small Horizontal Heaters During Pool Boiling of FC-72. *Journal of Heat Transfer*, Vol. 121/387:1–8, 1999.
- [116] E. Schleicher, M. Jose da Silva, and U. Hampel. Enhanced Local Void and Temperature Measurements for Highly Transient Multiphase

- Flows. *IEEE Transactions on Instrumentation and Measurement*, 57: 401–405, 2008.
- [117] U. Schnars and W. Jüptner. *Digital Holography*. Springer, 2005.
- [118] U. Schnars. Direct Phase Determination in Hologram Interferometry With Use of Digitally Recorded Holograms. *Journal of the Optical Society of America A (JOSA A): Optics, Image Science, and Vision*, 11:2011–2015, 1994.
- [119] S. Sharaf, M. Da Silva, U. Hampel, C. Zippe, M. Beyer, and B. Azopardi. Comparison between Wire Mesh Sensor and Gamma Densitometry Void Measurement in Two-Phase Flows. *Measurement Science and Technology*, 22:1–13, 2011.
- [120] C. Sodtke, J. Kern, N. Schweizer, and P. Stephan. High Resolution Measurements of Wall Temperature Distribution Underneath a Single Vapour Bubble Under Low Gravity Conditions. *International Journal of Heat and Mass Transfer*, 49, Issues 5-6:1100–1106, March 2006.
- [121] J. C. Sturgis and I. Mudawar. Critical Heat Flux in a Long, Rectangular Channel Subjected to One-Sided Heating - II. Analysis of Critical Heat Flux Data. *International Journal of Heat and Mass Transfer*, 42:1849–1862, 1999.
- [122] J. C. Sturgis and I. Mudawar. Critical Heat Flux in a Long, Rectangular Channel Subjected to One-Sided Heating - I. Flow Visualization. *International Journal of Heat and Mass Transfer*, 42:1835–1847, 1999.
- [123] M. A. Styrikovich, E. I. Nevstrueva, and G. M. Dvorina. The Effect of Two-Phase Flow Pattern on the Nature of Heat Transfer Crisis in Boiling. In *Heat Transfer 1970, Papers Presented at the Fourth International Heat Transfer Conference, Paris - Versailles 1970, Volume VI*, 1970.
- [124] R. Tauscher and F. Mayinger. Visualization of Flow Temperature Fields by Holographic Interferometry - Optimization of Compact Heat Exchangers. In *Proceedings of PSFVIP-2*, 1999.
- [125] A. Tomiyama, H. Tamai, I. Zun, and S. Hosokawa. Transverse Migration of Single Bubbles in Simple Shear Flows. *Chemical Engineering Science*, 57:1849–1858, 2002.

-
- [126] L. S. Tong. Boundary-Layer Analysis of the Flow Boiling Crisis. *Int. J. Heat Mass Transfer*, 11:1208–1211, 1968.
- [127] L. Tong and Y. Tang. *Boiling Heat Transfer and Two-Phase Flow*. Taylor and Francis, 1997.
- [128] J. Vejrazka, M. Vecer, S. Orvalho, P. Sechet, M. C. Ruzicka, and A. Cartellier. Measurement Accuracy of a Mono-Fiber Optical Probe in a Bubbly Flow. *International Journal of Multiphase Flow*, 36:533–548, 2010.
- [129] F. M. Verplaetsen and J. A. Berghmans. Film Boiling of an Electrically Insulating Fluid in the Presence of an Electric Field. *Heat and Mass Transfer*, 35:235–241, 1999.
- [130] N. Verrier and M. Atlan. Off-axis Digital Hologram Reconstruction: Some Practical Considerations. *Applied Optics*, 50(34):136–146, 2011.
- [131] R. Visenti, C. Colin, and P. Ruyer. Experimental investigation of heat transfer in transient boiling. *Experimental Thermal and Fluid Science*, 55:95–105, 2014.
- [132] J. Weisman. Letter to the Editor on "Evaluation of Subcooled Critical Heat Flux Correlations for Tubes With and Without Internal Twisted Tapes" by F. Inasaka and H. Nariai and "Consideration of CHF Margin Prediction by Subcooled or Low Quality CHF Correlations" by P. Hejzlar and N.E. Todreas. *Nuclear Engineering and Design*, 163:259–261, 1996.
- [133] J. Weisman and B. S. Pei. Prediction of Critical Heat Flux in Flow Boiling at low Qualities. *Int. J. Heat Mass Transfer*, 26:1463–1477, 1983.
- [134] J. Weisman, J. Y. Yang, and S. Usman. A Phenomenological Model for Boiling Heat Transfer and the Critical Heat Flux in Tubes Containing Twisted Tapes. *Int. J. Heat Mass Transfer*, 37:69–80, 1994.
- [135] F. M. White. *Fluid Mechanics*. McGraw-Hill, 1998.
- [136] J. Y. Yang and J. Weisman. A Phenomenological Model of Subcooled Flow Boiling in the Detached Bubble Region. *International Journal of Multiphase Flow*, 17:77–94, 1991.

- [137] S. H. Ying and J. Weisman. Prediction of Critical Heat Flux in Flow Boiling at Intermediate Qualities. *Int. J. Heat Mass Transfer*, 29: 1639–1648, 1986.
- [138] H. Zhang, I. Mudawar, and M. M. Hasan. Experimental Assessment of the Effects of Body Force, Surface Tension Force, and Inertia on Flow Boiling CHF. *International Journal of Heat and Mass Transfer*, 45:4079–4095, 2002.
- [139] H. Zhang, I. Mudawar, and M. M. Hasan. Investigation of Interfacial Behavior During the Flow Boiling CHF Transient. *International Journal of Heat and Mass Transfer*, 47:1275–1288, 2004.
- [140] H. Zhang, I. Mudawar, and M. M. Hasan. A Method for Assessing the Importance of Body Force on Flow Boiling CHF. *Journal of Heat Transfer*, 126:161–168, 2004.
- [141] H. Zhang, I. Mudawar, and M. M. Hassan. Flow Boiling CHF in Microgravity. *International Journal of Heat and Mass Transfer*, 48: 3107–3118, 2005.
- [142] H. Zhang, I. Mudawar, and M. M. Hasan. Photographic Study of High-Flux Subcooled Flow Boiling and Critical Heat Flux. *International Communications in Heat and Mass Transfer*, 34:653–660, 2007.